

**THÈSE DE DOCTORAT  
DE SORBONNE UNIVERSITÉ**

**Spécialité : Physique**

**École doctorale n°564: Physique en Île-de-France**

réalisée

**au Laboratoire Kastler Brossel**

**sous la direction de Pierre-François Cohadon**

présentée par

**Pierre-Edouard Jacquet**

pour obtenir le grade de :

**DOCTEUR DE SORBONNE UNIVERSITÉ**

**Sujet de la thèse :**

**Progress towards cryogenic squeezed light optomechanics**

**soutenue le ????? 2025**

devant le jury composé de :

M.	Mr.	Rapporteur
M.	Mr.	Rapporteur
M.	Mr.	Examinateur
Mme.	coucou	Examinateuse
Mme.	salut	Présidente du Jury
M.	aurevoir	Directeur de thèse









# **Remerciements**

Merci bien



# Contents

<b>I Theory: Background</b>	<b>3</b>
I.1 Optics . . . . .	5
I.1.1 Spatial Modes . . . . .	5
I.1.2 Quantum Description . . . . .	6
I.1.3 Coherent and Squeezed States . . . . .	9
I.1.4 Sidebands and Quantum Noises . . . . .	13
I.1.5 Quantum Sideband Diagram . . . . .	18
I.2 Cavities . . . . .	19
I.2.1 Cavity Geometries and Stability Conditions . . . . .	19
I.2.2 Cavity Resonances . . . . .	20
I.2.3 Mode-Matching . . . . .	21
I.2.4 Simple Cavities . . . . .	22
I.2.5 Non Linear Cavities . . . . .	28
I.2.6 Optomechanical Cavities . . . . .	35
<b>II Theory: Frequency Dependent Squeezing &amp; Membrane based Optomechanics</b>	<b>43</b>
II.1 Squeezed Light and Optomechanics . . . . .	45
II.1.1 Standard Quantum Limit . . . . .	45

II.1.2 Frequency Independent Squeezing in Optomechanical Cavities . . . . .	48
II.1.3 Frequency Dependent Squeezing in Optomechanical Cavities . . . . .	50
II.1.4 Filter Cavities for Frequency Dependent Squeezing . . . . .	51
II.2 Cavity Optomechanics with Membrane based systems . . . . .	52
II.2.1 Classical Description . . . . .	52
II.2.2 Quantum Langevin Equations . . . . .	53
II.2.3 Mechanical Resonators . . . . .	58
II.2.4 Noise spectra . . . . .	58
<b>III Experimental Methods</b>	<b>61</b>
III.1 Optical Locking Techniques with PyRPL . . . . .	62
III.1.1 Proportion-Integral (PI) Controllers . . . . .	62
III.1.2 Temperature Locks . . . . .	64
III.1.3 Optical paths Locks - Dither Locks . . . . .	64
III.1.4 Side of Fringe Locks . . . . .	65
III.1.5 Pound-Drever-Hall Locks . . . . .	65
III.1.6 Offset frequency Locks . . . . .	66
III.1.7 Coherent Sideband Locks . . . . .	66
III.1.8 PyRPL Control Implementation . . . . .	66
III.2 Optical Cavities and Squeezed Light Generation . . . . .	66
III.2.1 Cavity Types and Alignment Procedures . . . . .	67
III.2.2 Bowtie-type Optical Parametric Oscillator (OPO) . . . . .	67
III.2.3 Phase Matching and Nonlinear Crystals . . . . .	67
III.2.4 Filter Cavities for Squeezing Rotation . . . . .	67
III.3 Quadrature Measurement Techniques . . . . .	67
III.3.1 Direct Detection with Photodiodes . . . . .	67

III.3.2 Balanced Homodyne Detection . . . . .	67
III.3.3 Local Oscillator Design and Control . . . . .	67
<b>IV Experiments: Optomechanics</b>	<b>69</b>
IV.1 System Description and Setup . . . . .	70
IV.1.1 Previous LKB work and Motivation . . . . .	70
IV.1.2 Specifications and Design . . . . .	71
IV.1.3 Flexure Actuation . . . . .	74
IV.1.4 Experimental Setup . . . . .	76
IV.1.5 Alignment Procedures . . . . .	78
IV.2 Experimental Characterization . . . . .	79
IV.2.1 Cavity Characterization . . . . .	79
IV.2.2 Locking Techniques and Stability . . . . .	84
IV.2.3 Optical Ringdowns and Loss Measurements . . . . .	84
IV.2.4 Mechanical Resonator Characterization . . . . .	84
IV.2.5 Bistability . . . . .	84
IV.3 Design of an Optomechanical Fibered Cavity . . . . .	84
IV.3.1 Design considerations . . . . .	84
<b>V Experiments: Squeezed Light</b>	<b>85</b>
V.1 Optical Setup Overview . . . . .	86
V.2 Cavity Resonances and Locks . . . . .	86
V.2.1 IRMC Cavity . . . . .	86
V.2.2 SHG Cavity . . . . .	88
V.2.3 OPO Cavity . . . . .	91
V.3 Spectral analysis . . . . .	91
V.3.1 Detection of Squeezing and Anti-squeezing . . . . .	91

V.3.2 Spectral Variation with Frequency . . . . .	91
V.3.3 Optimal Quadrature Conditions . . . . .	91
V.4 Filter Cavity Concept . . . . .	91
V.4.1 Virgo Filter Cavity . . . . .	91
V.4.2 Thermal effects in bichromatic locks . . . . .	91
Appendix: PDH Derivation . . . . .	95
Appendix: Spectra Derivation . . . . .	99





# Chapter I

## Theory: Background

This chapter will cover the elementary concepts required to describe an membrane based optomechanical system in a quantum regime. We will first recall basics on optical field quantization as well describing coherent and squeezed light field, to then turn to the more specific frequency dependent squeezed light field. Secondly, we will cover the mathematical description of a mechanical resonator interacting with a generic coherent optical field, highlighting the differences with the seminal optomechanical system of a mirror on a spring. Finally, we will derive the equations of motions of a membrane based optomechanical system with frequency dependent squeezed optical fields.

**Contents**

---

<b>I.1</b>	<b>Optics</b>	<b>5</b>
I.1.1	Spatial Modes	5
I.1.2	Quantum Description	6
I.1.3	Coherent and Squeezed States	9
I.1.4	Sidebands and Quantum Noises	13
I.1.5	Quantum Sideband Diagram	18
<b>I.2</b>	<b>Cavities</b>	<b>19</b>
I.2.1	Cavity Geometries and Stability Conditions	19
I.2.2	Cavity Resonances	20
I.2.3	Mode-Matching	21
I.2.4	Simple Cavities	22
I.2.5	Non Linear Cavities	28
I.2.6	Optomechanical Cavities	35

---

## I.1 Optics

### I.1.1 Spatial Modes

The spatial structure of an electromagnetic wave propagating along the  $z$ -axis can be described by a set of well-defined transverse modes, which are solutions of the paraxial Helmholtz equation. The most fundamental solution is the Gaussian mode, whose electric field amplitude reads

$$E(\mathbf{r}) = E_0 \frac{w_0}{w(z)} \exp\left(-\frac{x^2 + y^2}{w^2(z)}\right) \exp\left[-i\left(kz + \frac{k(x^2 + y^2)}{2R(z)} - \psi(z)\right)\right], \quad (\text{I.1})$$

where  $\mathbf{r} = (x, y, z)$ ,  $E_0$  is the field amplitude at the beam waist,  $k = 2\pi/\lambda$  the wavenumber, and  $\lambda$  the optical wavelength. The various quantities introduced above are defined as

$$\begin{aligned} w(z) &\equiv w_0 \sqrt{1 + (z/z_R)^2}, & z_R &\equiv \pi w_0^2 / \lambda, \\ R(z) &\equiv z \left[1 + (z_R/z)^2\right], & \psi(z) &\equiv \arctan(z/z_R), \end{aligned}$$

with  $w_0$  the waist,  $z_R$  the Rayleigh range,  $R(z)$  the wavefront curvature, and  $\psi(z)$  the Gouy phase. A compact expression of the Gaussian envelope is written as

$$E(\mathbf{r}) = E_0 \frac{iz_R}{q(z)} \exp\left(-\frac{ik(x^2 + y^2)}{2q(z)}\right) e^{ikz} \quad \text{with} \quad q(z) \equiv z + iz_R, \quad (\text{I.2})$$

where we defined the complex beam parameter  $q(z)$ . Beyond the fundamental Gaussian mode, more general solutions of the paraxial equation can be constructed. In Cartesian coordinates, these are the Hermite–Gaussian modes  $\text{TEM}_{mn}$ , given by

$$\begin{aligned} E_{mn}(\mathbf{r}) &= E_0 \frac{w_0}{w(z)} H_m\left(\frac{\sqrt{2}x}{w(z)}\right) H_n\left(\frac{\sqrt{2}y}{w(z)}\right) \exp\left(-\frac{x^2 + y^2}{w^2(z)}\right) \\ &\quad \times \exp\left[-i\left(kz + \frac{k(x^2 + y^2)}{2R(z)} - (m + n + 1)\psi(z)\right)\right], \quad (\text{I.3}) \end{aligned}$$

where  $H_m, H_n$  are Hermite polynomials.

### I.1.2 Quantum Description

#### Quantised Electromagnetic Field

We consider the quantised electromagnetic field in a volume  $V$ . The electric field operator can be written as

$$\hat{\mathbf{E}}(\mathbf{r}, t) = i \sum_{\ell} \mathcal{E}_{\ell} \left[ \hat{a}_{\ell} \mathbf{f}_{\ell}(\mathbf{r}) e^{-i\omega_{\ell}t} - \hat{a}_{\ell}^{\dagger} \mathbf{f}_{\ell}^*(\mathbf{r}) e^{+i\omega_{\ell}t} \right], \quad (\text{I.4})$$

where  $\mathcal{E}_{\ell} = \sqrt{\frac{\hbar\omega_{\ell}}{2\varepsilon_0 V}}$  is the field amplitude per photon in mode  $\ell$ ,  $\hbar$  is the reduced Planck constant,  $\omega_{\ell}$  is the angular frequency of mode  $\ell$ , and  $\varepsilon_0$  is the vacuum permittivity. The spatial mode functions  $\mathbf{f}_{\ell}(\mathbf{r})$  form an orthonormal basis in  $V$  according to

$$\int_V d^3r \mathbf{f}_{\ell}^*(\mathbf{r}) \cdot \mathbf{f}_{\ell'}(\mathbf{r}) = \delta_{\ell\ell'}, \quad \mathbf{f}_{\ell}(\mathbf{r}) \propto E_{mn}(\mathbf{r})$$

The index  $\ell$  then labels the different modes, which can include spatial, polarization, and frequency degrees of freedom.

The annihilation and creation operators  $\hat{a}_{\ell}$  and  $\hat{a}_{\ell}^{\dagger}$  satisfy the canonical commutation relations

$$[\hat{a}_{\ell}, \hat{a}_{\ell'}^{\dagger}] = \delta_{\ell\ell'}, \quad [\hat{a}_{\ell}, \hat{a}_{\ell'}] = 0, \quad [\hat{a}_{\ell}^{\dagger}, \hat{a}_{\ell'}^{\dagger}] = 0.$$

#### Fock basis

In this description of the optical field, each mode  $\ell$  is modeled as a quantum harmonic oscillator with a discrete set of energy eigenstates known as *Fock states* or number states, denoted  $|n_{\ell}\rangle$ . These states form an orthonormal basis and satisfy  $\hat{n}_{\ell}|n_{\ell}\rangle = n_{\ell}|n_{\ell}\rangle$ , where  $\hat{n}_{\ell}$  is the number operator defined by

$$\hat{n}_{\ell} = \hat{a}_{\ell}^{\dagger} \hat{a}_{\ell}.$$

The action of the creation and annihilation operators on these states is given by

$$\hat{a}_{\ell}|n_{\ell}\rangle = \sqrt{n_{\ell}}|n_{\ell}-1\rangle, \quad \hat{a}_{\ell}^{\dagger}|n_{\ell}\rangle = \sqrt{n_{\ell}+1}|n_{\ell}+1\rangle.$$

They allow transitions between Fock states by lowering or raising the photon number in mode  $\ell$  by one unit. The vacuum state  $|0_{\ell}\rangle$  is annihilated by  $\hat{a}_{\ell}$ , satisfying  $\hat{a}_{\ell}|0_{\ell}\rangle = 0$ . Thus, the Hamiltonian for the electromagnetic field becomes a sum of harmonic oscillator energies:

$$\hat{H} = \sum_{\ell} \hbar\omega_{\ell} \hat{a}_{\ell}^{\dagger} \hat{a}_{\ell} \quad (\text{I.5})$$

where we ignore the constant zero-point energy term  $\frac{1}{2}\hbar\omega_\ell$  for simplicity.

In the following parts, we will always focus on a single mode of the electromagnetic field unless stated otherwise (for the mode matching part), which is sufficient to illustrate the concepts of quantum optics and optomechanics. The generalization to multiple modes is straightforward and follows the same principles. The electric field operator is then written

$$\hat{\mathbf{E}}(\mathbf{r}, t) = i\mathcal{E}_0 \left[ \hat{a} \mathbf{f}(\mathbf{r}) e^{-i\omega_0 t} - \hat{a}^\dagger \mathbf{f}^*(\mathbf{r}) e^{+i\omega_0 t} \right]. \quad (\text{I.6})$$

### Quadrature Operators

We describe the phase-space properties of a field mode using hermitian quadrature operators. These are linear combinations of the annihilation and creation operators that correspond to measurable observables in the electromagnetic field. The two most common quadratures are defined as follows:

$$\hat{\mathbf{u}} \equiv \begin{pmatrix} \hat{a}_1 \\ \hat{a}_2 \end{pmatrix} = \boldsymbol{\Gamma} \hat{\mathbf{a}} \quad \text{with} \quad \boldsymbol{\Gamma} \equiv \begin{pmatrix} 1 & 1 \\ -i & i \end{pmatrix} \quad \text{and} \quad \hat{\mathbf{a}} \equiv \begin{pmatrix} \hat{a} \\ \hat{a}^\dagger \end{pmatrix} \quad (\text{I.7})$$

where we defined the field vector  $\hat{\mathbf{a}}$  and the transfer matrix  $\boldsymbol{\Gamma}$ , later used to switch from *one-photon* to *two-photon* description of optical elements. In components, we then have  $\hat{a}_1 = \hat{a}^\dagger + \hat{a}$  and  $\hat{a}_2 = i(\hat{a}^\dagger - \hat{a})$ . The matrix form commutator reads

$$[\hat{\mathbf{a}}, \hat{\mathbf{a}}^\dagger] = \sigma_z, \quad (\text{I.8})$$

with  $\sigma_z$  the Pauli Z matrix. An arbitrary rotated quadrature pair is obtained by

$$\hat{\mathbf{u}}_\phi \equiv \begin{pmatrix} \hat{a}_\phi \\ \hat{a}_{\phi+\pi/2} \end{pmatrix} = \mathbf{R}(\phi) \hat{\mathbf{u}} = \mathbf{R}(\phi) \boldsymbol{\Gamma} \hat{\mathbf{a}} \quad \text{with} \quad \mathbf{R}(\phi) \equiv \begin{pmatrix} \cos \phi & \sin \phi \\ -\sin \phi & \cos \phi \end{pmatrix}. \quad (\text{I.9})$$

The commutators of the rotated quadrature operators read

$$[\hat{\mathbf{u}}_\phi, \hat{\mathbf{u}}_\phi^\dagger] = \mathbf{R}(\phi) \boldsymbol{\Gamma} [\hat{\mathbf{a}}, \hat{\mathbf{a}}^\dagger] \boldsymbol{\Gamma}^\dagger \mathbf{R}^\dagger(\phi) = 2i \mathbf{J} \quad \text{with} \quad \mathbf{J} \equiv \begin{pmatrix} 0 & 1 \\ -1 & 0 \end{pmatrix}. \quad (\text{I.10})$$

Note that since  $\hat{\mathbf{u}}_\phi$  is hermitian, we have  $\hat{\mathbf{u}}_\phi^\dagger = \hat{\mathbf{u}}_\phi^T$ , and similarly  $\mathbf{R}^\dagger(\phi) = \mathbf{R}^T(\phi)$  since all its entries are real.

This compact vector form will be used later for the one- and two-photon description of the light field behaviours in optomechanical systems with squeezed light input.

**Note:** notes the fact that these are defined for a specific  $\ell$ , so at each mode is associated such

a quadrature vector. The multimode treatment is used by the multimode quantum optics community, notably to describe multimode non gaussian states, hidden squeezing (beyond homodyne detection correlations, Patera and co)

### Linearization of the optical field

The annihilation operator can be decomposed as

$$\hat{a} = \bar{\alpha} + \delta\hat{a} \quad (\text{I.11})$$

where  $\bar{\alpha} = \langle \hat{a} \rangle \in \mathbb{C}$  is the mean complex amplitude of the quantum state, and  $\delta\hat{a}$  represents quantum fluctuations with  $\langle \delta\hat{a} \rangle = 0$ . Note this decomposition is valid for any quantum state, including coherent and squeezed states. We note  $\bar{\alpha}$  to distinguish it from the complex amplitude  $\alpha$  of a coherent state introduced below, which is a specific case of this decomposition. The associated matrix form is

$$\hat{\mathbf{a}} = \begin{pmatrix} \bar{\alpha} \\ \bar{\alpha}^* \end{pmatrix} + \begin{pmatrix} \delta\hat{a} \\ \delta\hat{a}^\dagger \end{pmatrix} = \bar{\mathbf{a}} + \delta\hat{\mathbf{a}} \quad (\text{I.12})$$

and it then follows that the quadrature operators can also be expressed as

$$\hat{\mathbf{u}}_\phi = \mathbf{R}(\phi) \mathbf{\Gamma} (\bar{\mathbf{a}} + \delta\hat{\mathbf{a}}) = \bar{\mathbf{u}}_\phi + \delta\hat{\mathbf{u}}_\phi \quad (\text{I.13})$$

where the fluctuations retain the canonical commutation relations

$$[\delta\hat{\mathbf{a}}, \delta\hat{\mathbf{a}}^\dagger] = \sigma_{\mathbf{z}} \quad \Rightarrow \quad [\delta\hat{\mathbf{u}}_\phi^T, \delta\hat{\mathbf{u}}_\phi^T] = 2i \mathbf{J}. \quad (\text{I.14})$$

**Note:** notes on first and second moments, as well as beyond second moments correlations and their use i.e. when and why is this linearization ok to use etc etc

### Heisenberg Uncertainty Relation

The covariance of Hermitian operators  $\hat{A}$  and  $\hat{B}$  is defined as

$$\text{Cov}(\hat{A}, \hat{B}) = \frac{1}{2} \langle \{\delta\hat{A}, \delta\hat{B}\} \rangle \quad (\text{I.15})$$

such that it reduces to the variance  $\delta A^2$  if  $\hat{A} = \hat{B}$ . Considering the quadrature operators, we define the covariance matrix as

$$\mathbf{V}_\phi \equiv \frac{1}{2} \langle \{\delta\hat{\mathbf{u}}_\phi, \delta\hat{\mathbf{u}}_\phi^T\} \rangle = \begin{pmatrix} \langle \delta\hat{a}_\phi^2 \rangle & \text{Cov}(\hat{a}_\phi, \hat{a}_{\phi+\pi/2}) \\ \text{Cov}(\hat{a}_\phi, \hat{a}_{\phi+\pi/2}) & \langle \delta\hat{a}_{\phi+\pi/2}^2 \rangle \end{pmatrix} \quad (\text{I.16})$$

and the Heisenberg uncertainty relation reads as

$$\det \mathbf{V}_\phi \geq 1 \quad \Rightarrow \quad \langle \delta \hat{a}_\phi^2 \rangle \langle \delta \hat{a}_{\phi+\pi/2}^2 \rangle - \text{Cov}^2(\hat{a}_\phi, \hat{a}_{\phi+\pi/2}) \geq 1 \quad (\text{I.17})$$

### Graphical Representation of Gaussian States

For Gaussian states, we can actually picture them in a 2D space, where ...

#### I.1.3 Coherent and Squeezed States

We now turn to standard optical quantum states, in particular gaussian states i.e. full positive in Wigner function representations such as coherent and squeezed states, that we will denote in braket notation as  $|\alpha\rangle$  and  $|\alpha, r, \theta\rangle$ .

##### Coherent States:

The coherent state  $|\alpha\rangle$  is an eigenstate of the annihilation operator:

$$\hat{a} |\alpha\rangle = \alpha |\alpha\rangle \quad (\text{I.18})$$

where  $\alpha = |\alpha|e^{i\bar{\varphi}}$  is a complex number representing the mean coherent amplitude. In this notation, the angle  $\bar{\varphi}$  is the mean angle of the distribution, used to describe the relative phase to a reference (e.g. a local oscillator), as in Fig ???. The  $\hat{a}$  linear decomposition above (Eq (I.11)) then yields  $\alpha = \bar{\alpha}$  for a coherent state. It can be expressed in the Fock basis as

$$|\alpha\rangle = e^{-|\alpha|^2/2} \sum_{n=0}^{\infty} \frac{\alpha^n}{\sqrt{n!}} |n\rangle \quad (\text{I.19})$$

and are generated by the action of the displacement operator  $\hat{D}(\alpha)$  on the vacuum state  $|0\rangle$ :

$$|\alpha\rangle = \hat{D}(\alpha) |0\rangle, \quad \hat{D}(\alpha) = \exp(\alpha \hat{a}^\dagger - \alpha^* \hat{a}) \quad (\text{I.20})$$

**Note:** note on the convention used i.e.  $\alpha \neq \bar{\alpha}$ ,  $\alpha_0 \neq \bar{\alpha}_0$

**Expectation values:** Using the quadrature vector  $\hat{\mathbf{u}}_\phi$  (Eq I.9), the expectation values in a coherent state are

$$\langle \hat{\mathbf{u}}_\phi \rangle = \mathbf{R}(\phi) \langle \hat{\mathbf{u}} \rangle = 2 \begin{pmatrix} \text{Re}(\alpha e^{-i\phi}) \\ \text{Im}(\alpha e^{-i\phi}) \end{pmatrix} \quad (\text{I.21})$$

such that the components reduce to  $2\text{Re}(\alpha)$  and  $2\text{Im}(\alpha)$  if  $\phi = 0$ .

**Amplitude and phase quadratures :** It is convenient to introduce the amplitude-phase quadrature vector at  $\phi = \bar{\varphi}$

$$\hat{\mathbf{u}}_{\bar{\varphi}} = \begin{pmatrix} \hat{p} \\ \hat{q} \end{pmatrix} = \begin{pmatrix} \hat{a}_{\bar{\varphi}} \\ \hat{a}_{\bar{\varphi}+\pi/2} \end{pmatrix}. \quad (\text{I.22})$$

with expectation values

$$\langle \hat{\mathbf{u}}_{\bar{\varphi}} \rangle = 2 \begin{pmatrix} |\alpha| \\ 0 \end{pmatrix}, \quad (\text{I.23})$$

**Covariance matrix:** For a coherent state, fluctuations are vacuum-like:

$$\langle \delta \hat{a}_\phi^2 \rangle = \langle \delta \hat{a}_{\phi+\pi/2}^2 \rangle = 1, \quad \text{Cov}(\hat{a}_\phi, \hat{a}_{\phi+\pi/2}) = 0, \quad (\text{I.24})$$

so that

$$\mathbf{V}_\phi = \begin{pmatrix} 1 & 0 \\ 0 & 1 \end{pmatrix} = \mathbf{1}, \quad \forall \phi. \quad (\text{I.25})$$

This saturates the Heisenberg uncertainty relation  $\det \mathbf{V}_\phi = 1$  in the units defined here i.e. it is a minimum uncertainty state.

**Photon number statistics:** The mean and variance of the photon number operator  $\hat{N} = \hat{a}^\dagger \hat{a}$  are

$$\langle \hat{N} \rangle = |\alpha|^2, \quad \Delta N^2 = |\alpha|^2. \quad (\text{I.26})$$

That is, coherent states display Poissonian photon statistics.

### Squeezed States:

Squeezed states  $|\alpha, r, \theta\rangle$  are quantum gaussian states of light in which the noise (variance) of one quadrature is reduced below the vacuum level, at the expense of increased noise in the conjugate quadrature. The single-mode squeezed vacuum state is defined as

$$|0, r, \theta\rangle = \hat{S}(r, \theta)|0\rangle, \quad \hat{S}(\theta) = \exp \left[ \frac{r}{2} (e^{-2i\theta} \hat{a}^2 - e^{-2i\theta} \hat{a}^{\dagger 2}) \right] \quad (\text{I.27})$$

where  $r$  is the squeezing parameter (strength) and  $\theta$  is the squeezing angle i.e. the angle along which one quadrature is reduced below vacuum level. The most general Gaussian state is the displaced squeezed state, obtained by applying both the squeezing operator  $\hat{S}(r, \theta)$  and the displacement operator  $\hat{D}(\alpha)$  to the vacuum:

$$|\alpha, r, \theta\rangle = \hat{S}(r, \theta)\hat{D}(\alpha)|0\rangle \quad (\text{I.28})$$

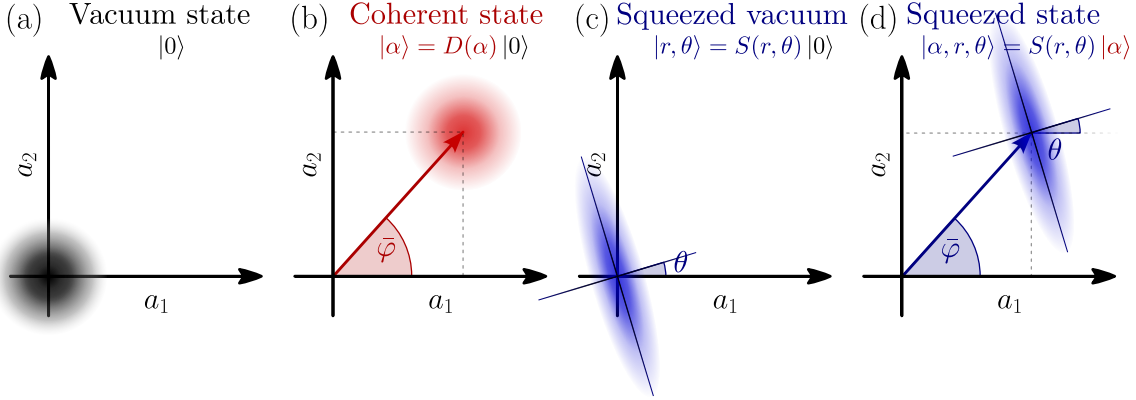


Fig. I.1 Phase-space representations of quantum states and transformations. (a) Wigner function of the vacuum state: a circular Gaussian centered at the origin, representing equal quantum fluctuations in both quadratures  $a_1$  and  $a_2$ . (b) Wigner function of a coherent state: a displaced circular Gaussian, showing a shift in phase space along an angle  $\varphi$  with unchanged, isotropic noise. (c) Wigner function of a squeezed vacuum state: an elliptical Gaussian centered at the origin, with reduced noise along a rotated quadrature  $X_\theta$  and increased noise in the orthogonal direction. (d) Wigner function of a displaced squeezed state: an ellipse shifted away from the origin, combining anisotropic fluctuations and a nonzero mean amplitude. The displacement angle  $\varphi$  and squeezing angle  $\theta$  are independent.

where  $\hat{D}(\alpha)$  displaces the state in phase space by the complex amplitude  $\alpha$ , defined similarly to the coherent state.

**Note:** The displacement and squeezing operators do not commute, i.e.  $\hat{D}(\alpha)\hat{S}(r,\theta) \neq \hat{S}(r,\theta)\hat{D}(\alpha)$ . However, both orderings correspond to experimentally valid procedures: one can either squeeze the vacuum and then displace (e.g. by mixing with a coherent state on a beamsplitter), or squeeze a coherent state straight away (e.g. by seeding an optical parametric amplifier). The resulting state is always a displaced squeezed state, but the relative phase between displacement and squeezing may differ.

**Expectation values:** Using the usual quadratures defined in Eq (I.7) and (I.9), the expectation values in a displaced squeezed state are

$$\langle \hat{\mathbf{u}} \rangle = 2 \begin{pmatrix} \operatorname{Re} \alpha \\ \operatorname{Im} \alpha \end{pmatrix}, \quad \langle \hat{\mathbf{u}}_\phi \rangle = 2 \begin{pmatrix} \operatorname{Re} (\alpha e^{-i\phi}) \\ \operatorname{Im} (\alpha e^{-i\phi}) \end{pmatrix}. \quad (\text{I.29})$$

For a squeezed vacuum ( $\alpha = 0$ ) all quadrature means vanish. Choosing  $\phi = \theta$ , the fluctua-

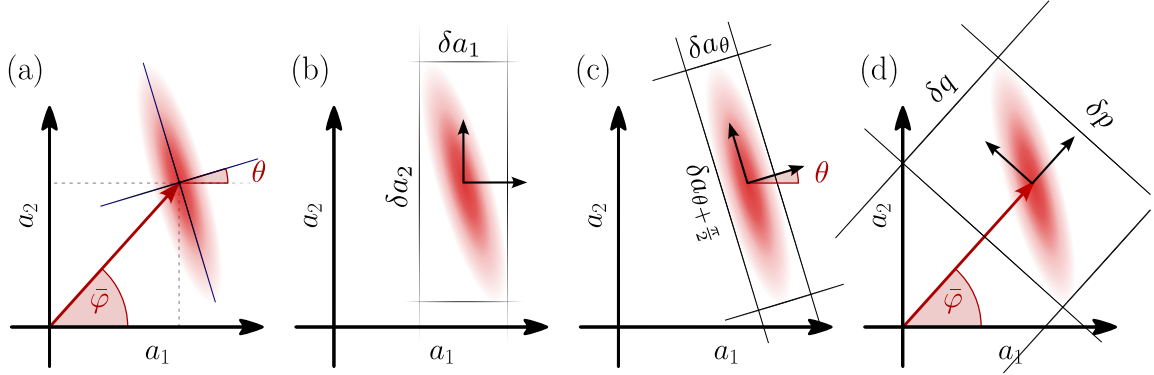


Fig. I.2 Phase-space representations of quantum states and transformations. (a) Wigner function of the vacuum state: a circular Gaussian centered at the origin, representing equal quantum fluctuations in both quadratures  $X_1$  and  $X_2$ . (b) Wigner function of a coherent state: a displaced circular Gaussian, showing a shift in phase space along an angle  $\varphi$  with unchanged, isotropic noise. (c) Wigner function of a squeezed vacuum state: an elliptical Gaussian centered at the origin, with reduced noise along a rotated quadrature  $X_\theta$  and increased noise in the orthogonal direction. (d) Wigner function of a displaced squeezed state: an ellipse shifted away from the origin, combining anisotropic fluctuations and a nonzero mean amplitude. The displacement angle  $\varphi$  and squeezing angle  $\theta$  are independent. **mistake on p and q**

tions along the squeezing axis are

$$\langle \delta \hat{a}_\theta^2 \rangle = e^{-2r}, \quad \langle \delta \hat{a}_{\theta+\pi/2}^2 \rangle = e^{2r}, \quad \text{Cov}(\hat{a}_\theta, \hat{a}_{\theta+\pi/2}) = 0, \quad (\text{I.30})$$

with uncertainty product  $\Delta \hat{a}_\theta \Delta \hat{a}_{\theta+\pi/2} = 1$  saturating the Heisenberg bound. The corresponding mean vector is

$$\langle \hat{\mathbf{u}}_\theta \rangle = 2 \begin{pmatrix} \text{Re}(\alpha e^{-i\theta}) \\ \text{Im}(\alpha e^{-i\theta}) \end{pmatrix}. \quad (\text{I.31})$$

### Covariance matrix:

Let  $\psi \equiv \phi - \theta$  be the measurement angle  $\phi$  relative to the squeezing axis  $\theta$ . For a displaced squeezed state, the covariance matrix is

$$\mathbf{V}_\phi = \mathbf{R}(\psi) \begin{pmatrix} e^{-2r} & 0 \\ 0 & e^{2r} \end{pmatrix} \mathbf{R}(\psi)^T. \quad (\text{I.32})$$

Expanding this explicitly gives

$$\mathbf{V}_\phi = \begin{pmatrix} \cosh 2r - \sinh 2r \cos 2\psi & \sinh 2r \sin 2\psi \\ \sinh 2r \sin 2\psi & \cosh 2r - \sinh 2r \sin 2\psi \end{pmatrix}. \quad (\text{I.33})$$

The covariance term is therefore

$$\text{Cov}(\hat{a}_\phi, \hat{a}_{\phi+\pi/2}) = \sinh 2r \sin 2(\phi - \theta), \quad (\text{I.34})$$

which vanishes when  $\sin 2(\phi - \theta) = 0$ , i.e.  $(\phi - \theta) \in \{0, \pi/2, \pi, \dots\}$ . Along these principal axes of squeezing,  $\mathbf{V}_\phi$  is diagonal.

**Amplitude and Phase squeezed states:** Considering a displaced squeezed state, two special cases are of interest: the amplitude squeezed state where  $\theta = \bar{\varphi}$  and the phase squeezed state where  $\theta = \bar{\varphi} + \pi/2$ . In the first case, the amplitude quadrature  $\hat{p}$  is squeezed, while the phase quadrature  $\hat{q}$  is anti-squeezed. In the second case, the phase quadrature is squeezed, while the amplitude quadrature is anti-squeezed. The covariance matrices for these states can be derived from Eq. (I.112) by setting  $\psi = 0$  or  $\psi = \pi/2$ , respectively.

#### Photon number statistics:

The mean and variance of the photon number operator  $\hat{N} = \hat{a}^\dagger \hat{a}$  in a displaced squeezed state are

$$\langle \hat{N} \rangle = |\alpha|^2 + \sinh^2 r, \quad \Delta N^2 = |\alpha|^2 \cosh 2r + \frac{1}{2} \sinh^2 2r. \quad (\text{I.35})$$

This shows that the squeezing operation increases the mean photon number of the coherent state by adding photons. Physically, this reflects the fact that generating squeezed light requires injecting energy into the system, so the squeezed vacuum contains correlated field excitations (photons) in even numbers. This is further seen by examining the photon-number distribution  $P_n$ : for a squeezed vacuum only even  $n$  occur, while displacement progressively repopulates the odd  $n$  and shifts weight to higher  $n$ , in agreement with the increase of  $\langle \hat{N} \rangle$  and  $\Delta N^2$  above.

#### I.1.4 Sidebands and Quantum Noises

##### Modulation picture

In realistic optical systems, the electromagnetic field is never perfectly monochromatic, nor isolated from its environment, nor static through time. Instead, it exhibits a finite spectral linewidth (stimulated emission, phase noise etc...), as well as non intentional/intentional modulations, all imprinted onto the carrier field. These effects cause the field amplitude and phase to evolve slowly compared to the optical frequency  $\omega_0$ .

As a result, the complex amplitude associated with each mode and described by the Schrodinger-picture annihilation operator  $\hat{a}$ , acquires an explicit time dependence beyond the standard fast-oscillating term  $e^{-i\omega_0 t}$ . It is often quoted as *modulation* picture in the litterature. We then promote the field vector to

$$\hat{\mathbf{a}} = \bar{\mathbf{a}} + \delta\hat{\mathbf{a}} \quad \rightarrow \quad \hat{\mathbf{a}}(t) = \bar{\mathbf{a}}(t) + \delta\hat{\mathbf{a}}(t) \quad (\text{I.36})$$

where the canonical commutation relations given in equation (I.14) becomes:

$$[\delta\hat{\mathbf{a}}(t), \delta\hat{\mathbf{a}}^\dagger(t')] = \sigma_{\mathbf{z}} \delta(t - t'). \quad (\text{I.37})$$

and the covariance matrix of the ammplitude-phase quadratures turns to

$$\mathbf{V}(t, t') = \begin{pmatrix} \langle \delta\hat{p}(t)\delta\hat{p}(t') \rangle & \text{Cov}(\hat{p}(t), \hat{q}(t')) \\ \text{Cov}(\hat{q}(t), \hat{p}(t')) & \langle \delta\hat{q}(t)\delta\hat{q}(t') \rangle \end{pmatrix} \delta(t - t') \quad (\text{I.38})$$

This time dependence allows us to track both slow classical modulations of the field  $\bar{\mathbf{u}}(t)$  and the intrinsic quantum fluctuations  $\delta\hat{\mathbf{u}}(t)$ . Note this is equivalent to the interaction picture where the reference angular frequency would be  $\omega_0$ , but where we also consider dynamical processes way slower than this frequency. Additionally, we will always consider the limit of weak fluctuations, where the quantum noise can be treated perturbatively around the classical field i.e.

$$|\bar{\alpha}(t)| \gg \Delta\hat{a}_\theta(t)$$

The resulting field operator can then be expressed as a

$$\begin{aligned} \hat{\mathbf{E}}(\mathbf{r}, t) = i\mathcal{E}_0 & \left[ \left[ \alpha(t) \mathbf{f}(\mathbf{r}) e^{-i\omega_0 t} - \alpha^*(t) \mathbf{f}^*(\mathbf{r}) e^{i\omega_0 t} \right] \right. \\ & \left. + \left[ \delta\hat{a}(t) \mathbf{f}(\mathbf{r}) e^{-i\omega_0 t} - \delta\hat{a}^\dagger(t) \mathbf{f}^*(\mathbf{r}) e^{i\omega_0 t} \right] \right] \end{aligned} \quad (\text{I.39})$$

**Amplitude Modulation (AM) :** Let the classical amplitude be modulated at  $\Omega_{\text{mod}}$  in amplitude:

$$\alpha(t) = \bar{\alpha} (1 + \epsilon_a \cos(\Omega_{\text{mod}} t)) \quad (\text{I.40})$$

with  $\epsilon_a \ll 1$ , the field amplitude modulation depth. While the DC term lives at frequency  $\omega_0$ , the modulation introduces sidebands at frequencies  $\omega_0 \pm \Omega_{\text{mod}}$ , seen by expanding the cosine:

$$\alpha(t) = \bar{\alpha} \left( 1 + \frac{\epsilon_a}{2} e^{i\Omega_{\text{mod}} t} + \frac{\epsilon_a}{2} e^{-i\Omega_{\text{mod}} t} \right) \quad (\text{I.41})$$

**Phase Modulation (PM) :** Now let the classical amplitude be modulated in phase at

frequency  $\Omega_{\text{mod}}$ :

$$\alpha(t) = \bar{\alpha} e^{i\epsilon_\phi \cos(\Omega_{\text{mod}} t)} \quad (\text{I.42})$$

with  $\epsilon_\phi \ll 1$  the field phase modulation depth. Expanding to first order in  $\epsilon_\phi$  gives:

$$\alpha(t) \approx \bar{\alpha} \left( 1 + \frac{i\epsilon_\phi}{2} e^{i\Omega_{\text{mod}} t} + \frac{i\epsilon_\phi}{2} e^{-i\Omega_{\text{mod}} t} \right) \quad (\text{I.43})$$

While the carrier term lives at frequency  $\omega_0$ , the modulation introduces sidebands at  $\omega_0 \pm \Omega_{\text{mod}}$ , both shifted in phase by  $\pi/2$  relative to the carrier.

In both cases, amplitude or phase modulations, the field contains a carrier at frequency  $\omega$  and two sidebands at  $\omega \pm \Omega$ . Amplitude modulation results in sidebands that are in phase with the carrier, while phase modulation produces sidebands with a  $\pm\pi/2$  phase shift relative to the carrier. We also note a general modulation process as :

$$\alpha(t) = \bar{\alpha} (1 + \varepsilon(t)) \quad (\text{I.44})$$

where  $\varepsilon(t) \in \mathbb{C}$  is a modulation function that weakly modulates the complex amplitude in time, and that features information about the modulation frequency and depth. It then follows that the linearized amplitude-phase operators can be expressed as

$$\hat{\mathbf{u}}_{\bar{\varphi}}(t) = 2|\bar{\alpha}| \begin{pmatrix} 1 \\ 0 \end{pmatrix} + 2|\bar{\alpha}| \begin{pmatrix} \text{Re}(\varepsilon(t)) \\ \text{Im}(\varepsilon(t)) \end{pmatrix} + \begin{pmatrix} \delta\hat{p}(t) \\ \delta\hat{q}(t) \end{pmatrix} \quad (\text{I.45})$$

## Fourier Domain

To deal with noise spectra, we need to rewrite the various quadratures defined in the previous sections in the Fourier domain, where each frequency component is referred to as a *sideband*.

The Fourier transform of the field vector is defined as

$$\begin{aligned} \hat{\mathbf{a}}[\Omega] &= \int_{-\infty}^{+\infty} dt e^{i\Omega t} \hat{\mathbf{a}}(t) \\ \hat{\mathbf{a}}(t) &= \frac{1}{2\pi} \int_{-\infty}^{+\infty} d\Omega e^{-i\Omega t} \hat{\mathbf{a}}[\Omega] \end{aligned} \quad (\text{I.46})$$

where  $\Omega \ll \omega_0$  is the sideband frequency relative to the so called *carrier* frequency  $\omega_0$ . Add something on the true integral bound i.e. bandwidth B In this definition, a notable property is that the hermitian conjugate in the time domain translates to a frequency inversion in the Fourier domain:

$$[\hat{a}(t)]^\dagger = \hat{a}^\dagger(t), \quad [\hat{a}[\Omega]]^\dagger = \hat{a}^\dagger[-\Omega]. \quad (\text{I.47})$$

To lighten the notation we will use  $\hat{a}^\dagger[\pm\Omega] = \hat{a}_\pm$ . Carrying out the linearization in the

Fourier domain, we have

$$\hat{\mathbf{a}}[\Omega] = \begin{pmatrix} \bar{\alpha}_+ \\ \bar{\alpha}_-^* \end{pmatrix} + \begin{pmatrix} \delta\hat{a}_+ \\ \delta\hat{a}_-^\dagger \end{pmatrix} = \bar{\mathbf{a}}[\Omega] + \delta\hat{\mathbf{a}}[\Omega] \quad (\text{I.48})$$

with the fluctuations commutator reading

$$[\delta\hat{\mathbf{a}}[\Omega], \delta\hat{\mathbf{a}}[\Omega']^\dagger] = \sigma_z \delta(\Omega + \Omega'). \quad (\text{I.49})$$

The quadrature operators in the Fourier domain are then written as

$$\begin{aligned} \hat{\mathbf{u}}_\phi[\Omega] &= \mathbf{R}(\phi) \boldsymbol{\Gamma} \bar{\mathbf{a}}[\Omega] + \mathbf{R}(\phi) \boldsymbol{\Gamma} \delta\hat{\mathbf{a}}[\Omega] \\ &= \underbrace{2|\bar{\alpha}| \begin{pmatrix} \cos(\bar{\varphi} - \phi) \\ \sin(\bar{\varphi} - \phi) \end{pmatrix} \delta(\Omega)}_{\text{classical part}} + \underbrace{\begin{pmatrix} \delta\hat{a}_\phi[\Omega] \\ \delta\hat{a}_{\phi+\pi/2}[\Omega] \end{pmatrix}}_{\text{quantum fluctuations}} \end{aligned} \quad (\text{I.50})$$

such that the amplitude-phase quadrature vector reads

$$\hat{\mathbf{u}}_{\bar{\varphi}}[\Omega] = 2|\bar{\alpha}| \begin{pmatrix} 1 \\ 0 \end{pmatrix} \delta(\Omega) + \begin{pmatrix} \delta\hat{p}[\Omega] \\ \delta\hat{q}[\Omega] \end{pmatrix} \quad \text{with} \quad \begin{pmatrix} \delta\hat{p}[\Omega] \\ \delta\hat{q}[\Omega] \end{pmatrix} = \begin{pmatrix} \delta\hat{a}_+ + \delta\hat{a}_-^\dagger \\ i(\delta\hat{a}_-^\dagger - \delta\hat{a}_+) \end{pmatrix} \quad (\text{I.51})$$

This very way of writing the field quadratures is known as the *two-photon* formalism, introduced by Caves and Schumaker [?, ?]. Here, we wrote down a vector, linearized form, useful to compute spectra numerically (see section ??). Throughout the litterature, the amplitude-phase two-photon quadratures are called differently, namely  $(a_I, a_Q)$  (Caves and Schumaker),  $(X_1, X_2)$  (Gerry and Knight),  $(X, Y)$  (Bachor and Ralph) or  $(x, p)$  (Weedbrook et al.). We chose the  $p, q$  convention to perpetuate the convention used at LKB.

**Note:** In the modulation picture, fluctuations in the time domain appear as symmetric sidebands at  $+\Omega$  and  $-\Omega$ . Any experimentally accessible, real signal arises from the interference of these two sidebands (quadratures in homodyne detection, intensity fluctuations, photocurrent spectra); equivalently, Hermiticity in time forces Fourier components to couple  $+\Omega$  with  $-\Omega$ . Packaging the field as the two-photon vector  $(\hat{a}[\Omega], \hat{a}^\dagger[-\Omega])^T$  therefore groups exactly the two degrees of freedom that generate a single measurable fluctuation at frequency  $\Omega$ . This makes correlations between the sidebands (which are the essence of frequency-dependent squeezing) explicit and ensures that quadrature spectra remain manifestly real. By contrast, the vector  $(\hat{a}[\Omega], \hat{a}^\dagger[\Omega])^T$  is convenient for per-frequency photon-number or passive-scattering calculations, but it obscures the intrinsic pairing required to form real observables, forcing one to carry  $-\Omega$  separately. For the noise-spectral analysis pursued here, the sideband-pair representation is thus the phenomenologically natural and

algebraically minimal choice.

### Modulations in Fourier space

Computing the Fourier transform for amplitude and phase modulations yields

$$\begin{aligned}\varepsilon^{AM}(\Omega) &= \frac{\epsilon_a}{2} (\delta(\Omega - \Omega_{\text{mod}}) + \delta(\Omega + \Omega_{\text{mod}})) \\ \varepsilon^{PM}(\Omega) &= \frac{i\epsilon_\phi}{2} (\delta(\Omega - \Omega_{\text{mod}}) + \delta(\Omega + \Omega_{\text{mod}}))\end{aligned}\quad (\text{I.52})$$

And the quadrature operators of a modulated field can be expressed as

$$\hat{\mathbf{u}}_{\bar{\varphi}}[\Omega] = 2|\bar{\alpha}| \begin{pmatrix} 1 \\ 0 \end{pmatrix} \delta(\Omega) + 2|\bar{\alpha}| \begin{pmatrix} \text{Re}(\varepsilon[\Omega]) \\ \text{Im}(\varepsilon[\Omega]) \end{pmatrix} + \begin{pmatrix} \delta\hat{p}[\Omega] \\ \delta\hat{q}[\Omega] \end{pmatrix} \quad (\text{I.53})$$

### Vacuum fluctuations

Considering a vacuum state or a coherent state, the expectation values of the quadrature fluctuations moments in the Fourier domain are

$$\langle \delta\hat{\mathbf{u}}_\phi[\Omega] \rangle = \mathbf{0}, \quad \langle \delta\hat{\mathbf{u}}_\phi[\Omega] \delta\hat{\mathbf{u}}_\phi^T[\Omega'] \rangle = 2\pi\delta(\Omega + \Omega')\mathbf{1} \quad (\text{I.54})$$

### Noise Spectra

In this work, we will be interested in the amplitude and phase noise spectra, defined as

$$\mathbf{S}_{\bar{\varphi}}[\Omega] = \frac{1}{2\pi} \int \delta\Omega' \langle \delta\hat{\mathbf{u}}_{\bar{\varphi}}[\Omega] \delta\hat{\mathbf{u}}_{\bar{\varphi}}^T[\Omega'] \rangle = \frac{1}{2\pi} \int \delta\Omega' \begin{pmatrix} \langle \delta\hat{p}[\Omega] \delta\hat{p}[\Omega'] \rangle & \langle \delta\hat{p}[\Omega] \delta\hat{q}[\Omega'] \rangle \\ \langle \delta\hat{q}[\Omega] \delta\hat{p}[\Omega'] \rangle & \langle \delta\hat{q}[\Omega] \delta\hat{q}[\Omega'] \rangle \end{pmatrix} \quad (\text{I.55})$$

In our way of writing it, we include all time dependent processes inside de fluctuation operators i.e.  $\varepsilon(t)$  and  $\delta\hat{p}(t)$ ,  $\delta\hat{q}(t)$  in the case of quadrature operators, as all terms in  $\delta(\Omega)$  contribute to the DC part of the spectrum.

We illustrate this by computing the spectra of a coherent field modulated in amplitude. The amplitude-phase quadrature fluctuation part reads

$$\delta\hat{\mathbf{u}}_{\bar{\varphi}}[\Omega] = |\bar{\alpha}|\epsilon_a \begin{pmatrix} \delta(\Omega - \Omega_{\text{mod}}) + \delta(\Omega + \Omega_{\text{mod}}) \\ 0 \end{pmatrix} + \begin{pmatrix} \delta\hat{p}[\Omega] \\ \delta\hat{q}[\Omega] \end{pmatrix} \quad (\text{I.56})$$

such that its covariance matrix reads

$$\mathbf{S}_{\bar{\varphi}}[\Omega] = 2|\bar{\alpha}|^2\epsilon_a^2 \left[ \delta(\Omega - \Omega_{\text{mod}}) + \delta(\Omega + \Omega_{\text{mod}}) \right] \begin{pmatrix} 1 & 0 \\ 0 & 0 \end{pmatrix} + \mathbf{1} \quad (\text{I.57})$$

As seen in the above expression, the covariance matrix display a sum of dirac functions corresponding to a classical amplitude modulation of the field, as well as a flat vacuum noise across all frequencies.

### Linear Optical Systems

As we will develop further in the next section, the output fields of various optical systems can be expressed in a general linear form as

$$\delta\hat{\mathbf{u}}_{\text{out}}[\Omega] = \mathbf{T}[\Omega] \delta\hat{\mathbf{u}}_{\text{in}}[\Omega] + \mathbf{L}[\Omega] \delta\hat{\mathbf{u}}_{\text{vac}}[\Omega]. \quad (\text{I.58})$$

where  $\mathbf{T}[\Omega]$  and  $\mathbf{L}[\Omega]$  are  $2 \times 2$  transfer matrices. The input and vacuum fields are assumed to be in the vacuum state, as well as being uncorrelated such that

$$\begin{aligned} \langle \delta\hat{\mathbf{u}}_{\text{in}}[\Omega] \delta\hat{\mathbf{u}}_{\text{in}}^T[\Omega'] \rangle &= 2\pi\delta(\Omega + \Omega') \mathbf{S}_{\text{in}}[\Omega] \\ \langle \delta\hat{\mathbf{u}}_{\text{vac}}[\Omega] \delta\hat{\mathbf{u}}_{\text{vac}}^T[\Omega'] \rangle &= 2\pi\delta(\Omega + \Omega') \mathbf{1} \\ \langle \delta\hat{\mathbf{u}}_{\text{in}}[\Omega] \delta\hat{\mathbf{u}}_{\text{vac}}^T[\Omega'] \rangle &= \mathbf{0} \end{aligned} \quad (\text{I.59})$$

so one can write

$$\langle \delta\hat{\mathbf{u}}_{\text{out}}[\Omega] \delta\hat{\mathbf{u}}_{\text{out}}^T[\Omega'] \rangle = 2\pi\delta(\Omega + \Omega') \left( \mathbf{T}[\Omega] \mathbf{S}_{\text{in}}[\Omega] \mathbf{T}^T[\Omega'] + \mathbf{L}[\Omega] \mathbf{L}^T[\Omega'] \right). \quad (\text{I.60})$$

Computing the noise spectra is then straightforward :

$$\mathbf{S}_{\text{out}}[\Omega] = \mathbf{T}[\Omega] \mathbf{S}_{\text{in}}[\Omega] \mathbf{T}^\dagger[\Omega] + \mathbf{L}[\Omega] \mathbf{L}^\dagger[\Omega] \quad (\text{I.61})$$

where  $\mathbf{T}^T[-\Omega] = \mathbf{T}^\dagger[\Omega]$ ,  $\mathbf{L}^T[-\Omega] = \mathbf{L}^\dagger[\Omega]$ , and  $\mathbf{S}_{\text{vac}}[\Omega] = \mathbf{1}$  for vacuum inputs.

For an arbitrary quadrature angle  $\phi$ , one can simply rotate the transfer matrices as

$$\mathbf{T}_\phi[\Omega] = \mathbf{R}(\phi) \mathbf{T}[\Omega] \mathbf{R}(-\phi), \quad \mathbf{L}_\phi[\Omega] = \mathbf{R}(\phi) \mathbf{L}[\Omega] \mathbf{R}(-\phi) \quad (\text{I.62})$$

such that

$$\mathbf{S}_{\text{out},\phi}[\Omega] = \mathbf{T}_\phi[\Omega] \mathbf{S}_{\text{in},\phi}[\Omega] \mathbf{T}_\phi^\dagger[\Omega] + \mathbf{L}_\phi[\Omega] \mathbf{L}_\phi^\dagger[\Omega] \quad (\text{I.63})$$

#### I.1.5 Quantum Sideband Diagram

Starting with the simplest case : the vacuum/coherent state.

## I.2 Cavities

Optical cavities are at the heart of this work, as they are used to coherently enhance the light-matter interaction in various systems, and also to filter and manipulate quantum states of light. In this section, we review the basic properties of optical cavities, their resonance conditions, and we derive the covariance matrices of their output fields.

### I.2.1 Cavity Geometries and Stability Conditions

An optical cavity is a structure that *traps* photons by means of reflection between two or more mirrors. They can be either standing wave cavities, where the light bounces back and forth between two mirrors, or traveling wave cavities, where the light circulates in a loop. In both cases, the cavity supports discrete resonant modes determined by its geometry and the boundary conditions imposed by the mirrors. The stability criteria of a specific cavity configuration is derived considering the round trip ABCD matrix of the cavity describing how the complex beam parameter  $q(z)$  introduced in (I.2) transforms after one round trip. The stability condition then simply reads as  $-1 < (A + D)/2 < 1$ . In the case of planar - travelling wave cavities, one needs to consider both the tangential and sagittal planes, as these cavities are astigmatic. The stricter condition, generally the sagittal plane one, then defines the stability range of the cavity.

**Linear standing wave cavities:** We first consider the two linear cavities used in this work, namely a confocal cavity (Fig I.10.(a)) with two identical concave mirrors, and a plano-concave cavity with one flat mirror and one concave mirror (Fig I.10.(b)). Using the ABCD formalism for a confocal cavity of length  $L$  formed by two identical mirrors of radii of curvature  $R$ , the stability condition reads

$$0 < L < 2R \quad (\text{I.64})$$

For the plano-concave cavity, the stability condition reads

$$0 < L < R \quad (\text{I.65})$$

**Planar traveling wave cavities:** We now consider a triangular cavity formed by two concave mirrors of radius of curvature  $R$  and one flat mirror (Fig I.10.(c)). The stability condition reads

$$0 < L_{rt} < 2R \cos(\theta) \quad (\text{I.66})$$

where  $L_{rt} = 2L + l$  is the cavity round trip length, and  $\theta$  is the angle of incidence of the beam onto the curved mirror. This condition is the sagittal one, and is more stringent than

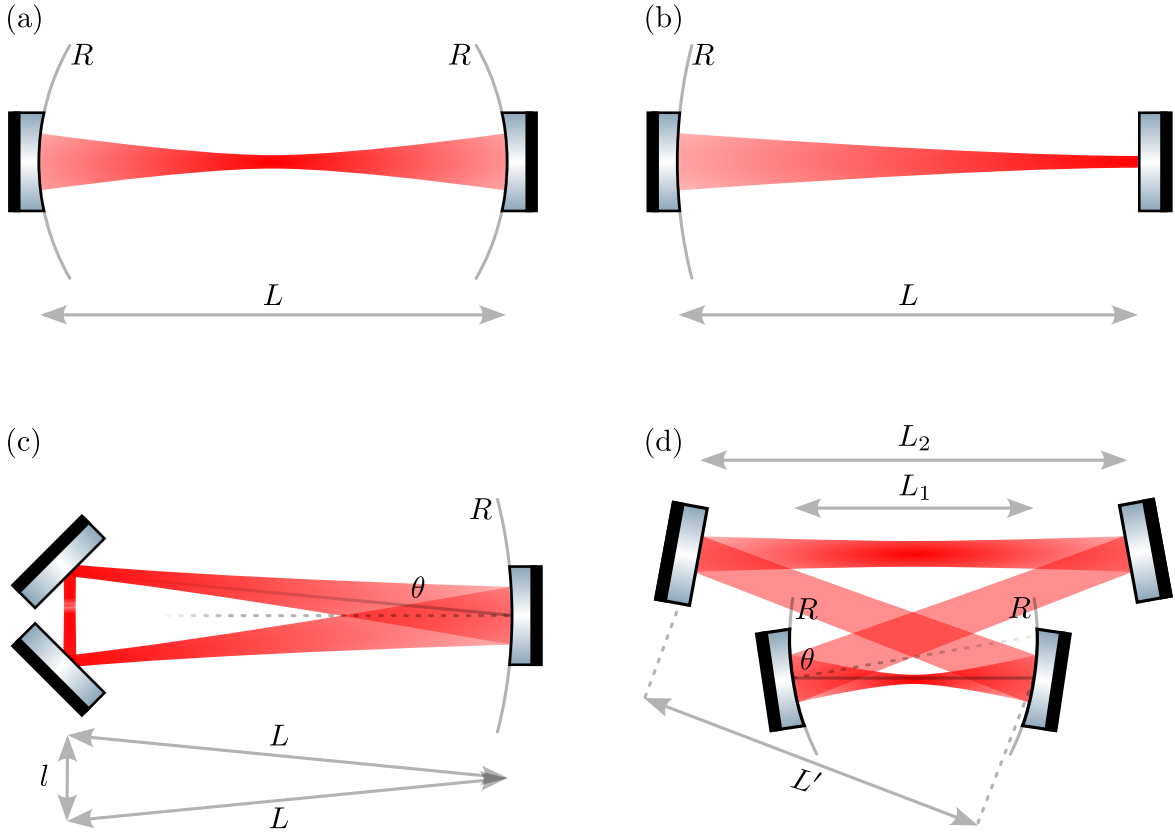


Fig. I.3 Yes

the tangential one.

Considering now a bow-tie cavity formed by two concave mirrors of radius of curvature  $R$  and two flat mirrors (Figure I.10.(d)), the full stability condition reads

$$0 < \left(1 - \frac{L_1 + 2L'}{R \cos \theta}\right) \left(1 - \frac{L_2}{R \cos \theta}\right) < 1 \quad (\text{I.67})$$

where  $L_1$  is the distance between the two concave mirrors,  $L_2$  the distance between the two flat mirrors, and  $L'$  the distance between a concave and a flat mirror (assuming a symmetric cavity). A simple design rule guaranteeing stability is then to set  $L_1 + 2L' < R \cos \theta$  and  $L_2 < R \cos \theta$ .

### I.2.2 Cavity Resonances

If the cavity is stable, it will then feature a discrete set of resonant modes everytime the cavity length is an integer multiple of half the wavelength  $\lambda/2$  (standing wave cavity) or the

wavelength  $\lambda$  (traveling wave cavity). In the frequency domain, modes are spaced by the free spectral range  $\omega_{\text{FSR}}$  of the cavity, defined as

$$\omega_{\text{FSR}} = \frac{\pi c}{L} \quad (\text{linear cavity}), \quad \omega_{\text{FSR}} = \frac{2\pi c}{L_{rt}} \quad (\text{traveling wave cavity}) \quad (\text{I.68})$$

such that the resonant frequencies are given by

$$\omega_m = m \omega_{\text{FSR}}, \quad m \in \mathbb{N} \quad (\text{I.69})$$

and the cavity is on resonance when the input laser frequency  $\omega_0$  matches one of the resonant frequencies  $\omega_m$  i.e.  $\omega_0 = \omega_m$ . To achieve this, one can either tune the laser frequency or the cavity length. In our experiments, we use the second option by mounting one of the cavity mirrors on a piezoelectric actuator. Changing the cavity length  $L$  by  $\delta L$  shifts the resonant frequencies by

$$\delta\omega_m = -m \frac{\pi c}{L^2} \delta L = -\frac{\omega_m}{L} \delta L \quad (\text{I.70})$$

### I.2.3 Mode-Matching

A cavity also supports  $TEM_{mn}$  transverse modes, each with a specific spatial profile and resonant frequency. The resonant frequencies of these transverse modes are shifted relative to the fundamental mode by an amount that depends on the cavity geometry and the mode indices  $(m, n)$ . Coupling an incoming beam into a stable optical cavity requires that the spatial mode of the beam matches that of the cavity. This means that the mode function of the incoming beam, assumed to be a  $TEM_{00}$  Gaussian mode  $f_0(\mathbf{r})$ , must overlap with the cavity's fundamental mode  $f'_0(\mathbf{r})$ . If the basis functions are not perfectly aligned, the incoming field can be expanded in the orthonormal basis of cavity modes as

$$f_0(\mathbf{r}) = c_0 f'_0(\mathbf{r}) + \sum_{m>0} c_m f'_m(\mathbf{r}), \quad (\text{I.71})$$

where the coefficients  $c_m$  quantify the projection of the incident field onto the cavity eigenmodes. Only the component  $c_0 f'_0$  couples efficiently to the fundamental cavity mode due to the mirror geometry, while any mismatch excites higher-order transverse modes  $f'_m$ . The mode-matching procedure therefore consists in maximizing the overlap integral

$$\eta = \left| \int d^3\mathbf{r} f_0^*(\mathbf{r}) f'_0(\mathbf{r}) \right|^2, \quad (\text{I.72})$$

which ensures that essentially all the incoming photons populate the desired cavity mode, while suppressing excitation of spurious modes.

regarding the resonant lengths for which a speci

#### I.2.4 Simple Cavities

We consider a single field cavity mode described by the annihilation operator  $\hat{a}$ , interacting with several independent noise inputs. The system is governed by a Hamiltonian

$$\hat{H} = -\hbar\Delta\hat{a}^\dagger\hat{a} \quad (\text{I.73})$$

with  $\Delta \equiv \omega_0 - \omega_c$  the cavity detuning to the laser frequency, and each input introduces dissipation characterized by a decay rate  $\kappa_i = T_i/\tau$ , with  $T_i$  the power transmittivity of the mirror and  $\tau = 2L/c$  the roundtrip time of the cavity. This is we consider an input coupler (mirror) with decay rate  $\kappa_1$  and an output coupler (mirror) with decay rate  $\kappa_2$ . The laser field is shone onto the cavity by the input coupler.

In the modulation picture, the dynamics of  $\hat{a}$  is given by the Quantum Langevin Equation (QLE):

$$\begin{aligned} \frac{d}{dt}\hat{a}(t) &= -\frac{i}{\hbar}[\hat{a}, \hat{H}] - \frac{\kappa}{2}\hat{a}(t) + \sqrt{\kappa_1}\hat{a}_{\text{in}}(t) + \sqrt{\kappa_2}\delta\hat{a}_{\text{vac}}(t) + \sqrt{\kappa_0}\delta\hat{a}_l(t) \\ &= -\left(\frac{\kappa}{2} - i\Delta\right)\hat{a}(t) + \sqrt{\kappa_1}\hat{a}_{\text{in}}(t) + \sqrt{\kappa_2}\delta\hat{a}_{\text{vac}}(t) + \sqrt{\kappa_0}\delta\hat{a}_l(t) \end{aligned} \quad (\text{I.74})$$

where  $\kappa = \kappa_0 + \kappa_1 + \kappa_2$  is the total decay rate, with  $\kappa_0 = \gamma/\tau$  and  $\delta\hat{a}_l(t)$  the rate and fluctuation operator of additional losses. Here losses  $\gamma$  have ppm units. Another key element to deriving both steady state behaviour as well as quadrature spectra is the input-output formula given by:

$$\hat{a}_r = \sqrt{\kappa_1}\hat{a} - \hat{a}_{\text{in}}, \quad \hat{a}_t = \sqrt{\kappa_2}\hat{a} - \delta\hat{a}_{\text{vac}} \quad (\text{I.75})$$

for both the reflected and transmitted field. In the input-output formula, the  $\hat{a}_{\text{in}}$  refers to the field incoming on the coupler considered, which are simple vacuum fluctuations on the output coupler since we don't shine the laser by this port.

As introduced in the previous subsection, one can split the annihilation operator in a mean field part  $\alpha$  and a fluctuation part  $\delta\hat{\mathbf{a}}(t)$  (vector form) such that this equation turns into two i.e. a scalar differential equation, and an operator differentail equation, that is:

$$\begin{cases} 0 = -\left(\frac{\kappa}{2} - i\Delta\right)\bar{\alpha} + \sqrt{\kappa_1}\bar{\alpha}_{\text{in}} \\ \delta\dot{\hat{\mathbf{a}}}(t) = -\begin{pmatrix} \kappa/2 - i\Delta & 0 \\ 0 & \kappa/2 + i\Delta \end{pmatrix}\delta\hat{\mathbf{a}}(t) + \sqrt{\kappa_1}\delta\hat{a}_{\text{in}}(t) + \sqrt{\kappa_2}\delta\hat{a}_{\text{vac}}(t) + \sqrt{\kappa_0}\delta\hat{a}_l(t) \end{cases} \quad (\text{II.62})$$

**Mean field solution (Static case):** Taking the first scalar equation and expressing the

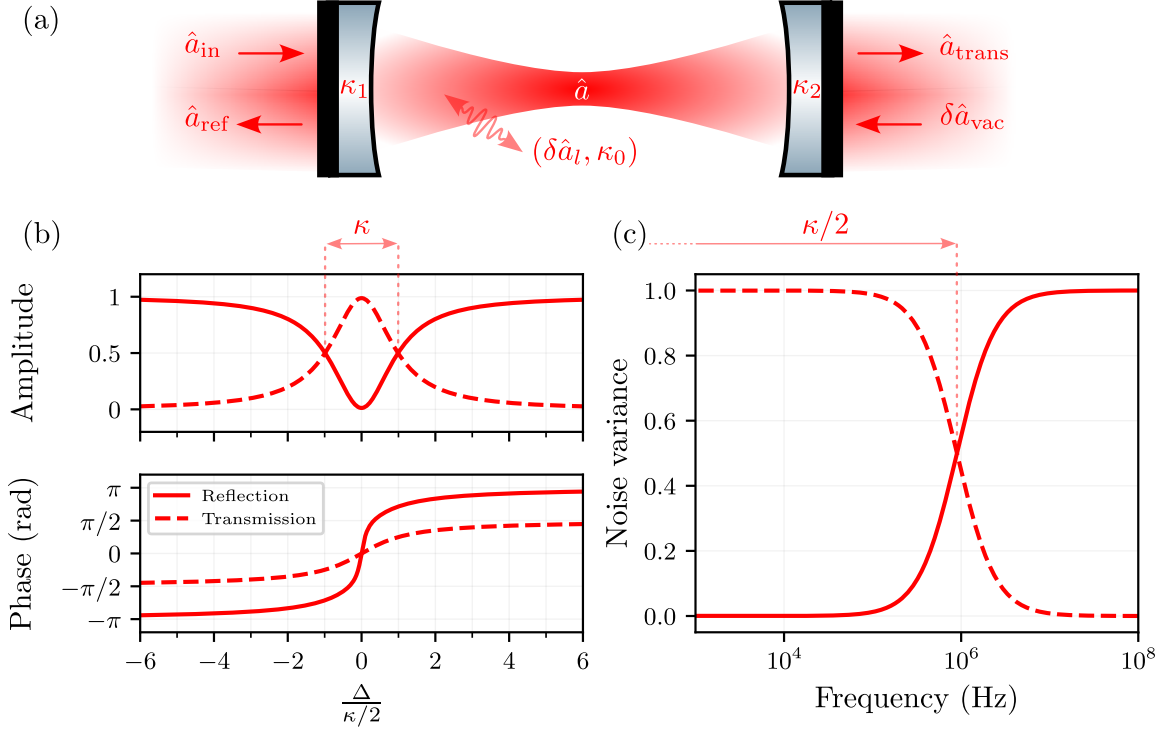


Fig. I.4 Yes

mean intracavity field gives

$$\bar{\alpha} = \frac{\sqrt{\kappa_1}}{\kappa/2 - i\Delta} \bar{\alpha}_{\text{in}} \quad (\text{I.76})$$

Patching it up with the input-output formula this gives

$$\bar{\alpha}_r = \left( \frac{\kappa_1}{\kappa/2 - i\Delta} - 1 \right) \bar{\alpha}_{\text{in}} \quad \bar{\alpha}_t = \frac{\sqrt{\kappa_1 \kappa_2}}{(\kappa/2 - i\Delta)} \bar{\alpha}_{\text{in}}. \quad (\text{I.77})$$

The reflection and transmission coefficients are then

$$R(\Delta) = \left| \frac{\bar{\alpha}_r}{\bar{\alpha}_{\text{in}}} \right|^2 = \frac{(\kappa_1 - \kappa/2)^2 + \Delta^2}{(\kappa/2)^2 + \Delta^2} \quad T(\Delta) = \left| \frac{\bar{\alpha}_t}{\bar{\alpha}_{\text{in}}} \right|^2 = \frac{\kappa_1 \kappa_2}{(\kappa/2)^2 + \Delta^2}. \quad (\text{I.78})$$

The cavity linewidth (FWHM) is then given by  $\kappa$ , as illustrated in Fig I.4.(b). Plugging back the expression of  $\kappa_i = T_i/\tau$  in the reflection coefficient, we have

$$R(\pm\infty) = 1 \quad R(0) = \left( \frac{T_1 - T_2 - \gamma}{T_1 + T_2 + \gamma} \right)^2 \quad (\text{I.79})$$

such that the relative depth of the resonance dip gives us information about the cavity losses

and couplings. In particular, the resonance dip vanishes when  $T_1 = T_2 + \gamma$ , which is the so called *impedance matching* condition: no light is reflected at resonance and all of it is transmitted or lost.

We also define the cavity finesse  $\mathcal{F}$ , which is a measure of the sharpness of the resonance peaks relative to its FSR, as

$$\mathcal{F} = \frac{\omega_{\text{FSR}}}{\kappa} = \frac{\pi c}{L\kappa} = \frac{2\pi}{T_1 + T_2 + \gamma} \quad (\text{I.80})$$

which also gives the average number of round trips a photon makes before escaping the cavity i.e.  $\langle n_{rt} \rangle = \mathcal{F}/\pi$ . For a given cavity length (so same FSR), the higher the finesse, the longer the photon lifetime in the cavity  $\kappa^{-1}$ .

### Mean field solution (Dynamical case):

We now let the detuning vary linearly in time, and express it in units of cavity bandwidth as  $\Delta(t) = \Delta_0 + v\frac{\kappa^2}{2}t$  where we defined  $v$  as the sweep speed in units of cavity bandwidth per  $\kappa^{-1}$ . The intracavity field yields the standard differential equation

$$\dot{\alpha}(t) = -\left(\frac{\kappa}{2} - i\left(\Delta_0 + \frac{v\kappa^2}{2}t\right)\right)\bar{\alpha}(t) + \sqrt{\kappa_1}\bar{\alpha}_{\text{in}} \quad (\text{I.81})$$

This is solved by the means of integration factor method, such that we find

$$\begin{aligned} \alpha(t) &= \exp\left[\left(-\frac{\kappa}{2} + i\Delta_0\right)t + i\frac{v\kappa^2}{4}t^2\right] \\ &\times \left[\alpha(0) + \sqrt{\kappa_1}\bar{\alpha}_{\text{in}} \int_0^t \exp\left(\left(\frac{\kappa}{2} - i\Delta_0\right)s - i\frac{v\kappa^2}{4}s^2\right) ds\right]. \end{aligned} \quad (\text{I.82})$$

This expression describes the transient response of the intracavity field as the detuning is swept through resonance. When scanning over the cavity resonance at a rate exceeding the cavity bandwidth, photons at various detuning start to build up in the cavity without reaching the steady state value. This results in a characteristic asymmetric lineshape, where these different *colored* photons start beating against each other, leading to oscillations in the transmitted and reflected intensities. This is illustrated in Fig I.4.(c) for different sweep speeds. The above does feature an analytical formula involving error functions erf, such that can either fit the data by performing a numerical integration or the analytical formula. However if the data array feature too few points numerical integration becomes numerically costly. **figure to do**

**Fluctuations solution:** To derive the covariance matrix we go to Fourier space such that

$$\mathbf{M}_\Delta \delta \hat{\mathbf{a}}[\Omega] = \sqrt{\kappa_1} \delta \hat{\mathbf{a}}_{\text{in}}[\Omega] + \sqrt{\kappa_2} \delta \hat{\mathbf{a}}_{\text{vac}}[\Omega] + \sqrt{\kappa_0} \delta \hat{\mathbf{a}}_{\text{l}}[\Omega] \quad (\text{I.83})$$

with

$$\mathbf{M}_\Delta = \begin{pmatrix} \kappa/2 - i(\Delta + \Omega) & 0 \\ 0 & \kappa/2 + i(\Delta - \Omega) \end{pmatrix}$$

The intracavity field fluctuations are then given by

$$\delta \hat{\mathbf{a}}[\Omega] = \mathbf{M}_\Delta^{-1} \left( \sqrt{\kappa_1} \delta \hat{\mathbf{a}}_{\text{in}}[\Omega] + \sqrt{\kappa_2} \delta \hat{\mathbf{a}}_{\text{vac}}[\Omega] + \sqrt{\kappa_0} \delta \hat{\mathbf{a}}_{\text{l}}[\Omega] \right) \quad (\text{I.84})$$

and the reflected and transmitted fields read

$$\begin{aligned} \delta \hat{\mathbf{a}}_{\text{r}}[\Omega] &= (\kappa_1 \mathbf{M}_\Delta^{-1} - \mathbf{1}) \delta \hat{\mathbf{a}}_{\text{in}}[\Omega] + \sqrt{\kappa_1} \mathbf{M}_\Delta^{-1} (\sqrt{\kappa_2} \delta \hat{\mathbf{a}}_{\text{vac}}[\Omega] + \sqrt{\kappa_0} \delta \hat{\mathbf{a}}_{\text{l}}[\Omega]) \\ \delta \hat{\mathbf{a}}_{\text{t}}[\Omega] &= \sqrt{\kappa_2} \mathbf{M}_\Delta^{-1} (\sqrt{\kappa_1} \delta \hat{\mathbf{a}}_{\text{in}}[\Omega] + \sqrt{\kappa_0} \delta \hat{\mathbf{a}}_{\text{l}}[\Omega]) + (\kappa_2 \mathbf{M}_\Delta^{-1} - \mathbf{1}) \delta \hat{\mathbf{a}}_{\text{vac}}[\Omega] \end{aligned} \quad (\text{I.85})$$

Using  $\delta \hat{\mathbf{a}} = \mathbf{\Gamma}^{-1} \delta \hat{\mathbf{u}}$  the reflected and transmitted quadratures read

$$\begin{aligned} \delta \hat{\mathbf{u}}_{\text{r}}[\Omega] &= (\kappa_1 \mathbf{\Gamma M}_\Delta^{-1} \mathbf{\Gamma}^{-1} - \mathbf{1}) \delta \hat{\mathbf{u}}_{\text{in}}[\Omega] + \sqrt{\kappa_1} \mathbf{\Gamma M}_\Delta^{-1} \mathbf{\Gamma}^{-1} (\sqrt{\kappa_2} \delta \hat{\mathbf{u}}_{\text{vac}}[\Omega] + \sqrt{\kappa_0} \delta \hat{\mathbf{u}}_{\text{l}}[\Omega]) \\ \delta \hat{\mathbf{u}}_{\text{t}}[\Omega] &= \sqrt{\kappa_2} \mathbf{\Gamma M}_\Delta^{-1} \mathbf{\Gamma}^{-1} (\sqrt{\kappa_1} \delta \hat{\mathbf{u}}_{\text{in}}[\Omega] + \sqrt{\kappa_0} \delta \hat{\mathbf{u}}_{\text{l}}[\Omega]) + (\kappa_2 \mathbf{\Gamma M}_\Delta^{-1} \mathbf{\Gamma}^{-1} - \mathbf{1}) \delta \hat{\mathbf{u}}_{\text{vac}}[\Omega] \end{aligned} \quad (\text{I.86})$$

where the matrix product above reads

$$\mathbf{\Gamma M}_\Delta^{-1} \mathbf{\Gamma}^{-1} = \frac{1}{(\kappa/2 - i\Omega)^2 + \Delta^2} \begin{pmatrix} \kappa/2 - i\Omega & \Delta \\ -\Delta & \kappa/2 - i\Omega \end{pmatrix}.$$

The structure above is the engine behind frequency-dependent squeezing. On resonance, we have

$$\mathbf{M}_0^{-1} = \frac{1}{\kappa/2 - i\Omega} \mathbf{I} \implies \mathbf{\Gamma M}_0^{-1} \mathbf{\Gamma}^{-1} = \frac{1}{\kappa/2 - i\Omega} \mathbf{I}$$

causing symmetric sidebands around the carrier to be filtered identically both in amplitude and phase — so the quadrature along which these sidebands are correlated (if considering squeezed correlations) remains the same at all frequencies. The moment the cavity is detuned, the  $\mathbf{\Gamma M}_\Delta^{-1} \mathbf{\Gamma}^{-1}$  off-diagonal terms asymmetrically mix the upper and lower sidebands; in the two-photon picture this is a frequency-dependent rotation and scaling of the  $(p, q)$  basis. The amplitude (Lorentzian) part sets how strongly each sideband passes, while the phase accrued inside the cavity sets the rotation angle that now varies with  $\Omega$ . A broadband field with a single squeezing angle at the input is therefore converted into an output whose squeezing angle “twists” with frequency: near one band it can align with the phase

quadrature, and at another it can align with the amplitude quadrature. This is exactly the mechanism exploited by filter cavities in precision interferometry: by choosing bandwidth, detuning, and coupling, one tailors the rotation profile to the target noise crossover. Practically, the attainable rotation and the preserved squeezing are limited by optical loss and mode mismatch, which inject uncorrelated vacuum and partially unwind the correlations the detuned cavity imprints on sidebands.

**Note:** On resonance ( $\Delta = 0$ ), the output quadratures can then be written as

$$\begin{aligned}\delta\hat{\mathbf{u}}_r[\Omega] &= \frac{\kappa_1 - \kappa/2 + i\Omega}{\kappa/2 - i\Omega} \delta\hat{\mathbf{u}}_{in}[\Omega] + \frac{\sqrt{\kappa_1\kappa_2}}{\kappa/2 - i\Omega} \delta\hat{\mathbf{u}}_{vac}[\Omega] + \frac{\sqrt{\kappa_1\kappa_0}}{\kappa/2 - i\Omega} \delta\hat{\mathbf{u}}_l[\Omega] \\ \delta\hat{\mathbf{u}}_t[\Omega] &= \frac{\sqrt{\kappa_1\kappa_2}}{\kappa/2 - i\Omega} \delta\hat{\mathbf{u}}_{in}[\Omega] + \frac{\kappa_2 - \kappa/2 + i\Omega}{\kappa/2 - i\Omega} \delta\hat{\mathbf{u}}_{vac}[\Omega] + \frac{\sqrt{\kappa_2\kappa_0}}{\kappa/2 - i\Omega} \delta\hat{\mathbf{u}}_l[\Omega]\end{aligned}\quad (I.87)$$

If we consider the reflected quadratures noise spectra we see that

$$\mathbf{S}_r[\Omega] = \frac{(\kappa_1 - \kappa/2)^2 + \Omega^2}{(\kappa/2)^2 + \Omega^2} \mathbf{S}_{in}[\Omega] + \frac{\kappa_1}{(\kappa/2)^2 + \Omega^2} (\kappa_2 \mathbf{1} + \kappa_0 \mathbf{1}) \quad (I.88)$$

where the vacuum and loss covariance matrices are equal to  $\mathbf{1}$ . As these two vacua sum up linearly, it is equivalent to consider a single vacuum with an effective decay rate  $\kappa_2 + \kappa_0 \rightarrow \kappa_2$  to lighten the notation. We then absorb intrinsic losses into the output coupler, and consider only two ports: the input coupler with decay rate  $\kappa_1$  and the output coupler with decay rate  $\kappa_2$ . We stress that this substitution is only valid when considering the **reflected** quadratures. When focusing on the transmitted quadratures, one can perform a similar redefinition with  $\kappa_1$  i.e.  $\kappa_1 + \kappa_0 \rightarrow \kappa_1$ .

**Transfer matrices and Spectra:** Expressing the reflected and transmitted quadratures in matrix form yields

$$\begin{aligned}\delta\hat{\mathbf{u}}_r[\Omega] &= \mathbf{T}_r[\Omega] \delta\hat{\mathbf{u}}_{in}[\Omega] + \mathbf{L}_r[\Omega] \delta\hat{\mathbf{u}}_{vac}[\Omega] \\ \delta\hat{\mathbf{u}}_t[\Omega] &= \mathbf{T}_t[\Omega] \delta\hat{\mathbf{u}}_{in}[\Omega] + \mathbf{L}_t[\Omega] \delta\hat{\mathbf{u}}_{vac}[\Omega]\end{aligned}\quad (I.89)$$

where the transfer matrices for the input and loss ports given by

$$\begin{aligned}\mathbf{T}_r[\Omega] &= \kappa_1 \mathbf{\Gamma} \mathbf{M}_\Delta^{-1} \mathbf{\Gamma}^{-1} - \mathbf{1}, & \mathbf{L}_r[\Omega] &= \sqrt{\kappa_1\kappa_2} \mathbf{\Gamma} \mathbf{M}_\Delta^{-1} \mathbf{\Gamma}^{-1} \\ \mathbf{T}_t[\Omega] &= \sqrt{\kappa_1\kappa_2} \mathbf{\Gamma} \mathbf{M}_\Delta^{-1} \mathbf{\Gamma}^{-1}, & \mathbf{L}_t[\Omega] &= \kappa_2 \mathbf{\Gamma} \mathbf{M}_\Delta^{-1} \mathbf{\Gamma}^{-1} - \mathbf{1}\end{aligned}$$

such that the covariance matrices for the reflected and transmitted quadratures of a detuned

cavity are given by

$$\begin{aligned}\mathbf{S}_r[\Omega] &= \mathbf{T}_r[\Omega]\mathbf{S}_{\text{in}}[\Omega]\mathbf{T}_r^\dagger[\Omega] + \mathbf{L}_r[\Omega]\mathbf{L}_r^\dagger[\Omega] \\ \mathbf{S}_t[\Omega] &= \mathbf{T}_t[\Omega]\mathbf{S}_{\text{in}}[\Omega]\mathbf{T}_t^\dagger[\Omega] + \mathbf{L}_t[\Omega]\mathbf{L}_t^\dagger[\Omega]\end{aligned}\quad (\text{I.90})$$

Additionally, we define the one-photon reflection matrix of the input field by

$$\mathbf{r}_\Delta[\Omega] = \kappa_1 \mathbf{M}_\Delta^{-1} - \mathbf{1} = \begin{pmatrix} r_\Delta[\Omega] & 0 \\ 0 & r_\Delta^*[-\Omega] \end{pmatrix} \quad \text{with} \quad r_\Delta[\Omega] = \frac{\kappa_1}{\kappa/2 - i(\Delta + \Omega)} - 1 \quad (\text{I.91})$$

such that

$$\mathbf{T}_r[\Omega] = \boldsymbol{\Gamma} \mathbf{r}_\Delta[\Omega] \boldsymbol{\Gamma}^{-1} = \frac{1}{2} \begin{pmatrix} r_\Delta[\Omega] + r_\Delta^*[-\Omega] & i(r_\Delta[\Omega] - r_\Delta^*[-\Omega]) \\ -i(r_\Delta[\Omega] - r_\Delta^*[-\Omega]) & r_\Delta[\Omega] + r_\Delta^*[-\Omega] \end{pmatrix} \quad (\text{I.92})$$

and similarly for the one photon transmission matrix

$$\mathbf{t}_\Delta[\Omega] = \sqrt{\kappa_1 \kappa_2} \mathbf{M}_\Delta^{-1} = \begin{pmatrix} t_\Delta[\Omega] & 0 \\ 0 & t_\Delta^*[-\Omega] \end{pmatrix} \quad \text{with} \quad t_\Delta[\Omega] = \frac{\sqrt{\kappa_1 \kappa_2}}{\kappa/2 - i(\Delta + \Omega)} \quad (\text{I.93})$$

such that

$$\mathbf{T}_t[\Omega] = \boldsymbol{\Gamma} \mathbf{t}_\Delta[\Omega] \boldsymbol{\Gamma}^{-1} = \frac{1}{2} \begin{pmatrix} t_\Delta[\Omega] + t_\Delta^*[-\Omega] & i(t_\Delta[\Omega] - t_\Delta^*[-\Omega]) \\ -i(t_\Delta[\Omega] - t_\Delta^*[-\Omega]) & t_\Delta[\Omega] + t_\Delta^*[-\Omega] \end{pmatrix} \quad (\text{I.94})$$

### Example 1: Mode Cleaner

Let us consider a configuration such that  $\kappa_1 = \kappa_2 \approx \kappa/2$  where we assume negligible losses  $\kappa_0 \ll \kappa_{1,2}$ . It represents a cavity where the input and output mirror transmittivities are equal, and we set the laser resonant to the cavity ( $\Delta = 0$ ), such that the transmitted quadratures are written

$$\delta \hat{\mathbf{u}}_t[\Omega] = \frac{\kappa/2}{\kappa/2 - i\Omega} \delta \hat{\mathbf{u}}_{\text{in}}[\Omega] + \frac{i\Omega}{\kappa/2 - i\Omega} \delta \hat{\mathbf{u}}_{\text{vac}}[\Omega]. \quad (\text{I.95})$$

The resulting transmitted quadrature covariance matric is given by:

$$\mathbf{S}_t[\Omega] = \frac{(\kappa/2)^2}{(\kappa/2)^2 + \Omega^2} \mathbf{S}_{\text{In}}[\Omega] + \frac{\Omega^2}{(\kappa/2)^2 + \Omega^2} \mathbf{1} \quad (\text{I.96})$$

Now consider that the input fluctuations are above those of vacuum i.e. the input field features classical noise. We would then have  $S_{pp}^{\text{in}} > S_{pp}^{\text{vac}} = 1$  and  $S_{qq}^{\text{in}} > S_{qq}^{\text{vac}} = 1$ . One can notice that the prefactor to the input noises is a Lorentzian function - a low pass filter. Hence, the noises of the input fields are low pass filtered by the cavity, while the vacuum

fluctuations are high pass filtered at precisely the same cutoff  $\kappa/2$ . The mean field of the *bright* coherent input is fully transmitted, but its super-vacuum fluctuations, potentially classically modulated, are filtered by the cavity. Taking a high finesse cavity such that the cutoff frequency is low, the transmitted field now features vacuum sidebands: it has been *clean* from classical noise. This is the principle of a *mode cleaner* cavity, which is used in many precision experiments to provide a spectrally pure laser field, as well as a spatially filtered beam such that the transmitted beam is a pure TEM<sub>00</sub>.

### Example 2: Detuned single port cavity

We now consider a lossless single port cavity with  $\kappa_2 = 0$  and  $\kappa_1 = \kappa$ . The transfer matrix is expressed as

$$\mathbf{T}_r[\Omega] = \frac{1}{(\kappa/2 - i\Omega)^2 + \Delta^2} \begin{pmatrix} (\kappa/2)^2 - \Delta^2 + \Omega^2 & -\kappa\Delta \\ +\kappa\Delta & (\kappa/2)^2 - \Delta^2 + \Omega^2 \end{pmatrix} \quad (I.97)$$

$$\kappa \mathbf{\Gamma} \mathbf{M}_\Delta^{-1} \mathbf{\Gamma}^{-1} - \mathbf{1} = \frac{1}{(\kappa/2 - i\Omega)^2 + \Delta^2} \begin{pmatrix} (\kappa/2)^2 - \Delta^2 + \Omega^2 & -\kappa\Delta \\ +\kappa\Delta & (\kappa/2)^2 - \Delta^2 + \Omega^2 \end{pmatrix}$$

such that the covariance matrix is given by

$$\mathbf{S}_r[\Omega] = \begin{pmatrix} S_{pp}^r[\Omega] & S_{pq}^r[\Omega] \\ S_{qp}^r[\Omega] & S_{qq}^r[\Omega] \end{pmatrix} \quad (I.98)$$

where we won't write the full expressions of the matrix elements for brevity. The key point is that the off-diagonal terms are non zero, meaning that the reflected quadratures are correlated. This is the frequency-dependent rotation mechanism described above.

This configuration is used in our experiment to measure the squeezing spectrum of the OPO, as the

#### I.2.5 Non Linear Cavities

We now turn to the description of optical cavities in which a  $\chi^{(2)}$  medium is embedded within. This non linear medium can be used both for sum frequency generation, or difference frequency generation. The generic Hamiltonian describing a degenerate  $\chi^{(2)}$  parametric process is

$$H = \hbar\omega_p \hat{b}^\dagger \hat{b} + \hbar\omega_0 \hat{a}^\dagger \hat{a} + \frac{i\hbar\epsilon}{2} (\hat{b} \hat{a}^{\dagger 2} - \hat{b}^\dagger \hat{a}^2) \quad (I.99)$$

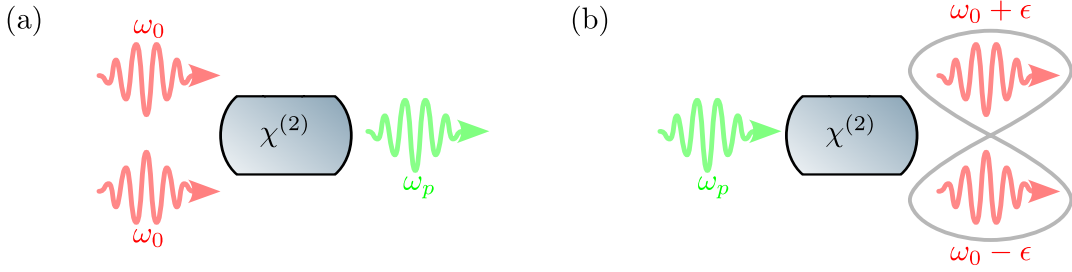


Fig. I.5 Yes

where we assumed perfect phase matching for simplicity, that is  $\epsilon \in \mathbb{R}$ . In our experiment with squeezed light, we do use both as to first generate a pump field using a Second Harmonic Generation (SHG) scheme, then use the generated field to *pump* a degenerate Optical Parametric Oscillator (OPO). The equations of motion of both fields are very similar in their structure, yet different in their phenomenology. Here we outline the main results and predictions for both.

### Second Harmonic Generation

The SHG scheme consists in shining a laser field at frequency  $\omega_0$  onto the cavity, and the nonlinear medium generates a field at frequency  $\omega_p = 2\omega_0$ , that is, two photons at  $\omega_0$  described by operator  $\hat{a}$ , are converted into a single photon at  $\omega_p$  described by operator  $\hat{b}$ . The input field is thus  $\hat{a}_{\text{in}}$  at  $\omega_0$ , while the input fields at  $\omega_p$  are vacua  $\hat{b}_{\text{in}} = \delta b_l = \delta \hat{b}_{\text{vac}}$ . We restrain the theoretical description to our experiment, where the end mirror reflectivity is  $\sim 1$  for our generated green beam, as seen in the figure below  $\kappa_{2,b} = 0$ . We will not derive the noise spectra for this scheme as they are not of interest in this work, displaying standard vacuum type fluctuations in both the pump and second harmonic field.

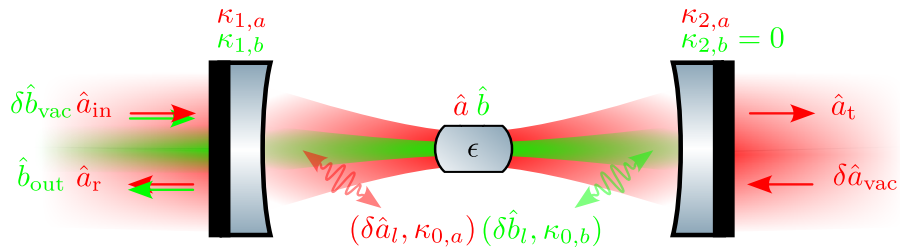


Fig. I.6 Yes

We rather focus on the mean field solution. The scalar part of the QLE on resonance for

both fields are given by

$$\begin{aligned} 0 &= -\frac{\kappa_a}{2} \bar{\alpha} + \epsilon \bar{\alpha}^* \bar{\beta} + \sqrt{\kappa_{1,a}} \bar{\alpha}_{\text{in}}, \\ 0 &= -\frac{\kappa_b}{2} \bar{\beta} + \frac{\epsilon}{2} \bar{\alpha}^2. \end{aligned} \quad (\text{I.100})$$

where subscript  $a$  and  $b$  refer to the  $\omega_0$  and  $\omega_p$  fields respectively. Solving for the  $\bar{\beta}$  field and computing the output field  $\bar{\beta}_{\text{out}}$  from the input mirror using the input-output relations, yields an output intensity of

$$\begin{aligned} |\bar{\beta}_{\text{out}}|^2 &= \frac{\kappa_a^2 \kappa_{1,b}^2}{4 \varepsilon^2} \left[ \left( 1 + \frac{108 \varepsilon^2 \kappa_{1,a}}{\kappa_a^3 \kappa_b} |\bar{\alpha}_{\text{in}}|^2 \left( 1 + \sqrt{1 + \frac{\kappa_a^3 \kappa_b}{54 \varepsilon^2 \kappa_{1,a} |\bar{\alpha}_{\text{in}}|^2}} \right) \right)^{1/6} \right. \\ &\quad \left. - \left( 1 + \frac{108 \varepsilon^2 \kappa_{1,a}}{\kappa_a^3 \kappa_b} |\bar{\alpha}_{\text{in}}|^2 \left( 1 + \sqrt{1 + \frac{\kappa_a^3 \kappa_b}{54 \varepsilon^2 \kappa_{1,a} |\bar{\alpha}_{\text{in}}|^2}} \right) \right)^{-1/6} \right]^4. \end{aligned} \quad (\text{I.101})$$

This cumbersome expression can be simplified in two limits. In the low input power limit, the output power scales quadratically with the input power, whereas at high powers it scales as  $|\alpha_{\text{in}}|^{4/3}$ .

**Pseudo linear behaviour:** For intermediate powers, the output power scales almost linearly with the input power, which is precisely the regime in which we will operate. The crossover between these regimes is set by the non linear gain  $\epsilon$  and the cavity decay rates  $\kappa_{a,b}$ .

### Optical Parametric Oscillation & Amplification

For this scheme, we consider a pump field with frequency  $\omega_p = 2\omega_0$ . A first key difference from the SHG scheme can be highlighted by the fact that we are now pumping at  $2\omega_0$ , such that pairs of entangled photons are generated at  $\omega_0 + \epsilon$  and  $\omega_0 - \epsilon$ , with  $\epsilon$  a sideband frequency allowed by the cavity bandwidth, hence conserving energy.

We further consider the pump is not *depleted*, such that we can change  $\hat{b}$  to its mean field value  $|\bar{\beta}|e^{i\bar{\varphi}_b}$ , and we disregard the  $\hat{b}$  fluctuations in the equations of motion for simplicity. A careful and complete derivations could also be carried out by keeping all terms in the equations of motion, but it is not serving our purpose here so we will these assumptions to lighten the notation. The total non linear gain is defined as  $g = \epsilon |\bar{\beta}|$ , and the QLEs for the

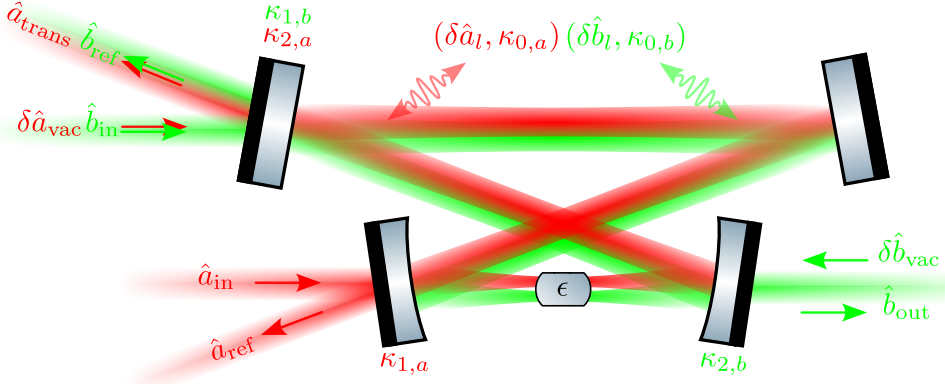


Fig. I.7 Yes

steady state and fluctuation parts of the  $\hat{a}$  field yields:

$$\begin{cases} 0 = -\left(\frac{\kappa}{2} - i\Delta\right)\bar{\alpha} + ge^{i\bar{\varphi}_b}\bar{\alpha}^* + \sqrt{\kappa_1}\bar{\alpha}_{in} \\ \dot{\delta\hat{a}}(t) = -\begin{pmatrix} \kappa/2 - i\Delta & -ge^{i\bar{\varphi}_b} \\ -ge^{-i\bar{\varphi}_b} & \kappa/2 + i\Delta \end{pmatrix}\delta\hat{a}(t) + \sqrt{\kappa_1}\delta\hat{a}_{in}(t) + \sqrt{\kappa_2}\delta\hat{a}_{vac}(t) \end{cases} \quad (\text{I.102})$$

**Mean field solution (Static case):** Assuming a real input field  $\bar{\alpha}_{in} = |\bar{\alpha}_{in}|$ , the transmitted field is given by:

$$\bar{\alpha}_t = \frac{\sqrt{\kappa_1\kappa_2}}{\kappa/2} \frac{1 + i\frac{\Delta}{\kappa/2} + xe^{i\bar{\varphi}_b}}{1 + \left(\frac{\Delta}{\kappa/2}\right)^2 - |x|^2} |\bar{\alpha}_{in}| \quad (\text{I.103})$$

where we define the normalised pump parameter  $x = 2g/\kappa \in \mathbb{R}$ . This normalised pump parameter also equals the ratio of the pump field amplitude by the pump field threshold often written  $B/B_{\text{thr}}$ . For a resonant cavity, the expression reduces to the well known parametric amplification/deamplification scheme

$$\bar{\alpha}_t = \frac{\sqrt{\kappa_1\kappa_2}}{\kappa/2} \frac{1 + xe^{i\bar{\varphi}_b}}{1 - |x|^2} |\bar{\alpha}_{in}| \quad (\text{I.104})$$

in which the amplification or deamplification processes are set by the phase of the pump  $\bar{\varphi}_b$ . In the absence of a non linear medium  $x = 0$  we recover the standard cavity results shown above. The threshold is defined at  $x = 1$ , where the rate of generation of entangled pairs exceeds the rate at which they leak from the cavity. In other words,  $x$  is unity when the round trip gain equals the round trip losses. That's precisely the point where the no depletion approximation breaks down, as illustrated by the divergence seen in transmitted field at this very value (how could one obtain a diverging field from a pump field with a

finite number of photons). We also notice two special cases, when  $\bar{\varphi}_b = \{0, \pi\}$ , coinciding with the amplification and the deamplification processes respectively.

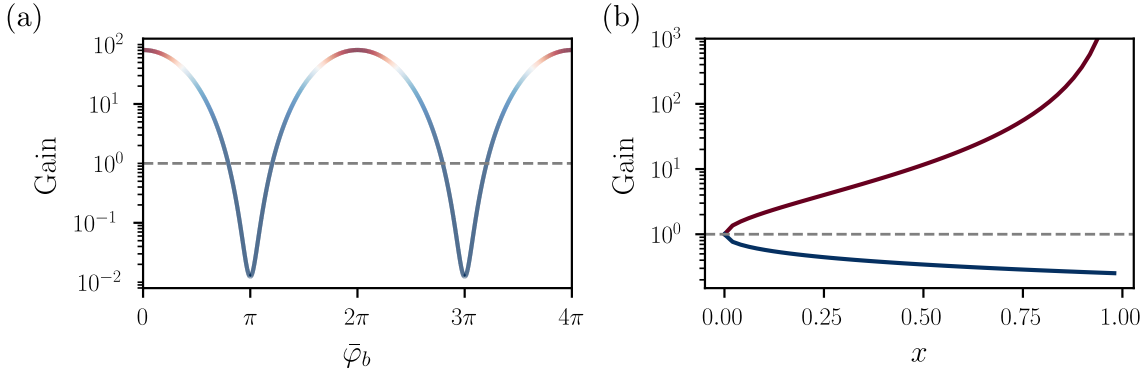


Fig. I.8 Yes

**Fluctuations solution:** The general expression of the QLE in Fourier space is given by

$$\tilde{\mathbf{M}}_\Delta \delta \hat{\mathbf{a}}[\Omega] = \sqrt{\kappa_1} \delta \hat{\mathbf{a}}_{\text{in}}[\Omega] + \sqrt{\kappa_2} \delta \hat{\mathbf{a}}_{\text{vac}}[\Omega] \quad (\text{I.105})$$

with

$$\tilde{\mathbf{M}}_\Delta = \begin{pmatrix} \kappa/2 - i(\Delta + \Omega) & -ge^{i\bar{\varphi}_b} \\ -ge^{-i\bar{\varphi}_b} & \kappa/2 + i(\Delta - \Omega) \end{pmatrix}$$

where we defined  $\tilde{\mathbf{M}}_\Delta$  to not be confused with the matrix  $\mathbf{M}_\Delta$  defined earlier for a simple cavity. Note that a genuine *frequency dependent* squeezing angle could be obtained by detuning the OPO cavity, but the frequency range over which the squeezing angle varies is limited by the cavity bandwidth, which is typically small compared to the frequency range of interest in our experiment. This phenomenon was realised experimentally few years ago [?], but is not the focus of our work.

In the context of our work, we will assume :

- the pump phase is locked to  $\bar{\varphi}_b = \{0, \pi\}$  i.e. amplification or deamplification regime,
- the cavity is resonant  $\Delta = 0$ ,

We further normalise all frequencies to the cavity bandwidth  $\kappa/2$  such that  $\Omega \rightarrow \Omega/(\kappa/2)$  and  $g \rightarrow g/(\kappa/2) = x$ , such that the off diagonal terms below can simply be written  $\mp x$  factoring out the cavity bandwidth. We carry out the derivation for  $\bar{\varphi}_b = 0$  (amplification) for simplicity, and the  $\bar{\varphi}_b = \pi$  (deamplification) case is obtained by changing  $x$  to  $-x$  in the

final expressions. The matrix QLE in Fourier space is written as

$$\tilde{\mathbf{M}}_0 \delta \hat{\mathbf{a}}[\Omega] = \sqrt{\kappa_1} \delta \hat{\mathbf{a}}_{\text{in}}[\Omega] + \sqrt{\kappa_2} \delta \hat{\mathbf{a}}_{\text{vac}}[\Omega] \quad (\text{I.106})$$

with

$$\tilde{\mathbf{M}}_0 = \frac{\kappa}{2} \begin{pmatrix} 1 - i \frac{\Omega}{\kappa/2} & -x \\ -x & 1 - i \frac{\Omega}{\kappa/2} \end{pmatrix}$$

**Transfer matrices and Spectra:** As before with a simple cavity, the transmitted quadratures at resonance are then

$$\delta \hat{\mathbf{u}}_{\text{OPO}}[\Omega] = \mathbf{T}_{\text{OPO}}[\Omega] \delta \hat{\mathbf{u}}_{\text{in}}[\Omega] + \mathbf{L}_{\text{OPO}}[\Omega] \delta \hat{\mathbf{u}}_{\text{vac}}[\Omega] \quad (\text{I.107})$$

where we defined the transfer matrices for the input and loss ports as

$$\mathbf{T}_{\text{OPO}}[\Omega] = \sqrt{\kappa_1 \kappa_2} \boldsymbol{\Gamma} \tilde{\mathbf{M}}_0^{-1} \boldsymbol{\Gamma}^{-1}, \quad \mathbf{L}_{\text{OPO}}[\Omega] = \kappa_2 \boldsymbol{\Gamma} \tilde{\mathbf{M}}_0^{-1} \boldsymbol{\Gamma}^{-1} - \mathbf{1} \dots$$

After a bit of algebra, the covariance matrix of the transmitted field at  $\bar{\varphi}_b = 0$  is then computed as

$$\mathbf{S}_{\text{OPO}}^0[\Omega] = \begin{pmatrix} 1 + \frac{\kappa_2}{\kappa} \frac{4x}{(1-x)^2 + \left(\frac{\Omega}{\kappa/2}\right)^2} & 0 \\ 0 & 1 - \frac{\kappa_2}{\kappa} \frac{4x}{(1+x)^2 + \left(\frac{\Omega}{\kappa/2}\right)^2} \end{pmatrix} \quad (\text{I.108})$$

On a side note, when deriving the noise spectra for the intracavity field, the maximum amount of squeezing is limited to 3dB, while the transmitted field can feature arbitrarily high squeezing levels. This is interpreted as additional correlations between vacuum fluctuations being reflected at the output port of the OPO and the squeezed field leaking from this very same output port, allowing for strong squeezing.

**The perfect squeezer:** Starting from (I.108), in the idealized limit of perfect escape efficiency ( $\eta_{\text{esc}} = 1$ ) and for analysis frequencies much smaller than the cavity bandwidth ( $\Omega/\kappa \rightarrow 0$ ), the expression simplifies to

$$\mathbf{S}_{\text{OPO}}^0[\Omega] = \begin{pmatrix} \frac{(1+x)^2}{(1-x)^2} & 0 \\ 0 & \frac{(1-x)^2}{(1+x)^2} \end{pmatrix} \quad (\text{I.109})$$

Introducing the standard squeezing parameter  $r$  through the relation  $x = \tanh \frac{r}{2}$ , one can rewrite the numerator and denominator as

$$1 + \tanh \frac{r}{2} = \frac{e^{+\frac{r}{2}}}{\cosh \frac{r}{2}}, \quad 1 - \tanh \frac{r}{2} = \frac{e^{-\frac{r}{2}}}{\cosh \frac{r}{2}},$$

such that

$$\frac{(1 \pm \tanh \frac{r}{2})^2}{(1 \mp \tanh \frac{r}{2})^2} = \left( \frac{e^{\pm \frac{r}{2}}}{e^{\mp \frac{r}{2}}} \right)^2 = e^{\pm 2r}.$$

Thus when  $\bar{\varphi}_b = \{0, \pi\}$ , in the lossless, low-frequency limit the transmitted noise levels reduce to the well-known parametric result

$$\mathbf{S}_{\text{OPO}}^0[\Omega] = \begin{pmatrix} e^{+2r} & 0 \\ 0 & e^{-2r} \end{pmatrix} \quad \text{and} \quad \mathbf{S}_{\text{OPO}}^\pi[\Omega] = \begin{pmatrix} e^{-2r} & 0 \\ 0 & e^{+2r} \end{pmatrix} \quad (\text{I.110})$$

where we can now establish that an amplified field ( $\bar{\varphi}_b = 0$ ) corresponds to a squeezed phase quadrature and an anti-squeezed amplitude quadrature, while a deamplified field ( $\bar{\varphi}_b = \pi$ ) corresponds to a squeezed amplitude quadrature and an anti-squeezed phase quadrature. Later on, we will use this idealized expression to describe how squeezed light interacts with a mechanical resonator whose frequency is much smaller than the OPO bandwidth.

**Losses:** Squeezing is very sensitive to optical losses, which couple uncorrelated vacuum fluctuations into the squeezed field and degrade the squeezing level. The escape efficiency  $\eta_{\text{esc}} = \kappa_2/\kappa$  of the OPO cavity is one such loss mechanism, but there are many others in a real experiment: propagation losses, mode-mismatch, non-unity quantum efficiency of the photodetectors, etc. One can then distinguish between *intracavity* losses, which are accounted for in the escape efficiency, and *extracavity* losses, which we denote by  $\eta_{\text{ext}}$  and lump all other loss mechanisms into a single effective loss. The effect of these losses can be modeled as a beam-splitter mixing the squeezed field with vacuum fluctuations, such that the lossy covariance matrix is given by

$$\mathbf{S}_{\text{det}}[\Omega] = (1 - \eta) \mathbf{S}_{\text{OPO}}^{\bar{\varphi}_b}[\Omega] + \eta \mathbf{1} \quad (\text{I.111})$$

This expression is actually true for any Gaussian state suffering from losses.

**Frequency dependence:** Similarly to what was seen earlier considering general quantum states, squeezing at an arbitrary angle  $\theta$  can be obtained by rotating the covariance matrix. However, one can now make the squeezing angle frequency dependent above as

$$\mathbf{S}_{\text{OPO}}^\theta[\Omega] = \mathbf{R}(\theta[\Omega]) \mathbf{S}_{\text{OPO}}^0[\Omega] \mathbf{R}^\dagger(\theta[\Omega]). \quad (\text{I.112})$$

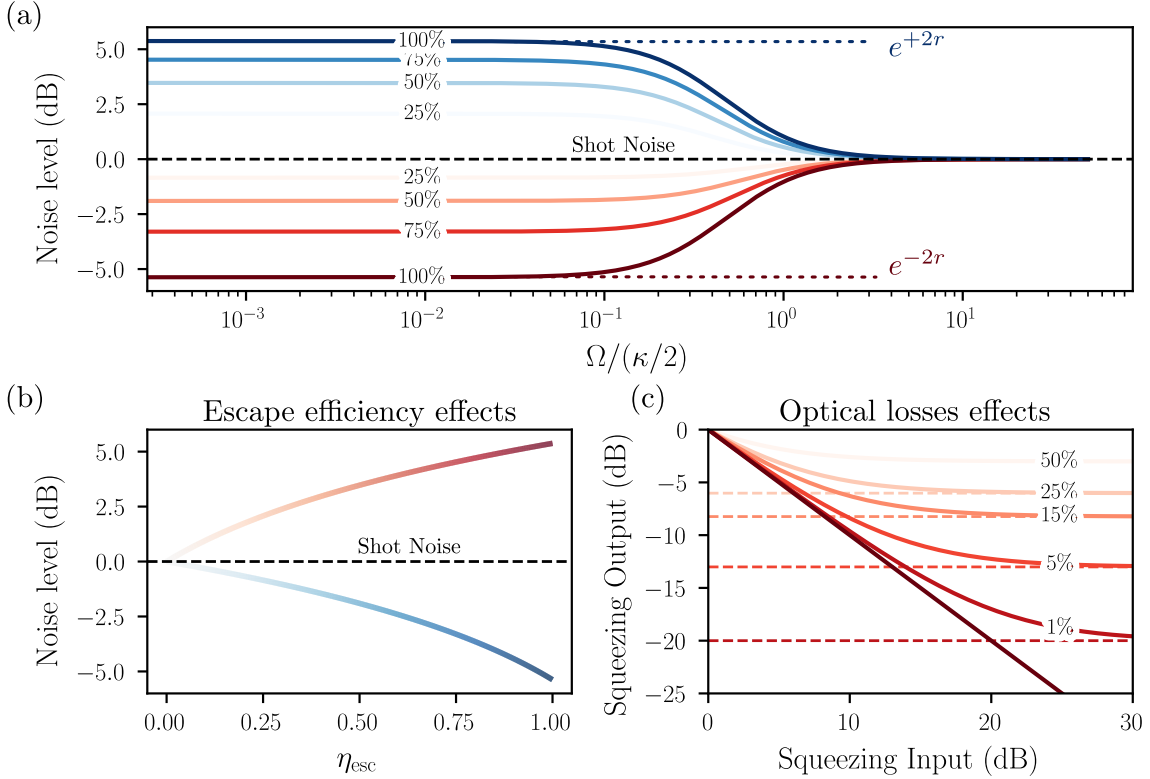


Fig. I.9 Yes

where  $\theta[\cdot]$  The  $\mathbf{S}[\Omega]$  can either be the full cavity one, or the idealized one. As already mentionned, the mechanical frequencies of interest will be deep in the OPO bandwidth such that we will use the ideal squeezer expression (I.110) in addition with extrinsic losses (I.111). The explicit of the covariance matrix at a frequency dependent angle is then

$$\mathbf{S}_{\text{OPO}}^{\theta}[\Omega] = \begin{pmatrix} \cosh 2r - \sinh 2r \cos 2\theta[\Omega] & -\sinh 2r \sin 2\theta[\Omega] \\ -\sinh 2r \sin 2\theta[\Omega] & \cosh 2r + \sinh 2r \cos 2\theta[\Omega] \end{pmatrix} \quad (\text{I.113})$$

### I.2.6 Optomechanical Cavities

We now turn to standard optomechanical cavities. As in the simple FP case, we consider a cavity mode, in which we now allow one of the the coupler (traditionnaly the output coupler), to be itself a *mechanical* harmonic oscillator with annihilation operator  $\hat{c}$ , effective mass  $m$ , angular frequency  $\Omega_m$  and damping rate  $\Gamma_m$ . In canonical optomechanical systems the mechanics operators are usually denoted as  $\hat{b}$  but in our case it would be redundant with the operators describing the pump field in non linear systems. The position can be expressed in terms of our bosonic operators as  $\hat{x} = x_0(\hat{c} + \hat{c}^\dagger)$  with  $x_0 = \sqrt{\hbar/(2m\Omega_m)}$  the resonator's zero point fluctuations.

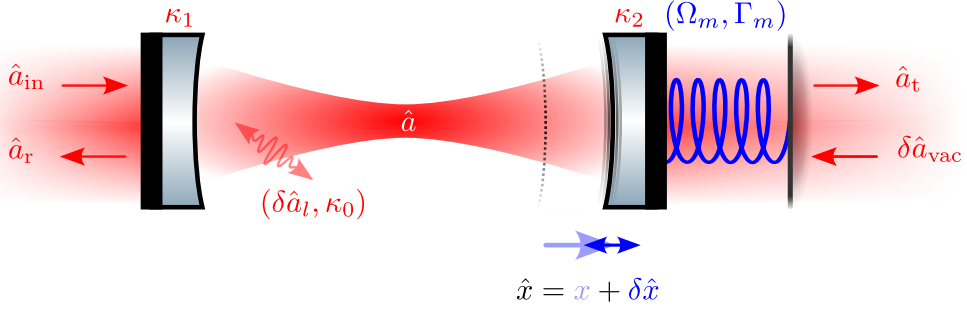


Fig. I.10 Yes

### Mechanics & Radiation Pressure Force

The equation of motion of such an oscillator are given by

$$m \ddot{x} = -m \Omega_m^2 \hat{x} - m \Gamma_m \dot{\hat{x}} + \hat{F} \quad (\text{I.114})$$

where  $\hat{F}$  is the total force acting on the oscillator. In Fourier space, we recover the standard linear response form

$$\hat{x}[\Omega] = \chi[\Omega] \hat{F}[\Omega] \quad \text{with} \quad \chi[\Omega] = \frac{1}{m(\Omega_m^2 - \Omega^2 - i\Gamma_m \Omega)} \quad (\text{I.115})$$

where  $\chi[\Omega]$  is the susceptibility linearly relating the position  $\hat{x}[\Omega]$  to the external force  $\hat{F}[\Omega]$ . This susceptibility can also be written as

$$\chi[\Omega] = |\chi[\Omega]| e^{i\phi_m[\Omega]} \quad (\text{I.116})$$

with

$$\text{with } \phi_m[\Omega] = \arctan \left( \frac{\Gamma_m \Omega}{\Omega_m^2 - \Omega^2} \right) \quad \text{and} \quad |\chi[\Omega]| = \frac{1}{m \sqrt{(\Omega_m^2 - \Omega^2)^2 + (\Gamma_m \Omega)^2}}.$$

Similarly to the simple Fabry-Perot cavity (being a driven damped harmonic oscillator too), we can define the analog of the Finesse, namely the quality factor, defined as

$$Q = \frac{\Omega_m}{\Gamma_m} \quad (\text{I.117})$$

which is the number of oscillations before the resonator's energy is damped by a factor  $1/e$ . On resonance, the susceptibility is purely imaginary and reads  $\chi[\Omega_m] = -iQ/(m\Omega_m^2)$ .

As before, the position is also linearized considering small quantum fluctuations compared to its mean value, such that we write  $\hat{x} = x + \delta\hat{x}$ . Importantly, the total position fluctuation  $\delta\hat{x} = \sum \delta\hat{x}_i$  is the sum of individual fluctuations that can arise from various sources, such as a

the zero point fluctuations, thermal fluctuations or radiation pressure induced fluctuations. In the following we will only consider a radiation pressure induced fluctuations  $\delta\hat{x}_{\text{RPN}}$ , such that  $\delta\hat{x} = \delta\hat{x}_{\text{RPN}}$ .

Due to the continuous yet discrete photon *hits* at a rate exceeding the resonator frequency, the resonator *feels* an effective force. This radiation pressure force is expressed as

$$\hat{F} = 2\frac{\hbar k_L}{\tau_c} \hat{a}^\dagger \hat{a} = 2\frac{\hbar k_L}{\tau_c} |\bar{\alpha}|^2 + 2\frac{\hbar k_L}{\tau_c} |\bar{\alpha}| \delta\hat{p} + \mathcal{O}(\delta\hat{a}^\dagger \delta\hat{a}) \quad (\text{I.118})$$

where  $k_L = 2\pi/\lambda$  is the laser wavevector, and  $\tau_c = 2L/c$  is the cavity round-trip time, and we neglect second order terms. This force then features a static component shifting the resonator away from its equilibrium position, that be the  $x$  component, as well as a fluctuating component  $\delta\hat{F} \propto \delta\hat{p}$  jittering the resonator around its mean displacement, that's  $\delta\hat{x}_{\text{RPN}}$ . The position mean value and its fluctuations under radiation pressure can therefore be expressed to first order as

$$x = \frac{2\hbar k_L |\bar{\alpha}|^2}{\tau_c} \chi[0], \quad \delta\hat{x}_{\text{RPN}}[\Omega] = \frac{2\hbar k_L |\bar{\alpha}|}{\tau_c} \chi[\Omega] \delta\hat{p}[\Omega]. \quad (\text{I.119})$$

### Optomechanical QLE

Considering an optomechanical cavity of length  $L$  at rest, such that the mean resonator position is initialy 0, the bare cavity free spectral range is given by  $\omega_{\text{FSR}} = \pi c/L$  and the cavity frequency  $\omega_c = N\omega_{\text{FSR}}$ . Injecting light inside this cavity then shifts the mechanical resonator position as seen above, which in turn changes the cavity length  $L \rightarrow L+x$ , thus its frequency. Writing the Hamiltonian, we simply Taylor expand to first order in  $\hat{x}$  the cavity frequency  $\omega_c(\hat{x}) = \omega_c + \hat{x} \partial\omega_c/\partial x$  such that we have:

$$\hat{H} = -\hbar\Delta\hat{a}^\dagger \hat{a} + \hbar G\hat{x} \hat{a}^\dagger \hat{a} + \hbar\Omega_m \hat{c}^\dagger \hat{c} \quad (\text{I.120})$$

where  $G = \partial\omega_c/\partial x = -\omega_c/L$ . One can also identify a useful identity by considering the radiation pressure force (I.118) and the Hamiltonian above, such that

$$\hat{F}_{\text{rad}} = -\frac{\partial\hat{H}}{\partial\hat{x}} = -\hbar G\hat{a}^\dagger \hat{a} \quad \Rightarrow \quad G = -2\frac{k_L}{\tau_c} \quad (\text{I.121})$$

consistent with our previous expression of  $G$  such that we rewrite the position fluctuation as  $\delta\hat{x}_{\text{tot}}[\Omega] = -\hbar G|\bar{\alpha}|\chi[\Omega] \delta\hat{p}[\Omega]$ . Plugging in the QLE and ignoring vacuum and loss fluctu-

ations for notational simplicity, the field's equation are written as

$$\begin{cases} 0 = -\left(\frac{\kappa}{2} - i\bar{\Delta}\right)\bar{\alpha} + \sqrt{\kappa_1} |\bar{\alpha}_{\text{in}}| \\ \delta\dot{\hat{\mathbf{a}}}(t) = -\begin{pmatrix} \kappa/2 - i\bar{\Delta} & 0 \\ 0 & \kappa/2 + i\bar{\Delta} \end{pmatrix} \delta\hat{\mathbf{a}}(t) + iG\bar{\alpha}\delta\hat{x} \begin{pmatrix} +1 \\ -1 \end{pmatrix} + \sqrt{\kappa_1} \delta\hat{\mathbf{a}}_{\text{in}}(t) + \sqrt{\kappa_2} \delta\hat{\mathbf{a}}_{\text{vac}}(t) \end{cases} \quad (\text{I.122})$$

where we introduced the radiation pressure induced detuning  $\bar{\Delta} = \Delta - Gx$  - that is, the mean resonator displacement shifts the cavity frequency, hence the detuning - and where we assume the input field to be real.

This so called *dispersive* coupling, where the cavity frequency  $\omega_c(x)$  depends linearly on the resonator's position to first order, is the hallmark of the optomechanical interaction. In the canonical model, the cavity linewidth  $\kappa$  do not depend on the resonator's position.

**Mean field solution & Bistability:** Writing the mean intracavity amplitude by keeping the *unperturbed* detuning  $\Delta$  for clarity and substituting for the static displacement  $x$ , we get

$$\bar{\alpha} = \frac{\sqrt{\kappa_1}}{\kappa/2 - i\left(\Delta - \frac{\hbar G^2 |\bar{\alpha}|^2}{m_{\text{eff}} \Omega_m^2}\right)} |\bar{\alpha}_{\text{in}}| \quad (\text{I.123})$$

where the  $|\bar{\alpha}|^2$  dependence in disguise in the mean mechanical displacement is the root of the bistable behaviour of optomechanical cavities. We show the induced hysteresis in figure ...

For moderate injected powers, this is the standard intracavity field formula where we simply relabel  $\Delta - Gx \rightarrow \Delta$  to lighten the notation. When resonant, the intracavity field does not pick up any phase and is real i.e.  $\bar{\alpha} = |\bar{\alpha}| = 2\sqrt{\kappa_1}/\kappa |\bar{\alpha}_{\text{in}}|$ .

Optomechanical cavities do display optical ringdowns too, as detailed in the cavity sub-part above, but this is a purely optical phenomenon: the mechanics plays no role in the optical ringdown (to first order?).

**Fluctuations solution:** As previously, going to Fourier space now yields

$$\mathbf{M}_{\bar{\Delta}} \delta\hat{\mathbf{a}}[\Omega] = iG\bar{\alpha}\delta\hat{x}[\Omega] \begin{pmatrix} +1 \\ -1 \end{pmatrix} + \sqrt{\kappa_1} \delta\hat{\mathbf{a}}_{\text{in}}[\Omega] + \sqrt{\kappa_2} \delta\hat{\mathbf{a}}_{\text{vac}}[\Omega] \quad (\text{I.124})$$

where we injected the mean field solution (??) in our equations assuming moderate input power to ignore bistable behaviour. We focus on the resonant case to derive our noise spectra,

such that  $\mathbf{M}_0 = (\kappa/2 - i\Omega)\mathbf{I}$  and the intracavity quadratures are

$$\delta\hat{\mathbf{u}}[\Omega] = \frac{2G|\bar{\alpha}|}{\kappa/2 - i\Omega} \delta\hat{x}[\Omega] \begin{pmatrix} 0 \\ 1 \end{pmatrix} + \frac{\sqrt{\kappa_1}}{\kappa/2 - i\Omega} \delta\hat{\mathbf{u}}_{\text{in}}[\Omega] + \frac{\sqrt{\kappa_2}}{\kappa/2 - i\Omega} \delta\hat{\mathbf{u}}_{\text{vac}}[\Omega] \quad (\text{I.125})$$

Writing explicitly our amplitude-phase quadratures then gives

$$\begin{aligned} \delta\hat{p}[\Omega] &= \frac{\sqrt{\kappa_1}}{\kappa/2 - i\Omega} \delta\hat{p}_{\text{in}}[\Omega] + \frac{\sqrt{\kappa_2}}{\kappa/2 - i\Omega} \delta\hat{p}_{\text{vac}}[\Omega] \\ \delta\hat{q}[\Omega] &= \frac{2G|\bar{\alpha}|}{\kappa/2 - i\Omega} \delta\hat{x}[\Omega] + \frac{\sqrt{\kappa_1}}{\kappa/2 - i\Omega} \delta\hat{q}_{\text{in}}[\Omega] + \frac{\sqrt{\kappa_2}}{\kappa/2 - i\Omega} \delta\hat{q}_{\text{vac}}[\Omega] \end{aligned} \quad (\text{I.126})$$

This expression highlights the fact that only the phase is affected by the resonator position fluctuations. Physically, this can be understood by considering first that a fluctuating field amplitude leads to a fluctuating radiation pressure force, which in turn *shakes* the mechanical resonator, which changes the phase of the field reflected. The reciprocal process does not happen: a fluctuating phase does not lead to a fluctuating radiation pressure force, hence the output amplitude fluctuations are unaffected by the mechanics. Importantly, considering the field reflected off the cavity we define the displacement to phase fluctuation transduction as

$$\frac{\delta\hat{q}_x[\Omega]}{\delta\hat{x}[\Omega]} = \frac{2\sqrt{\kappa_1}G|\bar{\alpha}|}{\kappa/2 - i\Omega} = \frac{\kappa_1}{\kappa} \frac{16\mathcal{F}\sqrt{\bar{I}_{\text{in}}}}{\lambda(1 - i2\Omega/\kappa)} \quad (\text{I.127})$$

where we plugged in useful experimental parameters  $\mathcal{F}$ ,  $\lambda$  and  $\bar{I}_{\text{in}}$ . The prefactor  $\kappa_1/\kappa$  is the analog of the escape efficiency for optomechanical cavities, and is unity for single port cavities. We stress that the total phase fluctuations are the sum of various contributions, including the input phase fluctuations, the vacuum fluctuations entering from the loss port, and the position induced phase fluctuations, whether they arise from radiation pressure or other sources. This transduction factor will be used later to express the displacement sensitivity/spectra in terms of experimental parameters.

Plugging in the position fluctuations derived earlier ((I.119) and (I.118)) in the intracavity phase fluctuations we get

$$\begin{aligned} \delta\hat{q}[\Omega] &= \frac{\kappa_1}{\kappa^2} \frac{8\hbar G^2 |\bar{\alpha}_{\text{in}}|^2}{(\kappa/2 - i\Omega)^2} \chi[\Omega] \left( \sqrt{\kappa_1} \delta\hat{p}_{\text{in}}[\Omega] + \sqrt{\kappa_2} \delta\hat{p}_{\text{vac}}[\Omega] \right) \\ &\quad + \frac{1}{\kappa/2 - i\Omega} \left( \sqrt{\kappa_1} \delta\hat{q}_{\text{in}}[\Omega] + \sqrt{\kappa_2} \delta\hat{q}_{\text{vac}}[\Omega] \right) \end{aligned} \quad (\text{I.128})$$

such that we can readily express the intracavity quadratures in matrix form as

$$\delta\hat{\mathbf{u}}[\Omega] = \begin{pmatrix} 1 & 0 \\ \frac{\kappa/2 - i\Omega}{\mathcal{K}[\Omega]} & \frac{1}{\kappa/2 - i\Omega} \end{pmatrix} \left( \sqrt{\kappa_1} \delta\hat{\mathbf{u}}_{\text{in}}[\Omega] + \sqrt{\kappa_2} \delta\hat{\mathbf{u}}_{\text{vac}}[\Omega] \right). \quad (\text{I.129})$$

with

$$\mathcal{K}[\Omega] = \left( \frac{\kappa_1}{\kappa} \right)^2 \frac{8\hbar G^2 |\bar{\alpha}_{\text{in}}|^2}{(\kappa/2 - i\Omega)^2} \chi[\Omega] = \left( \frac{\kappa_1}{\kappa} \right)^2 \frac{128\hbar \mathcal{F}^2 \bar{I}_{\text{in}}}{\lambda^2 (1 - i2\Omega/\kappa)^2} \chi[\Omega]$$

We then obtain the reflected and transmitted quadrature fluctuations

$$\begin{aligned} \delta\hat{\mathbf{u}}_{\text{r}}[\Omega] &= \mathbf{T}_{\text{r}}[\Omega] \delta\hat{\mathbf{u}}_{\text{in}}[\Omega] + \mathbf{L}_{\text{r}}[\Omega] \delta\hat{\mathbf{u}}_{\text{vac}}[\Omega] \\ \delta\hat{\mathbf{u}}_{\text{t}}[\Omega] &= \mathbf{T}_{\text{t}}[\Omega] \delta\hat{\mathbf{u}}_{\text{in}}[\Omega] + \mathbf{L}_{\text{t}}[\Omega] \delta\hat{\mathbf{u}}_{\text{vac}}[\Omega]. \end{aligned} \quad (\text{I.130})$$

where we defined the transfer matrices

$$\begin{aligned} \mathbf{T}_{\text{r}}[\Omega] &= \begin{pmatrix} \frac{\kappa_1}{\kappa/2 - i\Omega} - 1 & 0 \\ \frac{\kappa_1}{\kappa/2 - i\Omega} & \frac{\kappa_1}{\kappa/2 - i\Omega} - 1 \end{pmatrix} & \mathbf{L}_{\text{r}}[\Omega] &= \begin{pmatrix} \frac{\sqrt{\kappa_1 \kappa_2}}{\kappa/2 - i\Omega} & 0 \\ \sqrt{\frac{\kappa_2}{\kappa_1}} \mathcal{K}[\Omega] & \frac{\sqrt{\kappa_1 \kappa_2}}{\kappa/2 - i\Omega} \end{pmatrix} \\ \mathbf{T}_{\text{t}}[\Omega] &= \begin{pmatrix} \frac{\sqrt{\kappa_1 \kappa_2}}{\kappa/2 - i\Omega} & 0 \\ \sqrt{\frac{\kappa_2}{\kappa_1}} \mathcal{K}[\Omega] & \frac{\sqrt{\kappa_1 \kappa_2}}{\kappa/2 - i\Omega} \end{pmatrix} & \mathbf{L}_{\text{t}}[\Omega] &= \begin{pmatrix} \frac{\kappa_2}{\kappa/2 - i\Omega} - 1 & 0 \\ \frac{\kappa_2}{\kappa/2 - i\Omega} & \frac{\kappa_2}{\kappa/2 - i\Omega} - 1 \end{pmatrix} \end{aligned}$$

**Convergence to VIRGO/LIGO notation:** To sanity check this expression, we need to make sure we recover the standard expressions used in the LIGO/VIRGO community. This is we will assume the mechanical resonator is free, that is  $\Omega_m \rightarrow 0$  and  $\Gamma_m \rightarrow 0$ . The susceptibility then reduces to  $\chi[\Omega] = 1/M\Omega^2$ , and we will consider sideband frequencies  $\Omega \ll \kappa/2$  such that all terms in  $\Omega/(\kappa/2)$  can be neglected. We also consider a single port cavity such that  $\kappa_1 = \kappa$  and  $\kappa_2 = 0$ . The reflected quadrature fluctuations then read

$$\delta\hat{\mathbf{u}}_{\text{r}}[\Omega] = \begin{pmatrix} 1 & 0 \\ \frac{32\omega_0 P_{\text{in}}}{ML^2 \kappa^2 \Omega^2} & 1 \end{pmatrix} \delta\hat{\mathbf{u}}_{\text{in}}[\Omega]. \quad (\text{I.131})$$

In GW papers, the pre factor will often be 8 (and not 32) as they use the cavity half width at half maximum rather than  $\kappa$ . We indeed recover the standard expression used in the GW community, which is a good sanity check of our derivation. We do stress however that this expression is only valid for a free mass, and that the full expression including the mechanical resonance is required to describe optomechanical cavities in general.

**Reflected spectra:** We can now compute the covariance matrix of the reflected quadratures, assuming vacuum fluctuations both at the input and at the loss port. We additionally consider a quasi single port cavity for simplicity  $\kappa_1 \gg \kappa_2$ , such that  $\kappa_1 \sim \kappa$ , as well as the bad cavity limit  $\Omega \ll \kappa/2$ . The reflected covariance matrix is then given by

$$\mathbf{S}_r[\Omega] = \mathbf{T}_r[\Omega]\mathbf{S}_{\text{in}}[\Omega]\mathbf{T}_r^\dagger[\Omega] = \begin{pmatrix} 1 & \mathcal{K}[\Omega] \\ \mathcal{K}^*[\Omega] & 1 + |\mathcal{K}[\Omega]|^2 \end{pmatrix} \quad (\text{I.132})$$

where the off-diagonal entries are complex conjugates of each other, ensuring the covariance matrix is Hermitian as required. The diagonal terms are the amplitude and phase noise spectra respectively, while the off-diagonal terms quantify correlations between amplitude and phase. The presence of these correlations is the hallmark of optomechanical/ponderomotive squeezing i.e. using the non linear response of the resonator to squeeze light. This effect is not seen nor sought in our experiment, but is a very active field of research in the optomechanics community.

One now sees two essential components in the reflected phase spectrum. The first is the direct phase fluctuations, which is simply shot noise seen as 1. The second is the back-action term  $\propto |\mathcal{K}[\Omega]|^2$ , which is the phase fluctuations induced by the resonator motion driven by radiation pressure fluctuations.



## Chapter II

# Theory: Frequency Dependent Squeezing & Membrane based Optomechanics

This chapter will cover the elementary concepts required to describe an membrane based optomechanical system in a quantum regime. We will first recall basics on optical field quantization as well describing coherent and squeezed light field, to then turn to the more specific frequency dependent squeezed light field. Secondly, we will cover the mathematical description of a mechanical resonator interacting with a generic coherent optical field, highlighting the differences with the seminal optomechanical system of a mirror on a spring. Finally, we will derive the equations of motions of a membrane based optomechanical system with frequency dependent squeezed optical fields.

## Contents

---

<b>II.1 Squeezed Light and Optomechanics . . . . .</b>	<b>45</b>
II.1.1 Standard Quantum Limit . . . . .	45
II.1.2 Frequency Independent Squeezing in Optomechanical Cavities . . . . .	48
II.1.3 Frequency Dependent Squeezing in Optomechanical Cavities . . . . .	50
II.1.4 Filter Cavities for Frequency Dependent Squeezing . . . . .	51
<b>II.2 Cavity Optomechanics with Membrane based systems . . . . .</b>	<b>52</b>
II.2.1 Classical Description . . . . .	52
II.2.2 Quantum Langevin Equations . . . . .	53
II.2.3 Mechanical Resonators . . . . .	58
II.2.4 Noise spectra . . . . .	58

---

## II.1 Squeezed Light and Optomechanics

We will now introduce the concept of Standard Quantum Limit (SQL) in the context of optomechanical measurements, and show how frequency dependent squeezed light can be used to surpass this limit.

For the rest of this section we will assume the following

- A cavity on resonance:  $\Delta = 0$ .
- A single port optomechanical cavity:  $\kappa_1 \sim \kappa$ .
- The unresolved sideband regime:  $(\Omega, \Omega_m) \ll \kappa/2$ .

### II.1.1 Standard Quantum Limit

The question of interest is now:

**what is the best displacement sensitivity one can achieve?**

We start by recalling the reflected phase fluctuation of an optomechanical cavity from section II.2.5 under the aforementioned assumptions:

$$\delta\hat{q}_r[\Omega] = \delta\hat{q}_{\text{in}}[\Omega] + \mathcal{K}[\Omega] \delta\hat{p}_{\text{in}}[\Omega] \quad \text{with} \quad \mathcal{K}[\Omega] = \frac{128\hbar\mathcal{F}^2\bar{I}_{\text{in}}}{\lambda^2} \chi[\Omega]$$

as well as the phase to displacement transduction relation with an optomechanical escape efficiency of 1:

$$\delta\hat{q}_x = \frac{16\mathcal{F}\sqrt{\bar{I}_{\text{in}}}}{\lambda} \delta\hat{x}[\Omega]$$

Using these two relations, we can then express displacement fluctuations in terms of input amplitude and phase fluctuations, assuming the reflected field is a perfect probe of the mechanical resonator position fluctuations i.e.  $\delta\hat{q}_r[\Omega] = \delta\hat{q}_x[\Omega]$ . This treatment is formally equivalent to considering the output phase as a statistical estimator of the position fluctuations being a stationary random process as done in quantum measurement theory [?]. We then write

$$\delta\hat{x}[\Omega] = \frac{\lambda}{16\mathcal{F}\sqrt{\bar{I}_{\text{in}}}} \delta\hat{q}_{\text{in}}[\Omega] + \frac{8\hbar\mathcal{F}\sqrt{\bar{I}_{\text{in}}}}{\lambda} \chi[\Omega] \delta\hat{p}_{\text{in}}[\Omega] \quad (\text{II.1})$$

such that the associated displacement spectrum reads

$$S_{xx}[\Omega] = \frac{\lambda^2}{256\mathcal{F}^2\bar{I}_{\text{in}}} S_{qq}^{\text{in}}[\Omega] + \frac{64\hbar^2\mathcal{F}^2\bar{I}_{\text{in}}}{\lambda^2} |\chi[\Omega]|^2 S_{pp}^{\text{in}}[\Omega] + \hbar|\chi[\Omega]| \text{Re} \left[ e^{i\phi_m[\Omega]} S_{pq}^{\text{in}}[\Omega] \right] \quad (\text{II.2})$$

We then identify three contributions to the displacement spectrum:

- The first term is the laser shot noise (or imprecision noise) scaling inversely with the input power  $\bar{I}_{\text{in}}$ , arising from the input phase fluctuations  $S_{qq}^{\text{in}}[\Omega]$  and given by

$$S_{xx}^{\text{SN}}[\Omega] = \frac{\lambda^2}{256\mathcal{F}^2\bar{I}_{\text{in}}} S_{qq}^{\text{in}}[\Omega] \quad (\text{II.3})$$

- The second term is the radiation pressure noise (or backaction noise) scaling linearly with the input power  $\bar{I}_{\text{in}}$ , arising from the input amplitude fluctuations  $S_{pp}^{\text{in}}[\Omega]$  driving the mechanical resonator via radiation pressure given by

$$S_{xx}^{\text{RPN}}[\Omega] = \frac{64\hbar^2\mathcal{F}^2\bar{I}_{\text{in}}}{\lambda^2} |\chi[\Omega]|^2 S_{pp}^{\text{in}}[\Omega] \quad (\text{II.4})$$

- The third term is a correlation term between amplitude and phase fluctuations  $S_{pq}^{\text{in}}[\Omega]$ , which can be non-zero for arbitrary squeezed states as seen in the previous section and given by

$$S_{xx}^{\text{cor}}[\Omega] = \hbar|\chi[\Omega]| \operatorname{Re} \left[ e^{i\phi_m[\Omega]} S_{pq}^{\text{in}}[\Omega] \right] \quad (\text{II.5})$$

And we write the total displacement spectrum as the sum of these three contributions

$$S_{xx}[\Omega] = S_{xx}^{\text{SN}}[\Omega] + S_{xx}^{\text{RPN}}[\Omega] + S_{xx}^{\text{cor}}[\Omega] \quad (\text{II.6})$$

We now consider vacuum/coherent fluctuations such that  $S_{qq}^{\text{in}}[\Omega] = S_{pp}^{\text{in}}[\Omega] = 1$  and  $S_{pq}^{\text{in}}[\Omega] = 0$ , so that the displacement spectrum simplifies to

$$S_{xx}[\Omega] = \frac{\lambda^2}{256\mathcal{F}^2\bar{I}_{\text{in}}} + \frac{64\hbar^2\mathcal{F}^2\bar{I}_{\text{in}}}{\lambda^2} |\chi[\Omega]|^2 \quad (\text{II.7})$$

and we look at what noise dominates the displacement spectrum around the mechanical resonance  $\Omega \sim \Omega_m$ . We define the frequency  $\Omega_{\text{SQL}}$  as the frequency at which the SQL is achieved, given by

$$\Omega_{\text{SQL}}^{\pm} = \sqrt{\Omega_m^2 - \frac{\Gamma_m^2}{2}} \pm \frac{1}{2} \sqrt{\Gamma_m^4 - 4\Gamma_m^2\Omega_m^2 + \left( \frac{256\hbar\mathcal{F}^2\bar{I}_{\text{in}}}{m\lambda^2} \right)^2} \quad (\text{II.8})$$

and consistent with the LIGO/Virgo notation [?, ?]. Over the frequency range of interest  $\Omega \in [\Omega_m - \Omega_{\text{SQL}}, \Omega_m + \Omega_{\text{SQL}}]$ , the displacement noise is dominated by the radiation pressure noise, while outside this range, the noise is dominated by the shot noise. However, for every sideband frequency, there exists an optimal input power  $\bar{I}_{\text{in}}^{\text{SQL}}[\Omega]$  at which both contributions are equal, minimizing the total displacement noise. This limit is called the Standard Quantum Limit (SQL) and is a direct consequence of Heisenberg's uncertainty principle applied

to continuous position measurements [?, ?]. This SQL intensity is given by

$$S_{xx}^{\text{SN}}[\Omega] = S_{xx}^{\text{RPN}}[\Omega] \implies \bar{I}_{\text{in}}^{\text{SQL}}[\Omega] = \frac{\lambda^2}{128\mathcal{F}^2\hbar|\chi[\Omega]|} \quad (\text{II.9})$$

such that plugging back in this SQL intensity in (II.7) gives the SQL displacement spectrum as

$$S_{xx}^{\text{SQL}}[\Omega] = \hbar|\chi[\Omega]| \implies S_{xx}^{\text{SN}}[\Omega] + S_{xx}^{\text{RPN}}[\Omega] \geq \hbar|\chi[\Omega]| \quad (\text{II.10})$$

which is the fundamental limit to continuous position measurements with coherent light. We also note that for high Q resonators,  $\Omega_{SQL} \ll \Gamma_m$ , so approximating the susceptibility by its real part holds over a relatively large frequency range.

### Thermal Noise

Thermal noise is a major limitation in optomechanical experiments, as it can mask the quantum effects one aims to observe. The mechanical resonator is indeed coupled to a thermal bath at temperature  $T$ , which drives the resonator into a thermal state with mean phonon occupation number  $\bar{n}_{\text{th}} = k_B T / (\hbar\Omega_m)$  in the high temperature limit  $k_B T \gg \hbar\Omega_m$ . The position fluctuations induced by this thermal force is given by

$$S_{xx}^{\text{th}}[\Omega] = \frac{2\hbar}{1 - e^{-\hbar\Omega/k_B T}} \text{Im } \chi[\Omega] \simeq 2m\Gamma_m k_B T |\chi[\Omega]|^2 \quad \text{if } k_B T \gg \hbar\Omega \quad (\text{II.11})$$

where we used the identity  $\text{Im } \chi[\Omega] = m\Gamma_m \Omega |\chi[\Omega]|^2$ . At  $T = 0K$ , this reduces to the zero point fluctuations spectrum  $S_{xx}^{\text{ZPF}}[\Omega] = m\Gamma_m \hbar\Omega_m |\chi[\Omega]|^2 < S_{xx}^{\text{SQL}}[\Omega]$ , such that is often neglected in the total displacement spectrum. However, at finite temperature, the thermal noise can be much larger than the SQL. Therefore, the total displacement spectrum now reads

$$S_{xx}[\Omega] = S_{xx}^{\text{SN}}[\Omega] + S_{xx}^{\text{RPN}}[\Omega] + S_{xx}^{\text{cor}}[\Omega] + S_{xx}^{\text{th}}[\Omega] \quad (\text{II.12})$$

In order to experimentally probe these quantum limits without being limited by various technical noises, one would then need:

- A high finesse cavity, such that the shot noise  $S_{xx}^{\text{SN}} \propto \mathcal{F}^{-2}$  level is low, and the radiation pressure noise  $S_{xx}^{\text{RPN}} \propto \mathcal{F}^2$  is high. One should however ensure the cavity bandwidth  $\kappa$  is still much larger than the mechanical frequency  $\Omega_m$ . This can be ensure tuning the cavity length  $L$  and mirror transmissions.
- A low mass, low frequency, high quality factor mechanical resonator, such that the susceptibility modulus at resonance  $|\chi[\Omega_m]| = Q/m\Omega_m^2$  is high, and it comes out of the shot noise level significantly.

- A low temperature environment, such that the thermal noise  $S_{xx}^{\text{th}} \propto T$  is low and does not mask the quantum effects. This can be ensured by cryogenic cooling of the mechanical resonator, as well as using high quality factor resonators to reduce the mechanical linewidth  $\Gamma_m$ .

We now want to derive the displacement spectrum of an optomechanical system driven by a squeezed light field, whether frequency independent or dependent.

### II.1.2 Frequency Independent Squeezing in Optomechanical Cavities

We first recall the (idealized) covariance matrices for both a phase squeezed field and an amplitude squeezed field

$$\mathbf{S}_{\text{OPO}}^0[\Omega] = \begin{pmatrix} e^{+2r} & 0 \\ 0 & e^{-2r} \end{pmatrix}, \quad \mathbf{S}_{\text{OPO}}^\pi[\Omega] = \begin{pmatrix} e^{-2r} & 0 \\ 0 & e^{+2r} \end{pmatrix}$$

For a phase squeezed field, the displacement spectrum reads

$$S_{xx}^0[\Omega] = \frac{\lambda^2}{256\mathcal{F}^2\bar{I}_{\text{in}}}e^{-2r} + \frac{64\hbar^2\mathcal{F}^2\bar{I}_{\text{in}}}{\lambda^2}|\chi[\Omega]|^2e^{+2r} \quad (\text{II.13})$$

while for an amplitude squeezed field, the displacement spectrum reads

$$S_{xx}^\pi[\Omega] = \frac{\lambda^2}{256\mathcal{F}^2\bar{I}_{\text{in}}}e^{+2r} + \frac{64\hbar^2\mathcal{F}^2\bar{I}_{\text{in}}}{\lambda^2}|\chi[\Omega]|^2e^{-2r} \quad (\text{II.14})$$

We then see that phase squeezing reduces the shot noise contribution but increases the radiation pressure noise contribution, while amplitude squeezing reduces the radiation pressure noise contribution but increases the shot noise contribution. However, neither of these two configurations can reduce both contributions simultaneously, and therefore cannot improve the SQL limit. This is illustrated in figure II.2.

Now consider an input squeezed state with a frequency independent squeezing angle  $\theta = \pi/4$  with covariance matrix

$$\mathbf{S}_{\text{OPO}}^{\pi/4}[\Omega] = \begin{pmatrix} \cosh 2r & -\sinh 2r \\ -\sinh 2r & \cosh 2r \end{pmatrix}.$$

The resulting displacement spectrum then reads

$$S_{xx}^{\pi/4}[\Omega] = \left( \frac{\lambda^2}{256\mathcal{F}^2\bar{I}_{\text{in}}} + \frac{64\hbar^2\mathcal{F}^2\bar{I}_{\text{in}}}{\lambda^2}|\chi[\Omega]|^2 \right) \cosh 2r - \hbar|\chi[\Omega]|\sinh 2r \cos \phi_m[\Omega] \quad (\text{II.15})$$

and we seek the frequency range where the displacement spectrum is below the SQL, i.e.

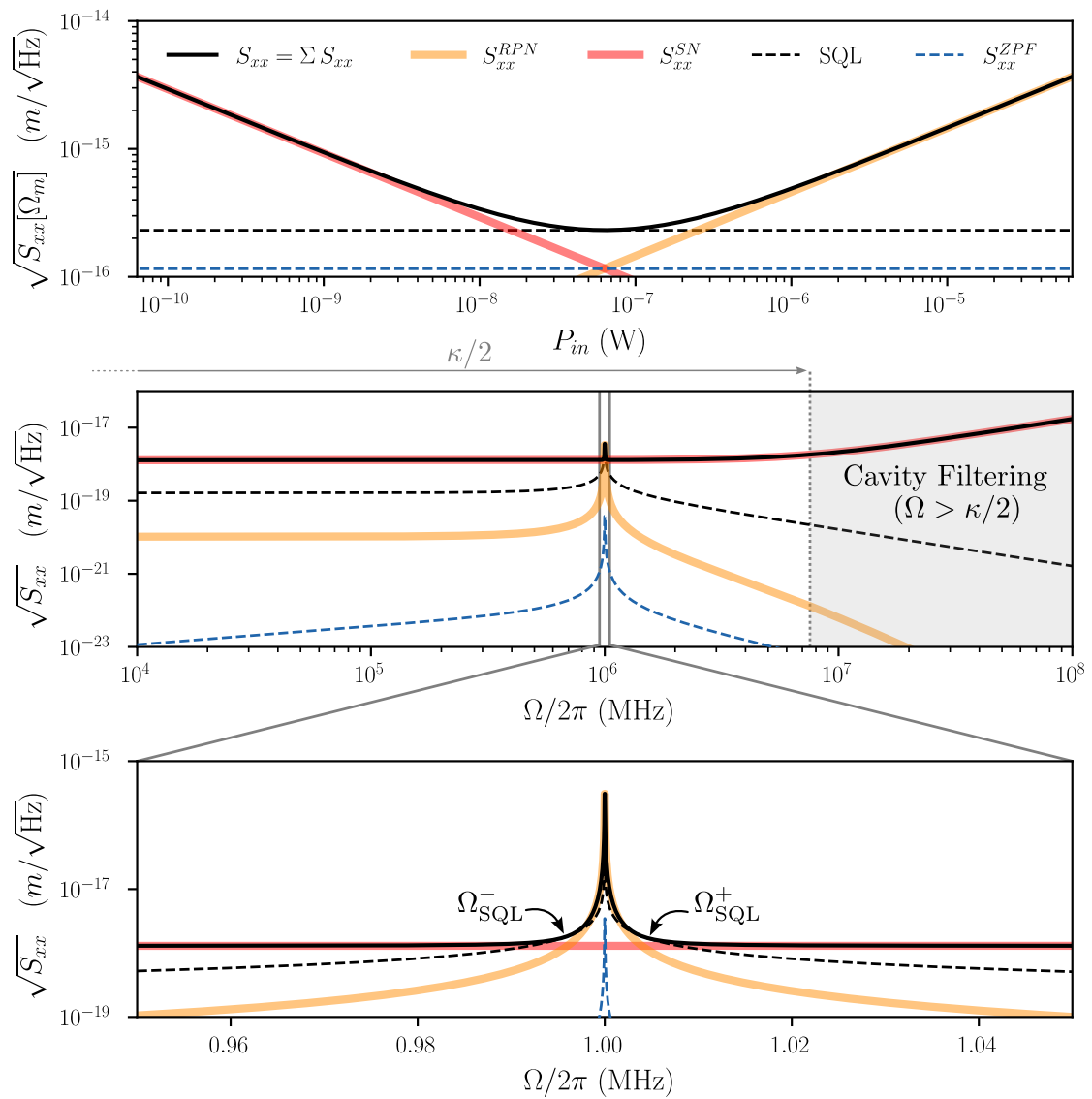


Fig. II.1 DYes

$S_{xx}^{\pi/4}[\Omega] < S_{xx}^{\text{SQL}}[\Omega]$ . This condition is satisfied when

$$\tanh \frac{r}{2} < \cos \phi_m[\Omega] < 1 \quad (\text{II.16})$$

Because  $\tanh r/2$  tends to 1 as  $r$  increases, the frequency range where the displacement spectrum is below the SQL decreases with increasing squeezing factor  $r$ . Furthermore, due to the interplay between quadrature correlations and the projection of the  $\pi/4$  ellipse onto the output quadrature axis, acting as an effective increase of the radiation pressure noise with effective intensity  $\cosh r \bar{I}_{\text{in}}$ , there is an effective range of  $r$  above which the displacement spectrum is always above the SQL (for a fixed input intensity). This is illustrated in figure II.2.

Additionally, and as seen in Fig ..., the optimal angle to maximally reduce the displacement spectrum varies with frequency, being 0 at frequencies outside the resonator's bandwidth,  $\pi/2$  at the mechanical resonance frequency  $\Omega_m$ , and about  $\pm\pi/4$  at  $\Omega_m \pm \Gamma_m$ . This motivates the use of frequency dependent squeezed states to reduce the displacement spectrum below the SQL over a broad frequency range, where every sideband frequency needs to be rotated by a different angle to minimize the displacement spectrum.

### II.1.3 Frequency Dependent Squeezing in Optomechanical Cavities

We now consider a frequency dependent squeezed state with covariance matrix

$$\mathbf{S}_{\text{OPO}}^\theta[\Omega] = \begin{pmatrix} \cosh 2r - \sinh 2r \cos 2\theta[\Omega] & -\sinh 2r \sin 2\theta[\Omega] \\ -\sinh 2r \sin 2\theta[\Omega] & \cosh 2r + \sinh 2r \cos 2\theta[\Omega] \end{pmatrix}$$

The resulting displacement spectrum then reads

$$\begin{aligned} S_{xx}[\Omega] = & S_{xx}^{\text{SN}}[\Omega](\cosh 2r + \sinh 2r \cos 2\theta[\Omega]) \\ & + S_{xx}^{\text{RPN}}[\Omega](\cosh 2r - \sinh 2r \cos 2\theta[\Omega]) \\ & - \hbar |\chi[\Omega]| \operatorname{Re} [e^{i\phi_m[\Omega]} \sinh 2r \sin 2\theta[\Omega]] \end{aligned} \quad (\text{II.17})$$

As shown in the annex, picking the squeezing angle as

$$\theta[\Omega] = \arctan \left[ \frac{2|\mathcal{K}[\Omega]| \cos \phi_m[\Omega]}{1 + |\mathcal{K}[\Omega]|^2} \right] \quad (\text{II.18})$$

minimizes the displacement spectrum at every sideband frequency, leading to

$$S_{xx}[\Omega] \approx e^{-2r} \left( \frac{\lambda^2}{256\mathcal{F}^2 \bar{I}_{\text{in}}} + \frac{64\hbar^2 \mathcal{F}^2 \bar{I}_{\text{in}}}{\lambda^2} |\chi[\Omega]|^2 \right) \quad (\text{II.19})$$

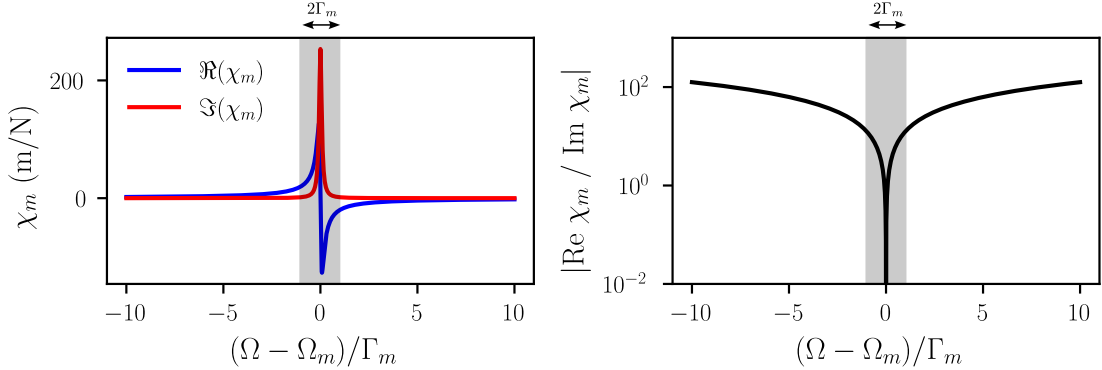


Fig. II.2 DYes

where we assumed the mechanical susceptibility is mainly defined by its real component, such that  $\chi[\Omega] \sim \text{Re } \chi[\Omega]$  as discussed previously. This broadband reduction of the displacement spectrum below the SQL is illustrated in figure ???. We can also see that for sufficient squeezing factor  $r$ , the displacement spectrum can, in principle, be reduced to the thermal noise level. One could then imagine using this quantum limited position readout to feedback cool and stabilize the mechanical resonator to its quantum ground state.

**Convergence to VIRGO/LIGO notation:** We once again show that this general treatment converges to the one used in the context of gravitational wave detectors. In the free mass regime,  $\mathcal{K}[\Omega]$  is real, such that  $\phi_m[\Omega] = 0$ . One can then rewrite the optimal squeezing angle as

$$\theta[\Omega] = \arctan \left[ \frac{2\mathcal{K}[\Omega]}{1 + \mathcal{K}^2[\Omega]} \right] = \arctan \mathcal{K}[\Omega] \quad (\text{II.20})$$

where we used the identity  $\arctan 2x/(1 + x^2) = 2 \arctan x \pmod{\pi}$ , such that this comes down to the expression used in the context of gravitational wave detectors [?, ?].

#### II.1.4 Filter Cavities for Frequency Dependent Squeezing

To generate frequency dependent squeezed states, one can use a filter cavity to rotate the squeezing angle in a frequency dependent manner. The filter cavity is a detuned optical cavity, such that such that symmetrical sidebands around the carrier will experience different phase shifts upon reflection.

Recalling the transfer matrix for a detuned single port cavity from the previous chapter

$$\mathbf{T}_r[\Omega] = \boldsymbol{\Gamma} \mathbf{r}_\Delta[\Omega] \boldsymbol{\Gamma}^{-1} = \frac{1}{2} \begin{pmatrix} r_\Delta[\Omega] + r_\Delta^*[-\Omega] & i(r_\Delta[\Omega] - r_\Delta^*[-\Omega]) \\ -i(r_\Delta[\Omega] - r_\Delta^*[-\Omega]) & r_\Delta[\Omega] + r_\Delta^*[-\Omega] \end{pmatrix} \quad (\text{II.21})$$

## II.2 Cavity Optomechanics with Membrane based systems

### II.2.1 Classical Description

To gain intuition and derive elementary parameters used in the next section, we first describe the classical fields  $\alpha_L$  and  $\alpha_R$  propagating in a three mirror cavity where a membrane with complex amplitude reflection and transmission coefficients  $r_m = |r_m|e^{i\phi_r}$  and  $t_m = |t_m|e^{i\phi_t}$  is placed between two high reflectivity mirrors of amplitude reflection coefficients  $\sim -1$ . The membrane splits the cavity in two sub-cavities of lengths  $L_1$  and  $L_2$ , with  $L = L_1 + L_2$  the total cavity length. The membrane is initially at mean position  $x = 0$ , and is modelled as a thin dielectric slab of thickness  $d$  and refractive index  $n$ , with amplitude reflection and transmission coefficients  $r_m$  and  $t_m$  given by [?]

$$r_m = \frac{(n^2 - 1) \sin knd}{2in \cos knd + (n^2 + 1) \sin knd}, \quad t_m = \frac{2n}{2in \cos knd + (n^2 + 1) \sin knd}. \quad (\text{II.22})$$

In the lossless case, we will assume the index of refraction  $n$  is real, such that  $|r_m|^2 + |t_m|^2 = 1$ . The cavity fields are then written as

$$\begin{aligned} \alpha_R &= t_m \alpha_L + r_m \alpha'_R \\ \alpha'_L &= t_m \alpha'_R + r_m \alpha_L. \end{aligned} \quad (\text{II.23})$$

In this case, energy conservation i.e.  $|\alpha_L|^2 + |\alpha'_R|^2 = |\alpha'_L|^2 + |\alpha_R|^2$  imposes that  $2(\phi_t - \phi_r) = \pi$  such that we can chose  $r_m = |r_m|$  and  $t_m = i|t_m|$ . We rewrite the the cavity fields by injecting the identities  $\alpha_L = -\alpha'_L e^{2ikL_1}$  and  $\alpha'_R = -\alpha_R e^{2ikL_2}$  i.e. end mirror reflectivities of -1, leading to

$$(t_m^2 - r_m^2)e^{ikL} - e^{-ikL} = 2r_m \cos(2kL_2 - kL) \quad (\text{II.24})$$

leading to the transcendental equation [?]

$$-\cos kL = |r_m| \cos(2kL_2 - kL) \quad (\text{II.25})$$

Following the method in Sankey et al. [?], we then derive the cavity resonance frequencies as a function of the membrane position  $x$  around its mean position  $x = 0$ . We will also always consider a long cavity such that  $L \gg \lambda, x$ . Consequently, the small displacement  $x$  of the membrane around its mean position will weakly affect the cavity resonance frequencies such that

The cavity sublengths considering a non zero mean membrane position are then  $L_1 \rightarrow L_1 + x$  and  $L_2 \rightarrow L_2 - x$ . The above equation then becomes

$$-\cos kL = |r_m| \cos(2k(L_2 - L_1) - 2kx) \quad (\text{II.26})$$

We now consider cases : the historical Membrane In the Middle (MIM) model where  $L_1 \sim L_2 \sim L/2$ , and the less studied Membrane At The Edge (MATE) model where  $L_1 \sim L \gg L_2$ . By considering that the membrane displacement perturbs the cavity resonance frequency by an amount at most of the order of one FSR, expanding the cosine on both sides with the standard trigonometric identities leads to

$$\begin{aligned} \text{MIM: } \omega_c(x) &\simeq N\omega_{FSR} + \frac{c}{L} \arccos\left((-1)^{N+1}|r_m| \cos 2kx\right) \\ \text{MATE: } \omega_c(x) &\simeq N\omega_{FSR} + \frac{c}{L} \arctan\left(-\frac{1 + |r_m| \cos 2kx}{|r_m| \sin 2kx}\right) \end{aligned} \quad (\text{II.27})$$

### II.2.2 Quantum Langevin Equations

Using the same tools as in section II.2, we can derive the QLE of a membrane based optomechanical system. The transmissive membrane splits the cavity in two sub-cavities of lengths  $L_1$  and  $L_2$ , with  $L = L_1 + L_2$  the total cavity length. The membrane position operator is described by annihilation operator  $\hat{x} \propto \hat{c} + \hat{c}^\dagger$  as in the previous section. The central difference with the standard book-keeping optomechanical system of a mirror on a spring is that the membrane splits the cavity in two sub-cavities, such that two bosonic operators  $\hat{a}_L$  and  $\hat{a}_R$  are required to describe the intracavity fields. The membrane position then modifies the resonance frequencies of the two subcavities, such that they both depend on the membrane position as  $\omega_L(x)$  and  $\omega_R(x)$  but with inverse trend: when one cavity shortens and its FSR increases, the other lengthens and its FSR decreases. To first order, we can linearize the resonance frequencies as

$$\omega_L(\hat{x}) \simeq \omega_{L,0} + G_L \hat{x}, \quad \omega_R(\hat{x}) \simeq \omega_{R,0} + G_R \hat{x}, \quad (\text{II.28})$$

with  $G_L = \omega_{L,0}/L_1$  and  $G_R = -\omega_{R,0}/L_2$  the optomechanical couplings of the two subcavities, and where  $\omega_{L,0}$  and  $\omega_{R,0}$  are the unperturbed resonance frequencies of the two subcavities. The system now features a network of optical modes varying linearly with the membrane position, coupled by the membrane transmission. The Hamiltonian of this system can then be written as

$$\begin{aligned} \hat{H} &= \hbar \omega_{L,0} \hat{a}_L^\dagger \hat{a}_L + \hbar \omega_{R,0} \hat{a}_R^\dagger \hat{a}_R + \hbar \Omega_m \hat{c}^\dagger \hat{c} \\ &\quad + \hbar (G_L \hat{a}_L^\dagger \hat{a}_L + G_R \hat{a}_R^\dagger \hat{a}_R) \hat{x} \\ &\quad - \hbar J (\hat{a}_L^\dagger \hat{a}_R + \hat{a}_R^\dagger \hat{a}_L) \end{aligned} \quad (\text{II.29})$$

where we only considered one cavity mode per subcavity, and where  $J$  is the photon tunneling rate through the membrane, proportional to the membrane transmission  $t_m$ . The first line describes the free evolution of the two subcavity modes and the mechanical resonator, the

second line describes the optomechanical interaction between the membrane position and the two subcavity modes, while the third line describes the photon tunneling through the membrane.

### Classical Description : Closed cavity model

We start by describing the classical behaviour of the cavity. Considering a high finesse cavity, with high reflectivity mirrors  $r_1, r_2 \approx 1$ , the cavity fields are written as

$$\alpha_1 = \alpha'_1 \quad (\text{II.30})$$

where  $E_{\text{in}}$  is the input field,  $E_1$  the intracavity field before the membrane,  $E_2$  the intracavity field after the membrane,  $E_3$  the transmitted field and  $E_4$  the reflected field. The cavity resonance frequencies are then obtained by solving these equations in the absence of input field  $E_{\text{in}} = 0$ , leading to the transcendental equation [?]

We describe the subcavity modes by annihilation operators  $\hat{a}_1$  and  $\hat{a}_2$ , with unperturbed resonance frequencies  $\omega_1$  and  $\omega_2$ . The membrane position operator is described by annihilation operator  $\hat{x} \propto \hat{c} + \hat{c}^\dagger$  as in the previous section. Considering how the membrane position under the effect of radiation pressure modifies the resonance frequencies of the two subcavities, the subcavity length can be written as  $L_1 = L_{1,0} + x$  and  $L_2 = L_{2,0} - x$ , with  $L_{1,0}$  and  $L_{2,0}$  the equilibrium lengths, and  $x$  the mean static displacement of the membrane. This mean displacement being small compared to the cavity length, we can linearize the resonance frequencies as

$$\omega_1(x) \simeq \omega_0 + G_1 x, \quad \omega_2(x) \simeq \omega_0 - G_2 x, \quad (\text{II.31})$$

with  $G_1 = \omega_0/L_{1,0}$  and  $G_2 = \omega_0/L_{2,0}$  the optomechanical couplings of the two subcavities, and where  $\omega_0$  is the common frequency of the two modes i.e.  $\omega_{1,0} = \omega_{2,0} = \omega_0$ . The system now features a network of optical modes varying linearly with the membrane position, coupled by the membrane transmission. The Hamiltonian of the system is then given by [?]

$$\hat{H} = \hbar\omega_1(x)\hat{a}_1^\dagger\hat{a}_1 + \hbar\omega_2(x)\hat{a}_2^\dagger\hat{a}_2 + \hbar g(\hat{a}_1^\dagger\hat{a}_2 + \hat{a}_2^\dagger\hat{a}_1) + \frac{\hat{p}^2}{2m} + \frac{1}{2}m\omega_m^2\hat{x}^2 \quad (\text{II.32})$$

Two configurations are then possible: position the membrane at approximately half the total cavity length  $L/2$ , such that  $L_{1,0} \simeq L_{2,0}$  and  $G_1 \simeq G_2$ ; or position the membrane close to one of the mirrors, such that one subcavity is much shorter than the other, e.g.  $L_{1,0} \gg L_{2,0}$  and  $G_1 \ll G_2$ . The first configuration is called the *membrane-in-the-middle* (MIM) configuration, while the second one is called the *membrane-at-the-edge* (MATE) configuration. The MIM configuration has been widely studied in the literature [?, ?, ?, ?], and

has been used to demonstrate various quantum effects such as ponderomotive squeezing [?], quantum non-demolition measurements of phonon number [?], or ground-state cooling of a mechanical resonator [?]. However, the MIM configuration suffers from a low optomechanical coupling rate due to the small value of  $G_{1,2}$ , which limits its use for quantum experiments. The MATE configuration has been less studied, but offers a much larger optomechanical coupling rate due to the large value of  $G_1$ . This makes it a promising candidate for quantum experiments. In this work, we will focus on the MATE configuration.

### Set-up and notation

We consider a three-mode optical model for a membrane-at-the-edge (MATE) cavity with a *highly transmissive* middle membrane. The long cavity mode is denoted by  $a$ ; the short cavity contributes two nearby modes,  $b_+$  and  $b_-$ , centered  $\pm\lambda/4$  away in displacement. In the mode basis  $(a, b_+, b_-)^\top$  we take (with  $\hbar = 1$ )

$$\mathbf{H} = \begin{pmatrix} \delta_a & J & -J \\ J & \delta_+ & 0 \\ -J & 0 & \delta_- \end{pmatrix}, \quad \begin{aligned} \delta_a &= r_m G_1 \Delta x, \\ \delta_\pm &= r_m G_2 \left( \Delta x \mp \frac{\lambda}{4} \right), \end{aligned} \quad (\text{II.33})$$

with

$$J = \frac{c t_m}{2\sqrt{L_1 L_2}}, \quad t_m^2 + r_m^2 = 1, \quad G_1 = \frac{\omega_0}{L_1}, \quad G_2 = -\frac{\omega_0}{L_2}. \quad (\text{II.34})$$

Here  $\Delta x$  is the membrane displacement from the symmetry point,  $\lambda$  the optical wavelength,  $t_m$  ( $r_m$ ) the middle-membrane amplitude transmission (reflection), and  $L_{1,2}$  the long/short sub-cavity lengths. High transmissivity means  $r_m \ll 1$  while  $J = O(t_m)$  can be sizable.

The exact normal modes are eigenoperators  $A_k = \alpha_k a + \beta_k b_+ + \gamma_k b_-$  obtained from  $(\mathbf{H} - \omega_k \mathbb{I})(\alpha_k, \beta_k, \gamma_k)^\top = 0$ . From the lower rows one finds the exact amplitude ratios

$$\frac{\beta_k}{\alpha_k} = -\frac{J}{\delta_+ - \omega_k}, \quad \frac{\gamma_k}{\alpha_k} = +\frac{J}{\delta_- - \omega_k}. \quad (\text{II.35})$$

The “physical” orange branch in the figures is the one continuously connected to the long-cavity mode  $a$ .

### Time-domain adiabatic elimination

Away from the two avoided crossings at  $\Delta x \approx \pm\lambda/4$ , the short-cavity detunings  $|\delta_\pm - \omega|$  are large compared to the coupling:

$$\varepsilon_\pm \equiv \frac{J}{|\delta_\pm - \omega|} \ll 1. \quad (\text{II.36})$$

The Heisenberg equations generated by (II.33) read

$$\begin{aligned} i\dot{a} &= \delta_a a + Jb_+ - Jb_-, \\ i\dot{b}_+ &= \delta_+ b_+ + Ja, \\ i\dot{b}_- &= \delta_- b_- - Ja. \end{aligned} \quad (\text{II.37})$$

The fast spectators  $b_{\pm}$  can be slaved to the slow variable  $a$  by setting  $\dot{b}_{\pm} \simeq 0$  to leading order:

$$b_+ \simeq -\frac{J}{\delta_+} a, \quad b_- \simeq -\frac{J}{\delta_-} a. \quad (\text{II.38})$$

Substituting (II.38) into the  $a$  equation in (II.37) gives an effective single-mode dynamics

$$i\dot{a} = \left[ \delta_a - J^2 \left( \frac{1}{\delta_+} + \frac{1}{\delta_-} \right) \right] a. \quad (\text{II.39})$$

Equation (II.39) shows that, in the dispersive region, the spectators do not acquire population to leading order; they merely induce a frequency (phase) shift of the  $a$  mode of order  $J^2/\delta_{\pm}$ .

If optical losses are included as  $\kappa_a, \kappa_{\pm}$  (phenomenologically via  $\delta_a \rightarrow \delta_a - i\kappa_a/2$  etc.), the same elimination yields

$$i\dot{a} = \left[ \delta_a - \frac{i\kappa_a}{2} - J^2 \left( \frac{1}{\delta_+ - i\kappa_+/2} + \frac{1}{\delta_- - i\kappa_-/2} \right) \right] a, \quad (\text{II.40})$$

and the validity condition strengthens to  $J \ll \sqrt{\Delta_{\pm}^2 + \kappa_{\pm}^2/4}$  with  $\Delta_{\pm} = \text{Re}(\delta_{\pm} - \omega)$ .

**Connection to eigenvectors.** Using (II.35), for the branch connected to  $a$  one has  $|\beta/\alpha|, |\gamma/\alpha| = O(\varepsilon_{\pm}) \ll 1$ . Thus the  $b_{\pm}$  weights in the physical eigenoperator are  $O(\varepsilon_{\pm}^2)$ , fully consistent with the slaving picture (II.38).

### Closed form for the physical eigenfrequency

The exact eigenvalue equation for the orange branch obtained from the first row of  $(\mathbf{H} - \omega\mathbb{I})v = 0$  together with (II.35) is

$$\omega = \delta_a - J^2 \left( \frac{1}{\delta_+ - \omega} + \frac{1}{\delta_- - \omega} \right). \quad (\text{II.41})$$

In the dispersive regime  $|\delta_{\pm}| \gg |\omega|$  one can set  $\omega \rightarrow 0$  in the denominators at first order, giving the explicit approximation

$$\omega_{\text{phys}}(\Delta x) \approx r_m G_1 \Delta x - J^2 \left[ \frac{1}{r_m G_2(\Delta x - \frac{\lambda}{4})} + \frac{1}{r_m G_2(\Delta x + \frac{\lambda}{4})} \right].$$

(II.42)

Combining the two fractions yields a compact dispersive form

$$\boxed{\omega_{\text{phys}}(\Delta x) \approx r_m G_1 \Delta x - \frac{2J^2}{r_m G_2} \frac{\Delta x}{\Delta x^2 - (\lambda/4)^2}.} \quad (\text{II.43})$$

Close to the symmetry point  $|\Delta x| \ll \lambda/4$ , (II.43) becomes nearly linear:

$$\boxed{\omega_{\text{phys}}(\Delta x) \approx \underbrace{\left[ r_m G_1 + \frac{32J^2}{r_m G_2 \lambda^2} \right]}_{\text{renormalized slope}} \Delta x.} \quad (\text{II.44})$$

In the usual MATE limit  $L_1 \gg L_2$  (hence  $|G_1| \ll |G_2|$ ), the second term typically dominates the slope; this analytic form explains the gentle “tilt” of the orange branch between the two avoided crossings.

### Schrieffer–Wolff (block-diagonal) derivation

For completeness, write  $H = H_0 + V$  with  $H_0 = \text{diag}(\delta_a, \delta_+, \delta_-)$  and  $V = \begin{pmatrix} 0 & J & -J \\ J & 0 & 0 \\ -J & 0 & 0 \end{pmatrix}$ . Let  $S$  be anti-Hermitian satisfying  $[H_0, S] = -V$ . A suitable choice is

$$S = \begin{pmatrix} 0 & \frac{J}{\delta_a - \delta_+} & -\frac{J}{\delta_a - \delta_-} \\ -\frac{J}{\delta_a - \delta_+} & 0 & 0 \\ \frac{J}{\delta_a - \delta_-} & 0 & 0 \end{pmatrix}. \quad (\text{II.45})$$

The transformed Hamiltonian  $\tilde{H} = e^S H e^{-S} = H_0 + \frac{1}{2}[S, V] + O(J^3/\Delta^2)$  is block-diagonal to second order, with the  $a$  block

$$H_{\text{eff}}^{(a)} = \delta_a - J^2 \left( \frac{1}{\delta_+ - \delta_a} + \frac{1}{\delta_- - \delta_a} \right), \quad (\text{II.46})$$

which reduces to (II.42) when  $|\delta_{\pm}| \gg |\delta_a|$ . Residual  $a \leftrightarrow b_{\pm}$  couplings are suppressed to  $O(J^3/\Delta^2)$ .

### Local avoided crossings (breakdown of elimination)

Near  $\Delta x \simeq +\lambda/4$ , only  $b_+$  is near resonant; the relevant subspace is  $(a, b_+)$  with

$$H_{\text{loc}}^{(+)} = \begin{pmatrix} \delta_a & J \\ J & \delta_+ \end{pmatrix}, \quad \Rightarrow \quad \omega_{\pm}^{(+)} = \frac{\delta_a + \delta_{\pm}}{2} \pm \sqrt{\left( \frac{\delta_a - \delta_{\pm}}{2} \right)^2 + J^2}. \quad (\text{II.47})$$

The orange branch is the one connecting continuously to (II.43) away from the crossing. The same holds at  $\Delta x \simeq -\lambda/4$  with  $b_-$ . Adiabatic elimination is invalid in windows where

$\varepsilon_{\pm} \ll 1$ .

## Validity conditions and practical rule

The small parameter governing all steps is  $\varepsilon_{\pm} = J/|\delta_{\pm} - \omega|$ . With losses,  $\varepsilon_{\pm} = J/\sqrt{\Delta_{\pm}^2 + \kappa_{\pm}^2/4}$ . A conservative working criterion is

$$\max\{\varepsilon_+, \varepsilon_-\} \lesssim 0.2 - 0.3 \quad \Rightarrow \quad \text{errors in } \omega_{\text{phys}} \text{ are } O(\varepsilon^2), \text{ and } |b_{\pm}|^2/|a|^2 = O(\varepsilon^2). \quad (\text{II.48})$$

### Optional bright/dark re-basis

Defining  $b_s = (b_+ - b_-)/\sqrt{2}$  and  $b_d = (b_+ + b_-)/\sqrt{2}$ , one finds that  $a$  couples only to the *bright* mode  $b_s$  with strength  $\sqrt{2}J$ , while  $b_d$  is dark to first order. In this basis the cubic spectrum becomes a quadratic (for  $a, b_s$ ) plus a spectator  $b_d$  whose frequency lies near  $r_m G_2 \Delta x$  and mixes weakly via  $O(r_m G_2 \lambda/2)$ . This re-basis is often convenient for fitting and for visualizing how the orange branch acquires its dispersive tilt.

**Summary.** In a high- $T$  middle-membrane MATE system, the short-cavity modes are far detuned for most  $\Delta x$ . They can be adiabatically eliminated, yielding the explicit orange-branch dispersion (II.43) (or (II.44) near the center), with controlled accuracy quantified by  $\varepsilon_{\pm}$ . Only in narrow windows around  $\Delta x = \pm\lambda/4$  is a  $2 \times 2$  avoided-crossing description required.

### II.2.3 Mechanical Resonators

Mechanical Resonators

### II.2.4 Noise spectra

We will derive the Hamiltonian formalism of a three mirror cavity, and show how it can be used to describe the optomechanical coupling of a membrane in the cavity. We now have to consider two optical modes coupled to one another through the membrane transmittivities. The Hamiltonian of the system can be written as:

$$\hat{H} = \hbar\omega_1 \hat{a}_1^\dagger \hat{a}_1 + \hbar\omega_2 \hat{a}_2^\dagger \hat{a}_2 + \hbar g(\hat{a}_1^\dagger \hat{a}_2 + \hat{a}_2^\dagger \hat{a}_1) + \frac{\hat{p}^2}{2m} + \frac{1}{2}m\omega_m^2 \hat{x}^2 \quad (\text{II.49})$$

where  $\hat{a}_1$  and  $\hat{a}_2$  are the annihilation operators of the two optical modes,  $\omega_1$  and  $\omega_2$  their respective frequencies,  $g$  the optomechanical coupling strength,  $\hat{p}$  and  $\hat{x}$  the momentum and

position operators of the membrane,  $m$  its mass and  $\omega_m$  its mechanical frequency. The optomechanical coupling strength  $g$  is defined as:

$$g = \frac{\omega_1}{L} \sqrt{\frac{\hbar}{2m\omega_m}} (T_1 + T_2) \quad (\text{II.50})$$

where  $T_1$  and  $T_2$  are the transmitivities of the two optical modes through the membrane. The Hamiltonian can be diagonalized by introducing the normal modes of the system, which are the eigenstates of the Hamiltonian. The normal modes can be expressed as:

$$\hat{b}_1 = \frac{1}{\sqrt{2}} (\hat{a}_1 + \hat{a}_2), \quad \hat{b}_2 = \frac{1}{\sqrt{2}} (\hat{a}_1 - \hat{a}_2) \quad (\text{II.51})$$

The normal modes  $\hat{b}_1$  and  $\hat{b}_2$  are the symmetric and antisymmetric modes of the system, respectively. The Hamiltonian can then be rewritten in terms of the normal modes as:

$$\hat{H} = \hbar\omega_1 \hat{b}_1^\dagger \hat{b}_1 + \hbar\omega_2 \hat{b}_2^\dagger \hat{b}_2 + \hbar g (\hat{b}_1^\dagger \hat{b}_2 + \hat{b}_2^\dagger \hat{b}_1) + \frac{\hat{p}^2}{2m} + \frac{1}{2} m \omega_m^2 \hat{x}^2 \quad (\text{II.52})$$

**Diagonalisation of two non-degenerate, tunnel-coupled optical cavities.** Let  $a_1$  and  $a_2$  (with the usual bosonic commutation relations) annihilate photons in the first and second cavity, whose bare resonance frequencies are  $\omega_1 \neq \omega_2$ . Photon tunnelling at rate  $J > 0$  through the semi-transparent middle mirror couples the two modes, giving the second-quantised Hamiltonian

$$H = \hbar \begin{pmatrix} a_1^\dagger & a_2^\dagger \end{pmatrix} \underbrace{\begin{pmatrix} \omega_1 & J \\ J & \omega_2 \end{pmatrix}}_{\mathbf{M}} \begin{pmatrix} a_1 \\ a_2 \end{pmatrix}.$$

Diagonalising the  $2 \times 2$  Hermitian matrix  $\mathbf{M}$  one finds the normal-mode (super-mode) eigenfrequencies

$$\omega_\pm = \frac{\omega_1 + \omega_2}{2} \pm \sqrt{J^2 + \left(\frac{\omega_1 - \omega_2}{2}\right)^2}, \quad (\text{II.53})$$

and introduces a mixing angle  $\theta$  via

$$\tan 2\theta = \frac{2J}{\omega_2 - \omega_1}, \quad 0 < \theta < \pi/2.$$

The corresponding canonical operators

$$A_+ = \cos \theta a_1 + \sin \theta a_2, \quad A_- = -\sin \theta a_1 + \cos \theta a_2,$$

obey  $[A_\mu, A_\nu^\dagger] = \delta_{\mu\nu}$  and bring the Hamiltonian to the diagonal form

$$H = \hbar\omega_+ A_+^\dagger A_+ + \hbar\omega_- A_-^\dagger A_-,$$

revealing two independent harmonic oscillators whose frequency splitting  $\omega_+ - \omega_- = 2\sqrt{J^2 + [(\omega_1 - \omega_2)/2]^2}$  interpolates smoothly between the strong-coupling limit ( $\omega_1 \approx \omega_2$ ) and the large-detuning regime where each cavity mode retains its individuality and the admixture of its neighbour is suppressed by the small parameter  $J/|\omega_2 - \omega_1| \ll 1$ .

# Chapter III

# Experimental Methods

This chapter will cover the experimental methods used in the development of optomechanical systems, focusing on the generation of squeezed light and the techniques for optical locking and quadrature measurement. The methods are designed to enhance the sensitivity of measurements in quantum optics and optomechanics.

## Contents

---

<b>III.1 Optical Locking Techniques with PyRPL . . . . .</b>	<b>62</b>
III.1.1 Proportion-Integral (PI) Controllers . . . . .	62
III.1.2 Temperature Locks . . . . .	64
III.1.3 Optical paths Locks - Dither Locks . . . . .	64
III.1.4 Side of Fringe Locks . . . . .	65
III.1.5 Pound-Drever-Hall Locks . . . . .	65
III.1.6 Offset frequency Locks . . . . .	66
III.1.7 Coherent Sideband Locks . . . . .	66
III.1.8 PyRPL Control Implementation . . . . .	66
<b>III.2 Optical Cavities and Squeezed Light Generation . . . . .</b>	<b>66</b>
III.2.1 Cavity Types and Alignement Procedures . . . . .	67
III.2.2 Bowtie-type Optical Parametric Oscillator (OPO) . . . . .	67
III.2.3 Phase Matching and Nonlinear Crystals . . . . .	67
III.2.4 Filter Cavities for Squeezing Rotation . . . . .	67
<b>III.3 Quadrature Measurement Techniques . . . . .</b>	<b>67</b>
III.3.1 Direct Detection with Photodiodes . . . . .	67
III.3.2 Balanced Homodyne Detection . . . . .	67
III.3.3 Local Oscillator Design and Control . . . . .	67

---

### III.1 Optical Locking Techniques with PyRPL

A central aspect of the experimental setups is the ability to stabilize various optical features. In this work, it is the case for the relative phase between two optical paths, keeping optical cavities on resonance, or fixing the detuning between a master and a slave laser.

This section will cover the locking techniques used in this work, from basic Michelson-type locking to more advanced Pound-Drever-Hall techniques and phase-locked loops. The implementation of these techniques using the in-house library PyRPL is presented.

#### III.1.1 Proportion-Integral (PI) Controllers

Proportional-Integral (PI) controllers are widely used in quantum optics experiments to stabilize critical parameters such as cavity length, laser frequency, and optical phase. To this end, one needs to extract an error signal  $\epsilon(t)$  that quantifies the deviation from a desired setpoint, such as a target temperature, phase difference or cavity resonance. It is typically expressed as the difference between a measured signal and its reference value:

$$\epsilon(t) = s_{\text{meas}}(t) - s_{\text{ref}},$$

where  $s_{\text{meas}}(t)$  denotes the physical quantity monitored in the experiment (e.g., reflected intensity or interferometric signal), and  $s_{\text{ref}}$  is the target value corresponding to the lock point.

For effective feedback stabilization, the error signal must satisfy several essential criteria:

- **High SNR:** Near the setpoint,  $\epsilon(t)$  should exhibit a high SNR to ensure robust locking and minimize the influence of technical and electronic noise.
- **Linearity and antisymmetry:** The error signal should be linear and antisymmetric in a neighborhood of the operating point. Small deviations from the setpoint should produce a proportional response in  $\epsilon(t)$ , with opposite signs for deviations of opposite direction.
- **Monotonicity and uniqueness:** The slope  $\partial\epsilon/\partial x$ , where  $x$  denotes the control parameter (e.g., cavity length or laser frequency), should be monotonic and unambiguous near the lock point to avoid multiple equilibrium points and ensure stable locking behavior.
- **Steep slope near the setpoint:** A steeper slope improves sensitivity to small deviations and enhances lock accuracy, although it must be balanced against potential noise amplification.

- **Bandwidth compatibility:** The spectral content of  $\epsilon(t)$  must be compatible with the bandwidth of the actuator and the dynamics of the system. For example, in the case of a piezoelectric transducer, which acts as a low-pass mechanical element, the error signal high-frequency components won't be compensated by the actuator.

The PI controller computes the feedback signal  $u(t)$  from the error signal  $\epsilon(t)$  according to:

$$u(t) = K_P \epsilon(t) + K_I \int_0^t \epsilon(\tau) d\tau \quad (\text{III.1})$$

where  $K_P$  and  $K_I$  are the proportional and integral gains, respectively. The proportional term  $K_P \epsilon(t)$  responds to the current error and primarily acts on mid-frequency deviations, enabling rapid corrections. The integral term  $K_I \int \epsilon(\tau) d\tau$  accumulates past errors and is most effective at low frequencies, helping to eliminate long-term drifts and steady-state offsets.

In classical control theory, PID (Proportional-Integral-Derivative) controllers are designed to stabilize dynamic systems by combining three terms: a proportional term for immediate response, an integral term to eliminate steady-state error, and a derivative term that anticipates future error based on the rate of change. However, in practical experimental setups—particularly in quantum optics—PI control (Proportional-Integral) is typically sufficient and even preferable to full PID control. The derivative term, which acts predominantly at high frequencies, is generally unnecessary and can be counterproductive. This is because the feedback actuator is often a piezoelectric transducer, which exhibits non-zero capacitance. Combined with the finite output impedance of the control electronics, this forms a natural low-pass filter that significantly attenuates high-frequency components of the feedback signal. As a result, any derivative term—which primarily targets high-frequency correction—would be both ineffective due to this filtering and potentially harmful by injecting high-frequency noise into the loop.

Therefore, PI control offers a balanced and robust approach: the integral term suppresses low-frequency drifts (typically below a few Hz to tens of Hz), the proportional term corrects intermediate-frequency deviations (up to a few kHz), and high-frequency components (above the mechanical resonance or actuation bandwidth) are naturally filtered out and deliberately left uncorrected. This allows for stable feedback while preserving high-frequency signals—such as thermal noise or mechanical sidebands—which carry essential physical information for analysis and measurement.

### III.1.2 Temperature Locks

A first example of a PI lock used in this work is the temperature lock, which is used to stabilize the temperature of non linear crystals embedded inside optical cavities. The error signal is derived from a temperature sensor, such as a thermistor, which measures the temperature of the crystal and simply written as:

$$\epsilon(\Delta T) \propto \Delta T \quad (\text{III.1})$$

where  $\Delta T = T_{\text{meas}} - T_{\text{set}}$ . The error signal is then fed into a PI controller, which adjusts the heating element, a peltier module in our case, to maintain the desired temperature setpoint.

The temperature lock is crucial for maintaining the phase matching conditions in nonlinear optical processes (developed in the next section), such as second-harmonic generation or optical parametric oscillation, where the efficiency of frequency conversion depends sensitively on the crystal temperature. By stabilizing the temperature, we ensure that the nonlinear interactions remain optimal, leading to consistent and reproducible results in experiments involving squeezed light generation or other nonlinear optical phenomena.

### III.1.3 Optical paths Locks - Dither Locks

Controlling the relative path length between two arms of an interferometer is a fundamental technique in quantum optics. The basic idea is to use the interference of light from two paths to lock the phase difference between them. Although not being the same experimental setups, Michelson interferometers, Mach-Zhender interferometers, and Local Oscillator stabilization error signals fall in the same category as they are derived from the same principle. Namely, the error signal is proportional to the sine of the phase difference between the two arms:

$$\epsilon(\Delta\phi) \propto \sin(\Delta\phi) \simeq \Delta\phi \quad (\text{III.2})$$

where  $\Delta\phi = \phi_a - \phi_b$  is the phase difference between the two optical paths. Analogically, we would need to add an adjustable voltage offset, as to be able to tune the error signal to zero at the desired phase difference, before seeding this error signal to the PI block. Digitally, this is performed by adding a constant offset to the error signal, which can be adjusted to set the desired phase difference.

In practice, this is implemented by mounting a mirror on which one of the arms is reflected, and then using a piezoelectric transducer to control the position of the mirror, hence modulating the relative phase between the two optical paths. The piezo is then feedback controlled

through a PI loop, which adjusts the voltage applied to the piezo to set the error signal to 0.

## FIGURE

### III.1.4 Side of Fringe Locks

$$\epsilon(\Delta\omega) \propto \Delta\omega \quad (\text{III.3})$$

### III.1.5 Pound-Drever-Hall Locks

Another key technique extensively used in this work is the *Pound-Drever-Hall* (PDH) method, a high-sensitivity scheme for stabilizing either the cavity length to a fluctuating laser frequency, or vice versa. The method relies on imposing phase modulation sidebands on the laser field, typically using an electro-optic modulator (EOM), and using these sidebands as phase-stable references. Because they lie far outside the cavity linewidth ( $\Omega_{\text{mod}} \gg \kappa$ ), the sidebands are reflected nearly unchanged:  $r(\omega_\ell \pm \Omega_{\text{mod}}) \approx 1$ . In contrast, the carrier field near resonance acquires a frequency-dependent phase shift upon reflection, captured by the complex cavity reflection coefficient  $r_c(\delta)$ . The PDH error signal is obtained by detecting the reflected beam and demodulating the photocurrent at the modulation frequency, isolating the beat terms between carrier and sidebands. The resulting signal is proportional to the *imaginary part* of  $r_c(\delta)$ , which varies antisymmetrically with detuning and provides a zero-crossing error signal ideal for linear feedback. The error signal near resonance is then given by

$$\epsilon(\Delta\omega) \propto \Im(r_c(\Delta\omega)) \simeq \Delta\omega \quad (\text{III.4})$$

This imaginary component encodes the rapid phase dispersion near resonance that allows the system to discriminate the sign and magnitude of frequency deviations. In contrast, the real part of  $r_c(\delta)$ , being symmetric around resonance, does not yield a usable error signal.

The *demodulation phase* plays a critical role in selecting the appropriate quadrature of the signal for feedback. Since the beat signal between the carrier and sidebands has both in-phase (cosine) and quadrature (sine) components, choosing the correct demodulation phase ensures that the extracted error signal aligns with the imaginary part of the reflection coefficient. A misaligned demodulation phase can lead to mixing of the symmetric (real) part into the error signal, thereby reducing sensitivity and introducing offset or distortion near the lock point. In practice, the demodulation phase is optimized empirically—either via a variable phase shifter in the electronic demodulation path or by adjusting the physical delay in the reference oscillator—to maximize the slope of the error signal at zero-crossing, corresponding to pure detection of the dispersive component.

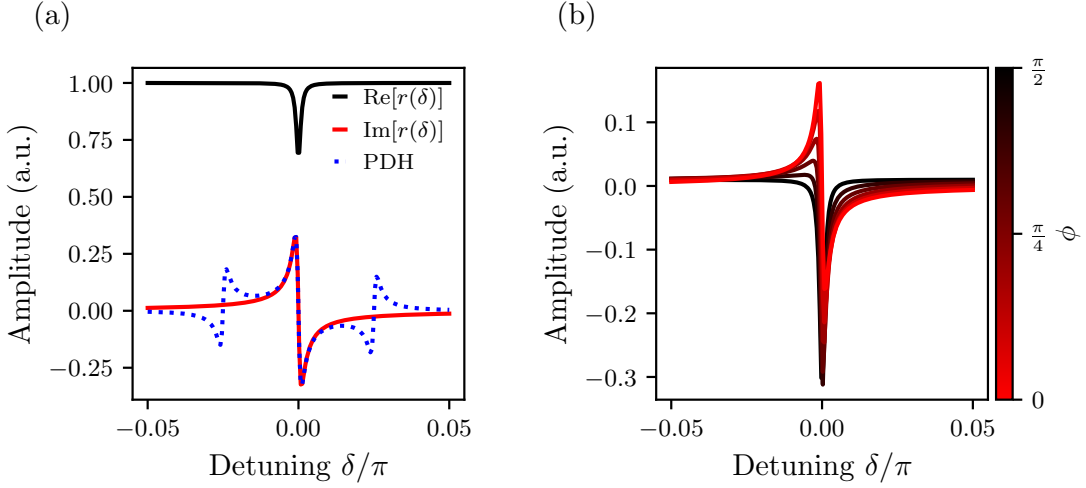


Fig. III.1 *Schematic of the Pound-Drever-Hall (PDH) locking technique.* The laser passes through an electro-optic modulator (EOM) generating phase modulation sidebands. The modulated beam is incident on the optical cavity, and the reflected light is detected by a photodiode (PD). The photocurrent is demodulated at the modulation frequency to produce the PDH error signal, which is fed to a PI controller driving the cavity actuator (e.g., piezo). Key components are labeled: EOM (electro-optic modulator), PD (photodiode), LO (local oscillator for demodulation), and PI (proportional-integral controller).

### III.1.6 Offset frequency Locks

$$\epsilon(\Delta\omega_{\text{beat}}) \propto \Delta\omega_{\text{beat}} \quad (\text{III.5})$$

### III.1.7 Coherent Sideband Locks

### III.1.8 PyRPL Control Implementation

## III.2 Optical Cavities and Squeezed Light Generation

Maybe I need to add a section on the theory of squeezed light generation, but for now I will just focus on the experimental methods.

**III.2.1 Cavity Types and Alignment Procedures****III.2.2 Bowtie-type Optical Parametric Oscillator (OPO)****III.2.3 Phase Matching and Nonlinear Crystals****III.2.4 Filter Cavities for Squeezing Rotation****III.3 Quadrature Measurement Techniques****III.3.1 Direct Detection with Photodiodes****III.3.2 Balanced Homodyne Detection****III.3.3 Local Oscillator Design and Control**



## Chapter IV

# Experiments: Optomechanics

This chapter will cover the experimental methods used in the development of optomechanical three-mirror cavity systems, focusing on the design, fabrication, and characterization of mechanical resonators within optical cavities. The methods are designed to enhance the sensitivity of measurements in quantum optics and optomechanics.

### Contents

---

<b>IV.1 System Description and Setup . . . . .</b>	<b>70</b>
IV.1.1 Previous LKB work and Motivation . . . . .	70
IV.1.2 Specifications and Design . . . . .	71
IV.1.3 Flexure Actuation . . . . .	74
IV.1.4 Experimental Setup . . . . .	76
IV.1.5 Alignment Procedures . . . . .	78
<b>IV.2 Experimental Characterization . . . . .</b>	<b>79</b>
IV.2.1 Cavity Characterization . . . . .	79
IV.2.2 Locking Techniques and Stability . . . . .	84
IV.2.3 Optical Ringdowns and Loss Measurements . . . . .	84
IV.2.4 Mechanical Resonator Characterization . . . . .	84
IV.2.5 Bistability . . . . .	84
<b>IV.3 Design of an Optomechanical Fibered Cavity . . . . .</b>	<b>84</b>
IV.3.1 Design considerations . . . . .	84

---

Over the past two decades, optomechanical systems have greatly benefited from advancements in optical coating technologies, enabling the realization of high-finesse cavities ( $\mathcal{F} > 10^5$ )[?]. Simultaneously, progresses in micro/nanofabrication allowed the making of mechanical structures with high  $Q$  factors ( $> 10^6$ )[?]. Despite these achievements, a significant challenge remained: fabricating mechanical elements that possess both high  $Q$  and high reflectivity, as optical, mechanical and thermal effects often degrade system performance and hinder ultra-sensitive measurements[?].

## IV.1 System Description and Setup

### IV.1.1 Previous LKB work and Motivation

Previous optomechanics experiments at LKB have primarily utilized Fabry–Pérot cavities with two mirrors, where the end mirror of the cavity was typically a HR mirror deposited on top of a mechanical structure featuring a mechanical mode of interest [?].

- Over Aurélien’s and Leonard’s PhD works, the group in collaboration with ONERA developed a platform based on a 1-mm-thick quartz micropillar with an effective mass of  $33 \mu\text{g}$ . The structure supports a fundamental compression mode oscillating at 3.6 MHz, with a mode shape as shown in Fig. ???. Using a dry-film photoresist technique, a  $100 \mu\text{m}$  diameter high-reflectivity mirror was deposited on one end of the pillar. Careful design of the suspension has yielded mechanical quality factors up to  $3 \times 10^6$  at room temperature and up to  $7 \times 10^7$  below 1 K. When integrated into a  $50 \mu\text{m}$ -long Fabry–Pérot cavity with a custom-fabricated coupling mirror, finesses exceeding  $10^5$  were achieved. Importantly, this compact cavity remains robust against vibrations of the dilution refrigerator and maintains alignment during cooldown, thereby providing a stable platform to study optomechanical effects in the intermediate mass regime.  
**limitations and why it didnt work**
- Then over Rémi’s and Michael’s PhD, another resonator was developed in collaboration with Francesco Marin’s team, based on a suspended silicon disk. The device operates in a balanced mode, where the central disk vibrates in opposition to four surrounding counterweights. By adjusting the geometry, the resonance frequency was increased to 280 kHz, corresponding to an effective mass of about  $110 \mu\text{g}$ , bringing the system closer to the micropillar parameters. A HR mirror was then deposited on top using the same technique as the micropillar. Finesse of about  $\sim 50000$  were then reached. At cryogenic temperature, optimized designs reached mechanical quality factors on the order of  $1.2 \times 10^6$ .**limitations and why it didnt work**

Although the systems ended up being limited by various factors mentioned above (optical, mechanical and thermal effects) [?], the parts designed over the years did feature a high level of passive stability as well as good thermalization properties. A pivotal solution, introduced by Regal, Kimble, Harris, and collaborators[?, ?], was to decouple these requirements by embedding a high- $Q$  mechanical resonator within a high-finesse optical cavity, using the optical field to probe and control the resonator's dynamics.

#### IV.1.2 Specifications and Design

It was then decided to build on this design and extend it to a three-mirror cavity in a MATE configuration to benefit from this large linear and tunable coupling range as detailed in the previous chapter. That is the work Michael and myself undertook during my M2 internship and the following years of my PhD. This new three mirror cavity then needed to fulfill various requirements:

- **High Finesse:** input and back mirrors should both have high reflectivities, with low extra losses such as scattering, absorption, etc ...[?]
- **High  $Q$  factor:** the middle mirror i.e. the mechanical resonator, should feature a high  $Q$  factor, ideally above  $10^6$ , in order to ensure a good sensitivity to radiation pressure forces[?]
- **Optical alignment:** the cavity should be designed to allow for easy optical alignment, with the ability to mode match the setup fairly easily.
- **Dynamical range:** both input and output mirrors should be mounted on piezoelectric actuators, allowing for a dynamic range of at least few microns to scan few FSRs. The piezo actuators should also be able to provide a good bandwidth, ideally above 100 kHz, as well as a sub-nanometer resolution to ensure a good control of the cavity length[?].
- **Compactness & Stability :** the entire assembly should be compact, with a high level of passive stability, yet without mechanically low pass filtering the piezo actuators motion during the locking.
- **Vacuum and Cryogenic compatibility:** the cavity should be vacuum compatible, and the mirrors should be thermally anchored to the vacuum chamber in order to ensure a good thermalization of the system. Same holds for the cryogenic compatibility, although no test could be performed during this thesis. The cavity was nonetheless designed to be compatible with cryogenic operation.

### High Finesse

Low loss mirrors were produced by **Jérôme DEGALLAIX** and **David HOFMAN** at the *Laboratoire des Matériaux Avancés* (LMA, Lyon) using ion-beam-sputtered (IBS) Bragg stacks made of  $\text{Ta}_2\text{O}_5$  (high index,  $n \approx 2.09$ ) and  $\text{SiO}_2$  (low index,  $n \approx 1.46$ )<sup>[?, ?]</sup>.

The coatings were deposited in the LMA's *Veeco SPECTOR* chambers and subsequently annealed at  $500^\circ\text{C}$  for 10 hours to minimise both optical (absorption) and mechanical losses, following the recipe of Amato *et al.* [?]. <sup>1</sup>

We supplied the LMA with a batch of substrates with various radii of curvature to explore different cavity geometries. The requested specifications are summarized in the table below. The total round-trip scatter and absorption losses are usually below 20 ppm, in agreement with the measurements reported (absorption  $\sim 0.7$  ppm, scattering  $\sim 10$  ppm) in Ref. [?].

Substrate type	Laseroptik ID	$R$	Front-side HR $T$	Back-side AR
Plane	S-00798	$\infty$ (plane)	$20 \pm 4$ ppm	$R \lesssim 100$ ppm
Plano-concave	S-00128	-25 mm	$100, 50 \pm 10$ ppm	$R \lesssim 100$ ppm
Plano-concave	S-00127	-15 mm	$100, 50 \pm 10$ ppm	$R \lesssim 100$ ppm
Plano-concave	S-00126	-10 mm	$100, 50 \pm 10$ ppm	$R \lesssim 100$ ppm

Table IV.1: Specifications of supplied Laseroptik substrates for different cavity geometries.

The quarter-wave design is centred at  $\lambda = 1064$  nm for normal incidence. After annealing, the measured mechanical loss angle of the  $\text{TiO}_2:\text{Ta}_2\text{O}_5/\text{SiO}_2$  stack is  $\phi < 4 \times 10^{-4}$  at 1 kHz [link to mechanical damping needed](#), supporting cavity finesse in the range  $200\,000 - 500\,000$  before excess scatter or absorption dominates[?].

### High $Q$ factor

The middle mirror is a commercially-available stoichiometric silicon-nitride ( $\text{Si}_3\text{N}_4$ ) membrane supplied by Norcada® (NX10050AS)<sup>[?, ?]</sup>. It consists of a  $l \times l = 500 \mu\text{m} \times 500 \mu\text{m}$ , 50 nm-thick  $\text{Si}_3\text{N}_4$  film suspended in a  $10 \text{ mm} \times 10 \text{ mm}$ ,  $200 \mu\text{m}$ -thick silicon frame and is marketed specifically for *high-Q* resonator applications. Because stoichiometric LPCVD  $\text{Si}_3\text{N}_4$  is under high intrinsic tensile stress ( $\sigma \approx 0.9$  GPa), the square drum supports MHz-frequency modes with low mechanical loss[?].

- **Room temperature.** Measurements on nominally identical Norcada membranes report quality factors  $Q \sim 5 \times 10^6$  at  $\approx 1$  MHz in  $< 10^{-6}$  mbar vacuum [?, ?].
- **Cryogenic operation.** Cooling to  $T \lesssim 300$  mK reduces internal friction by an order of magnitude, with  $Q > 10^7$  routinely observed [?].

---

<sup>1</sup>Identical optics are used for the Advanced LIGO, Advanced Virgo and KAGRA interferometers[?].

The membrane's high stress, thin-film nature and dielectric composition make it fully compatible with ultra-high-vacuum environments and repeated cryogenic cycling, while introducing (a priori) negligible optical loss in the cavity. The expected mechanical mode structure can be derived from

$$f_{n,m} = \sqrt{\frac{\sigma}{4\rho l^2}(n^2 + m^2)} \quad (\text{IV.1})$$

with  $\rho = 2.7 \text{ g/cm}^3$  the film mass density and  $n, m$  the mode indices. The fundamental mode  $(n, m) = (1, 1)$  is expected at  $f_{1,1} \approx 816 \text{ kHz}$ , with the two higher order modes  $(1, 2)$  and  $(2, 1)$  degenerate at  $f_{1,2} \approx f_{2,1} \approx 1.29 \text{ MHz}$ .

### Optical alignment

The cavity is designed to be compatible with the Thorlabs® cage system. The input mirror is mounted on a 3 axis cage mount, allowing for easy alignment of the input mirror with respect to the cavity optical axis. Both the resonator and the back mirror are embedded within a custom-made holder, which is itself integrated into the cage system. The relative tilt between the resonator and the back mirror is adjusted using a set of 3 screws with a very fine thread, allowing for a fine alignment of the parallelism of the back cavity. The alignment procedure is detailed in section ??.

### Dynamical range

The input mirror is glued to a PI Ceramic® P-016.00H ring-stack piezoelectric actuator using vacuum epoxy (Torr Seal®). Driven from 0 to  $+1000 \text{ V}$  it provides a longitudinal stroke of  $5 \mu\text{m}$ , a blocking force of  $2.9 \text{ kN}$ , as well as an unloaded resonance of  $144 \text{ kHz}$ , making it suitable for fast, low-noise cavity-length control.

The end-mirror-membrane assembly is mounted on a custom holder actuated by three PD080.31 piezo chips arranged mechanically in series. Each chip yields  $2 \mu\text{m}$  of travel over a drive range of  $-20$  to  $+100 \text{ V}$ ; the triple stack therefore supplies roughly  $6 \mu\text{m}$  of coarse tuning while preserving high stiffness and sub-microsecond response. The effective range is lower than this owing to the fact the piezo is constrained within the holder. Furthermore, one should not constrain the piezo to much to avoid damaging it: it happened that the assembly was too tightly screwed such that it ended up fracturing the piezo pushing against the back mirror holder.

Combining the  $5 \mu\text{m}$  stroke of the front P-016.00H with the  $6 \mu\text{m}$  range of the rear triple stack provides an overall cavity-length adjustment sufficient to scan few FSRs, as well as to tune the membrane position over a full wavelength, thus accessing allowing exploration of the three mirror cavity physics.

### Compactness & Stability

The entire assembly is built as a cage system using standard Thorlabs® cage parts, allowing for a compact and stable assembly. The cage system also allows for (relatively) easy alignment of the mirrors, as well as easy access to the piezo actuators.

### Vacuum and Cryogenic compatibility

The back cavity composed of the back mirror and the middle mirror is embedded inside an Oxygen Free Copper (OFC) assembly with a circular geometry, eventually mitigating for transverse misalignment issues when going to cryogenic temperatures, the constraints compensating themselves radially with respect to the symmetry axis of the cavity assembly[?]. Furthermore, the screws used to hold the assembly together are made of brass with a thermal expansion coefficient lower than that of the OFC, tightening up the cavity when reaching cryogenic temperatures. Thorlabs cage parts are compatible with moderate vacuum operation down to  $\sim 10^{-7} \text{ mbar}$  if properly degreased and ultrasound cleant, but a custom cryocompatible system to hold the input mirror would be needed for operation at cryogenic temperatures.

The initial design of the cavity was made using Autodesk Fusion 360, allowing for a detailed 3D model of the entire assembly, including the piezo actuators, the mirrors and the cage system. The design was then exported to a STEP file format, which was used to manufacture the parts using a 3 axis CNC milling machine and a digital lathe. The pieces were machined by **Carounagarane DORE** and **Gael COUPIN** at the LKB mechanical workshop with  $100\mu\text{m}$  tolerance. A detailed view of the cavity design and assembly is shown in Fig. IV.1.

#### IV.1.3 Flexure Actuation

One specificity of the MATE system is that the back cavity is significantly shorter than the front cavity, which would require high precision in both the machining of the copper pieces and the positioning of the resonator. In our case, we aim at a centimetric cavity which would require to position the membrane at roughly hundreds of microns from the back mirror, and parallel to the back mirror. Moving the membrane independently from the back mirror while maintaining a controllable tilt between both planes is therefore challenging.

A smart workaround was introduced by Jack Sankey and its group [?], where the authors introduced a flexure-tuned MATE system. The key innovation lies in actuating the membrane position by flexing its supporting silicon frame rather than translating the entire mount. This is done by mounting the back cavity in a semi-monolithic fashion, and 'locking'

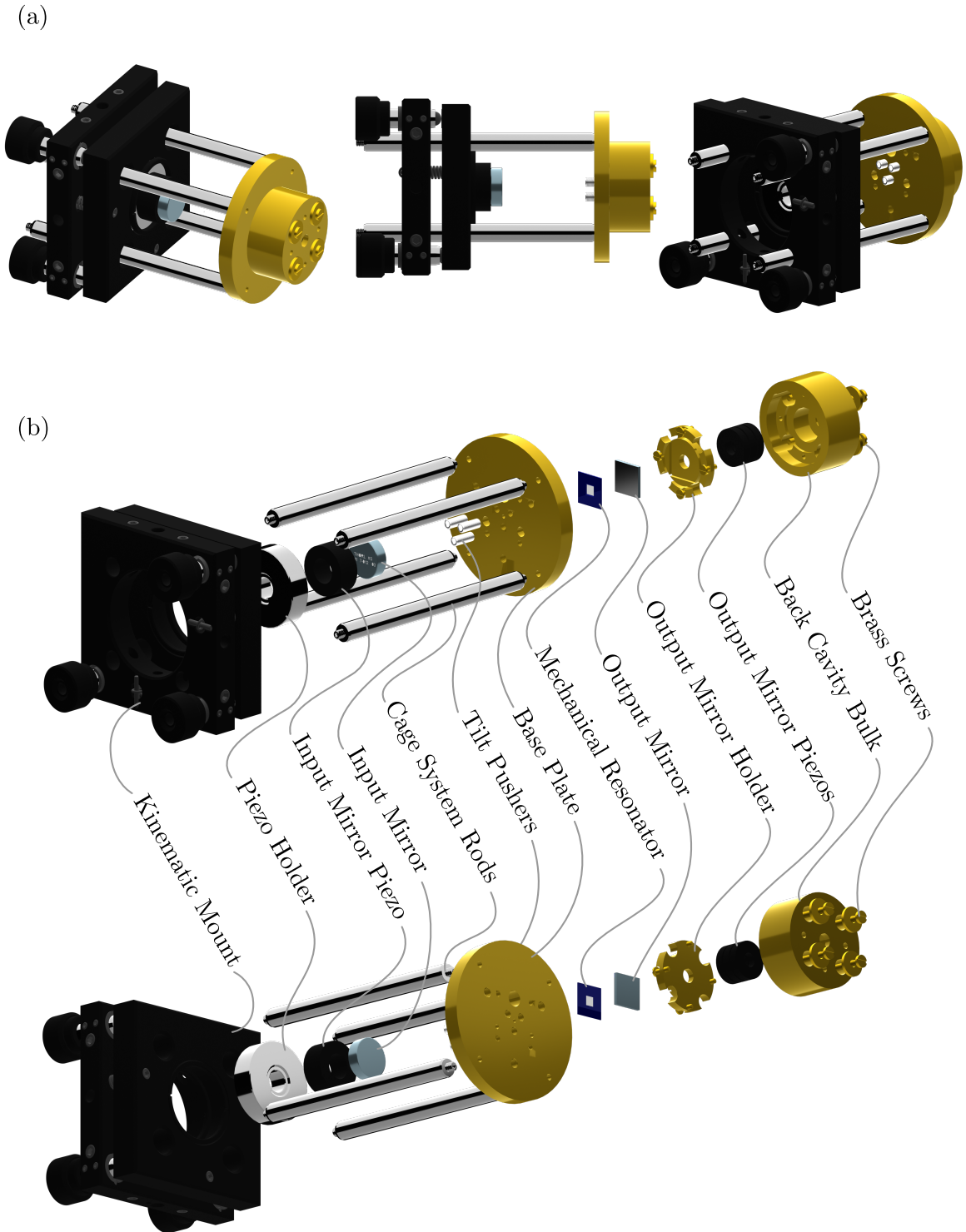


Fig. IV.1 Cavity design and assembly. (a) The figure shows the overall assembly of the MATE system from various views, highlighting the integration of the high-finesse mirrors, the membrane resonator embedded inside the back cavity copper assembly held to the input mirror Thorlabs holder through a cage system.(b) The exploded view details the arrangement of the mechanical and optical components, illustrating the modular design that facilitates alignment, stability, and compatibility with vacuum environments.

the silicon frame of the membrane using three screws with a fine thread, allowing for a fine adjustment of the angle of the membrane plane with respect to the back mirror plane. The piezos pushing on the back of the assembly then force the silicon frame constrained by the screws to bend, thus displacing the membrane with respect to the back mirror, as shown in Fig. IV.2. This approach preserves the cavity alignment for gentle flexures, while enabling continuous and wide-range tuning of both the membrane displacement and tilt.

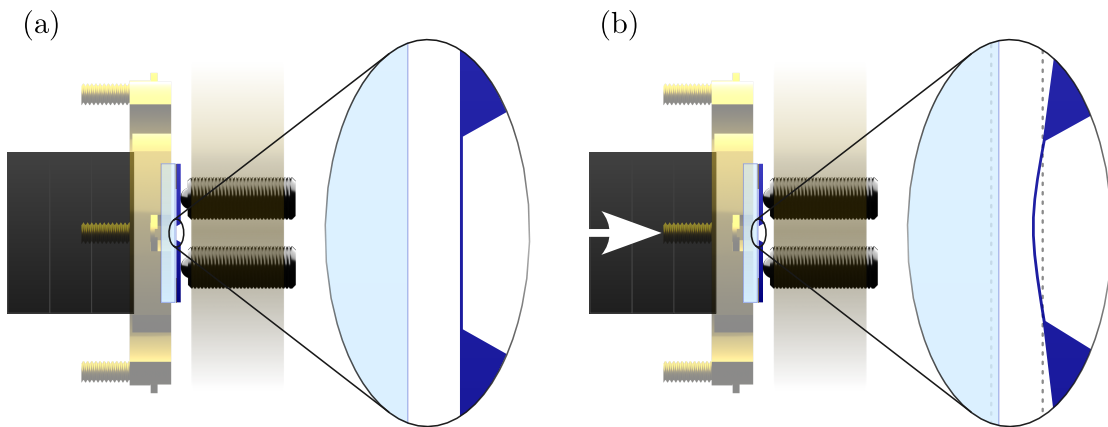


Fig. IV.2 Cavity design and assembly. (a) In this configuration (no voltage applied to the piezos), the screws are used to align the membrane plane with respect to the back mirror plane, ensuring a good parallelism between both planes. (b) Flexure tuning of the membrane position. When a voltage is applied to the piezos, they push on the back of the assembly, forcing the silicon frame to bend, thus displacing the membrane with respect to the back mirror. The two dashed lines show the initial positions of the back mirror and the membrane. This push shortens the overall cavity length (i.e. increasing the overall system's frequency), as well as the relative distance between the mirror and the membrane (i.e. changing the optomechanical coupling).

#### IV.1.4 Experimental Setup

The assembly is now to be integrated into the optical setup shown in Fig. IV.3. The source laser is a 1064nm Nd:YAG laser (Coherent Mephisto). We did not require the full optical power delivered by the laser, so a short optical path not detailed here splits the laser in 3 arms to eventually fiber couple some laser power and bring it to other experiments that would need 1064nm laser light.

The optical path then consists of :

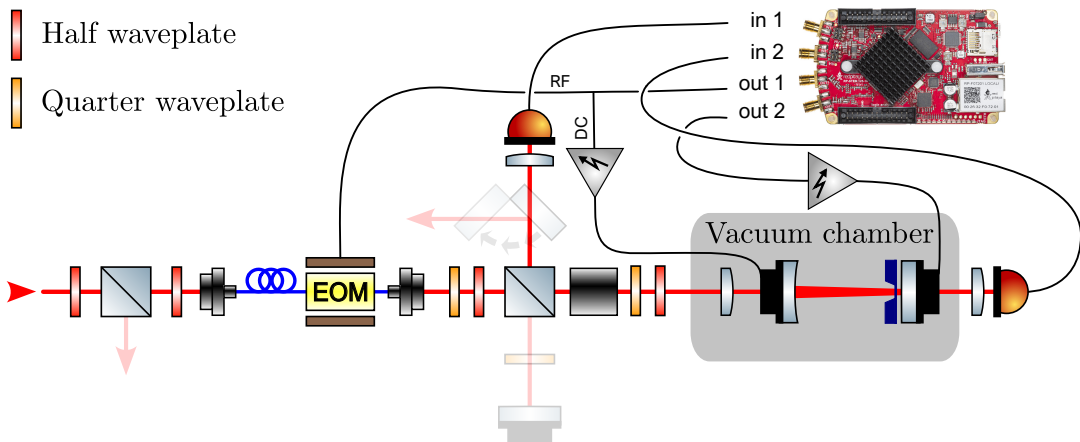


Fig. IV.3

- a first half waveplate and a beam splitter to adjust the total power injected into the experimental setup,
- a fibered electro-optics phase modulator (EOM Photline NIR-MPX-LN-10) to generate sidebands for the PDH locking of the cavity. It is polarization matched by using a fibered polarization controller to avoid Residual Amplitude Modulation noise (RAM) at the output (three blue circles on the optical layout).
- a fiber coupler to go from a guided optical mode to a free space optical mode, with a the coupler adjusted such that the outputted beam is collimated and has a waist of about 1mm,
- a quarter waveplate to compensate for ellipticity of the output beam polarization, then a half waveplate and a beam splitter to adjust the powers injected into the cavity path and the prospective LO path, respectively,
- on the cavity path, a faraday rotator to ensure the cavity reflected beam to be deflected to an output port and not back into the fiber
- a lens to mode match the laser input mode to the cavity mode, with a focal length of 40 to 60mm depending on the input mirror radii of curvature. This lens is mounted on a x-y cage system translation mount, and is mounted inside the vacuum chamber that features AR coated windows to allow for optical access yet minimal parasite reflections.
- the cavity itself.
- two photodiodes (Thorlabs ???) to detect the reflected beam and the transmitted beam, respectively, with 40mm focal length lenses to focus the beam onto the photodiodes.

The optical path was designed to be as modular as possible, allowing for easy replacement of the components if needed, as well as additions of optical elements. For this reason, it features two faint additional optical paths as seen on Fig. IV.3, one for a prospective LO, and another to deflect the reflected beam to a Homodyne Detection setup using a flip mirror. Polarization optics would also need to be added on the Homodyne Detection path to mix the LO and the reflected beam, but this was not done during this thesis.

#### IV.1.5 Alignment Procedures

The optical setup is now to be aligned as to ensure a good mode matching between the laser input mode and the cavity mode. The steps are as follows, and the associated diagrams are shown in Fig. IV.9:

- **Step 1** (Fig. IV.9(a)): we position an iris diaphragm before our two injection mirrors mounted on  $(\theta_x, \theta_y)$  kinematic mounts. We then adjust the tilt of both mirrors i.e. *beam-walking*, such that the reflected beam is centered on the iris diaphragm: this is done by maximising the reflected signal on the reflection photodiode. This ensures the beam reflected by the output mirror (HR mirror) is at normal incidence. In a second time we tune the plane of the resonator using the three screws of the assembly. We monitor the Fizeau fringes in transmission with a camera (Allied Vision Alvium), and adjust the tilt such that no fringes are to be seen.
- **Step 2** (Fig. IV.9(b)): we then place the focusing lens in the optical path, and adjust its position such that we recover maximal power on the reflection photodiode. This lens is mounted on the (x-y) cage system translation mount, and positioned at a distance from the back mirror fixed by the cavity mode matching requirements (ref chap theory). The lens is then fixed in place using the cage system screws.
- **Step 3** (Fig. IV.9(c)): we add the input mirror on a  $(\theta_x, \theta_y)$  cage system mount, and adjust its position to get an input beam normal to the tangent of the concave mirror curvature. This is also done maximising the reflected power on the reflection photodiode. The mount (and thus the mirror) was also positioned at the appropriate distance from the back mirror to ensure optimal mode matching.
- **Step 4** (Fig. IV.9(d)): We scan the cavity length using the piezo actuator mounted on the input mirror, and monitor the cavity resonances using both the reflected and transmitted photodiodes. We finally fine tune the mode match by *beam-walking* the two injection mirrors. We can also play with the collimating lens at the fiber coupler (not shown on the diagram) as to fine tune for longitudinal mode matching. The cavity is now aligned and ready for operation.

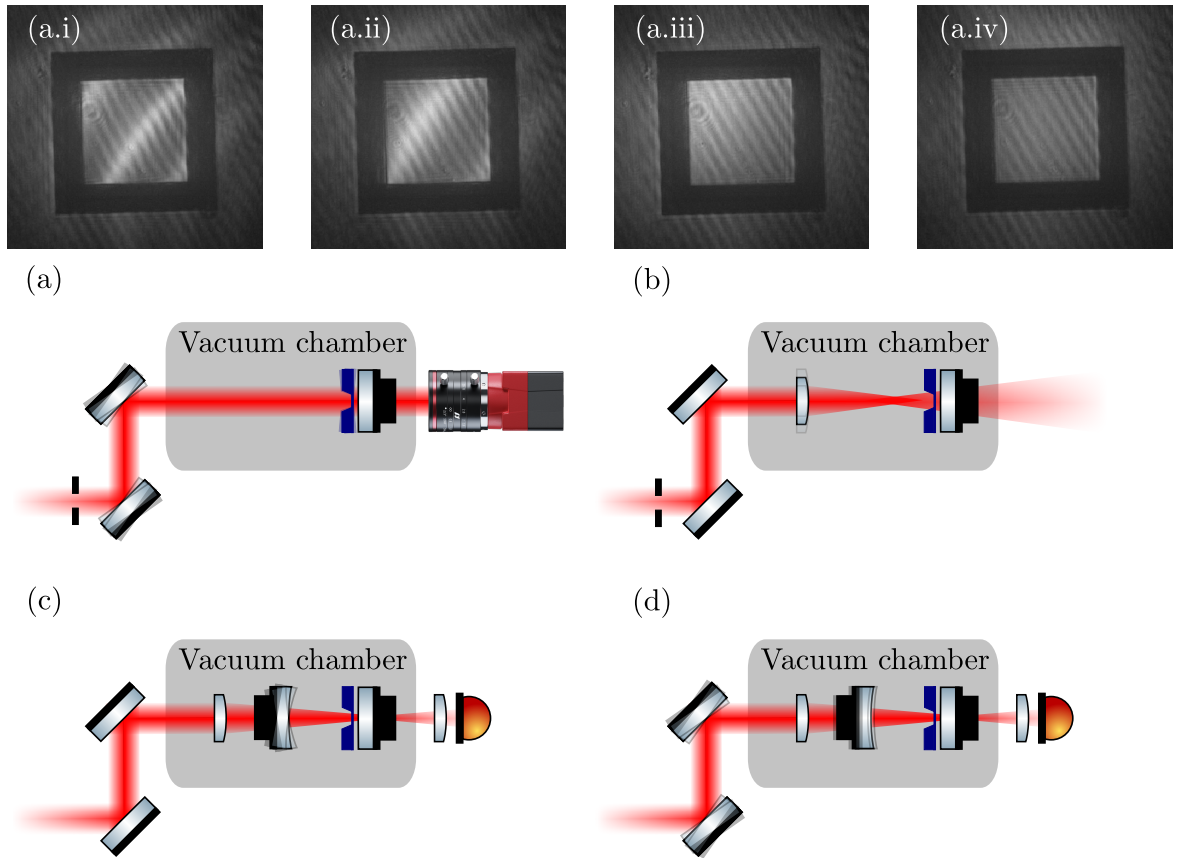


Fig. IV.4 Set up alignment procedure. (a) to (d) show the steps to align the cavity with respect to the optical path (detailed in the main text). The (a.i) to (a.iv) show what is seen on the camera for four different tilt positions where (a.iv) displays a 'good' tilt alignment: no visible fringes except for the dim fringes of the camera setup. These dim fringes are present when the beam is a normal incidence with the back mirror (use of the iris) and are believed to be interferences arising from reflections inside the camera objective as they are seen whatever the plane of focus is.

## IV.2 Experimental Characterization

### IV.2.1 Cavity Characterization

Many trial and errors for such a MATE cavity were realised over this thesis. Their main characteristics are summarized in table

, but the cleaner data were obtained with a cavity made of an input concave mirror of radius of curvature  $R = 25\text{mm}$ , input and output mirrors with requested transmittivities  $t_1 = 100\text{ppm}$  and  $t_2 = 20\text{ppm}$ , and a cavity length of  $L = 22\text{mm}$ . Hence, the theoretical finesse would be  $\sim 52400$ . Another cavity of length 17mm was also mounted at the start of

the project but only gross preliminary results were extracted from it. It however did feature finesse 10 times higher than the one whose result are presented here, and these results are shown in the annexe ??.

Once the cavity is aligned, we can scan the cavity length by driving the front mirror piezo with a triangular or a sine wave voltage. This signal is first amplified using a high voltage amplifier made by the LKB electronic workshop, which can deliver up to 1000V. The output impedance of the amplifier is a standard 50 Ohms, but the piezo in parallel at the end of the line with capacitance of about 15 nF low pass filters the signal at  $\sim 200$  Hz. We can also modulate the back piezo actuators, in DC or AC, and a similar lowpass filtering occurs with a lower cutoff frequency  $\sim 50$ Hz (3 piezo actuators in parallel with a capacitance of around 100 nF each).

We then monitor the cavity resonances using both the reflected and transmitted photodiodes and scanning the cavity over a large range, as to mode match the cavity to the TEM<sub>00</sub> mode. By beam walking, we optimally mode match the cavity such that higher order modes vanish in the photodiode noise floor and the reflected and transmitted signals are maximised, we can then perform finer scans to characterize the cavity parameters.

**Cavity resonances versus membrane position:** We first scanned the input mirror piezo with a linear ramp  $V_{SW}$  ranging from 0 to 500V at 10-50Hz, corresponding to a displacements of around  $2\mu m$ . The back piezo actuating the membrane position was driven by a DC voltage  $V_{DC}$  ranging from 0 to 70V, with an associated stroke of  $4\mu m$  (3 piezos). A typical scan is shown in Fig. ??(a), where we can see three to four distinct resonance branches as well as the avoided crossings, and where one can also notice the non linearity of the piezo actuators. Knowing the FSR of the cavity, we calibrate the piezo displacement as a function of the applied voltage, and fit the resonances positions using the theoretical model detailed in chapter 3. We modelled the front cavity length  $L_1$  as well as the back cavity length  $L_2$  as third order polynomials of the applied voltages  $V_{SW}$  and  $V_{DC}$  such that

$$\begin{aligned} L_1 &= a_0 + a_1 V_{SW} + a_2 V_{SW}^2 + a_3 V_{SW}^3 - \alpha V_{DC} \\ L_2 &= b_0 + b_1 V_{DC} + b_2 V_{DC}^2 + b_3 V_{DC}^3 \end{aligned} \quad (\text{IV.2})$$

where we introduced the coefficients  $a_i$  and  $b_i$  to be fitted, as well as a cross-coupling term  $\alpha V_{DC}$  to take into account the fact that the back piezo actuators does change the front cavity length since the piezo pushing the back cavity assembly bends the silicon frame.

The rescaled scans are shown in Fig. ??(b), where we can see a good agreement between the experimental data and the theoretical model. This fits allow us to extract the membrane reflectivity  $|r_m|$ , which was found to be 0.54, such that we estimate the power

reflectivity and transmittivity of the membrane to be 0.30 and 0.70, respectively. These transfer functions will also be of use as a calibration to plot the cavity parameters as a function of the membrane position  $x$  rather than the applied voltage  $V_{DC}$ . [link to expected value](#).

[link to expected value](#). As seen in the scans, and contrary to the model developped earlier, we see an overall increase of the different resonance branches, owing to the shortening of the cavity upon actuation of the back piezo, causing an overall drift of the resonances.

**Finesse :** We use three different methods to evalutate the finesse of the cavity.

- The first one would be to scan the cavity over few FSRs, and fit the lorentzian dips such that we can extract the ratio of their interspacings to their linewidths. This method is quite sensitive to the piezo nonlinearities, arising both from the system's transfer function and from the low pass filtering of the voltage ramp by the electronics. One can however used a sine ramp below the electronics cutoff frequency and calibrate the displacement owing to the fact that each resonance corresponds to a displacement of  $\lambda/2$  (one FSR). For our system, this method turned out to be hardly reliable, since a large sweep amplitude implies a fast sweep over the resonance, which started exhibiting dynamical effects such as cavity ringdowns.
- The second method would be to scan the cavity over a single resonance, and use the EOM sidebands as a frequency reference to extract the linewidth of the resonance. This method is less sensitive to piezo nonlinearities, assuming the piezo sweep is quasi linear over the resonance width.
- The third method would be to scan the cavity rapidly and observe a cavity ringdown, and compare the heights of the first two rebounds in transmission to their temporal spacings. This method is less sensitive to piezo nonlinearities, but requires a fast photodiode. Additionally we can vary the piezo sweep frequency to scan for various sweep rates.

**Empty cavity:** By using the second method for our finesse estimation, the empty cavity finesse was measured to be  $\sim 28000$ , such that we deduce total loss of  $\sum T_i = 225 \pm 20\text{ppm}$  (including losses). The LMA did not provide us with specification sheets for the exact mirrors we used, but the uncertainty on the sum of the transmissions is estimated to be around 15ppm. In turn, we can estimate the excess cavity losses to be around  $\gamma = 105\text{ppm}$ . [errors](#)

**MATE cavity:** Once the membrane is inserted inside the cavity, both the resonant frequencies and the linewidths-finesse vary as a function of the membrane position  $x$ .

Using the IR EOM as a frequency ruler, setting a reference between few MHz to  $\sim 60$  MHz (limited by the RedPitaya) we perform lorentzian fits of the three lorentzian dips, and compare the fitted positions. Two typical scans are shown in Fig. ??, one large scan over few cavity FSRs, and a narrow one.

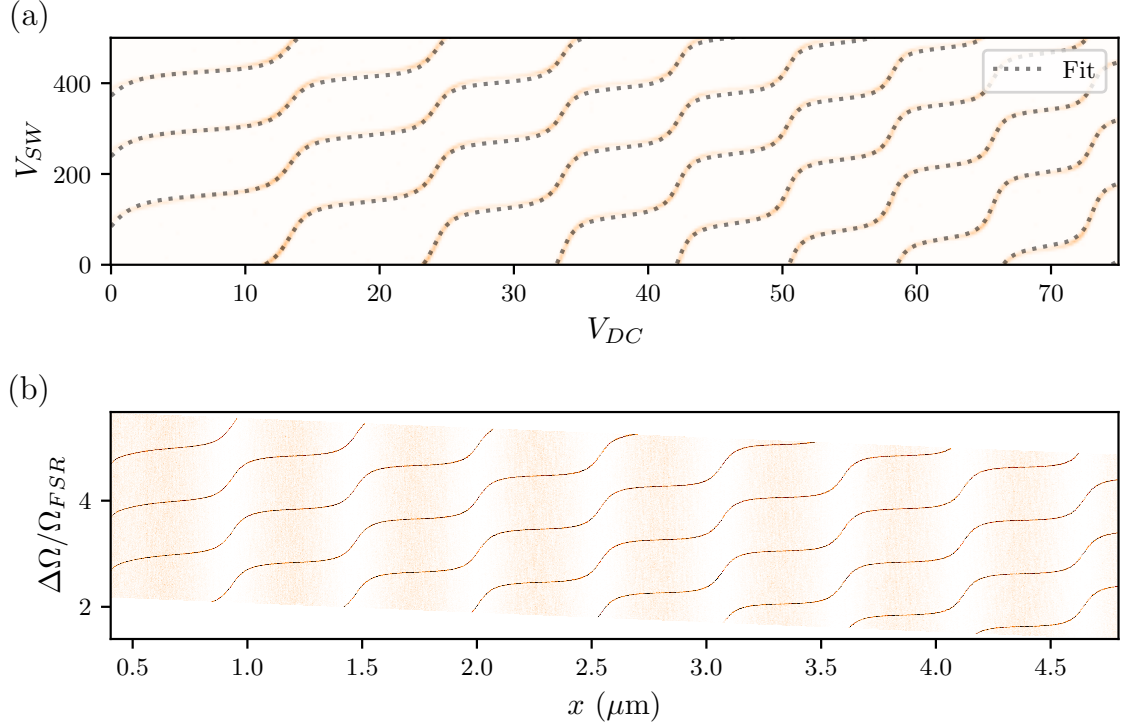


Fig. IV.5

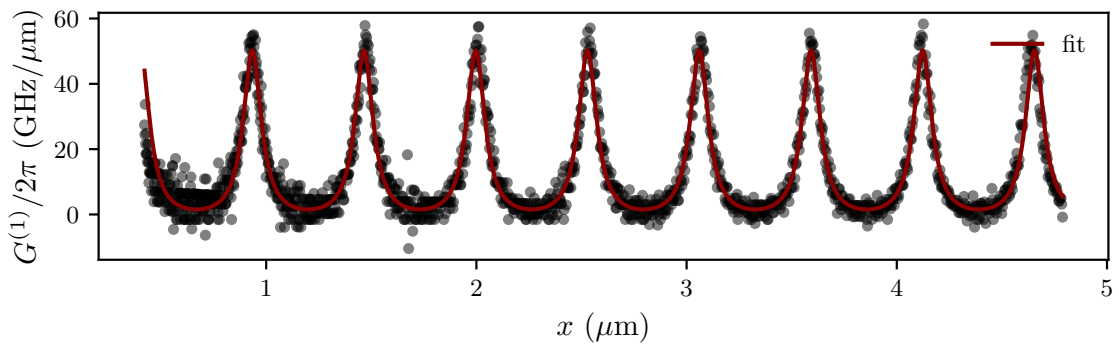


Fig. IV.6

**Position dependent finesse:** We now record cavity scans at increasing values of  $V_{DC} \propto$

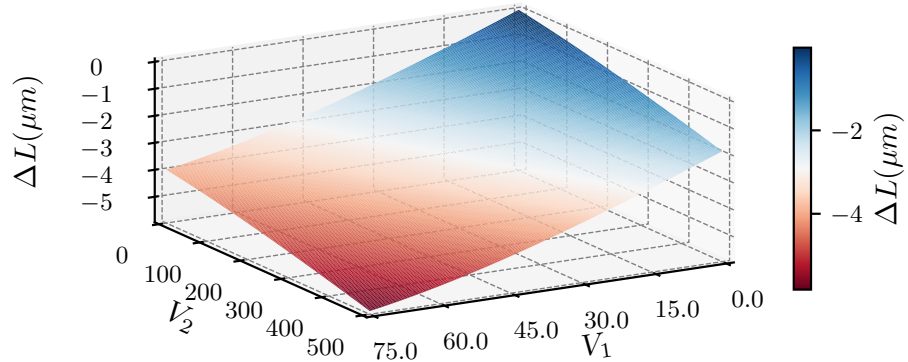


Fig. IV.7

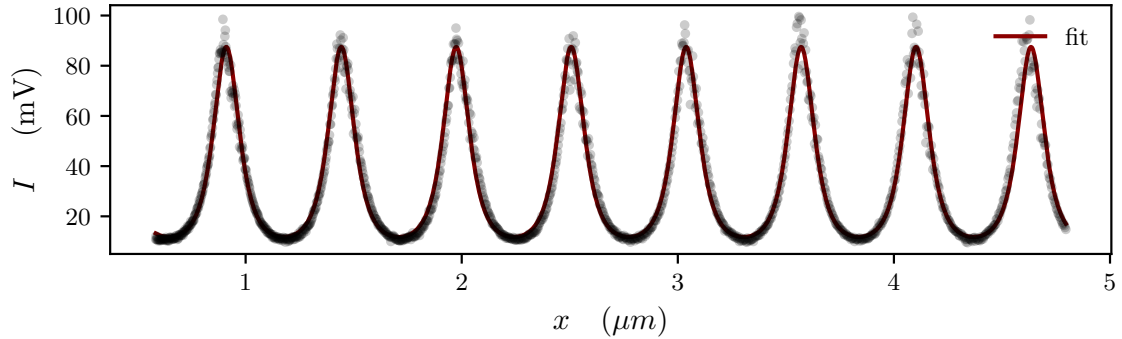


Fig. IV.8

$P_3(x)$ . The finesse oscillates between  $\sim 6000$  and  $\sim 20000$ , which corresponds to total losses  $\Sigma T_i$  between 300 ppm and 1050 ppm. This is significantly higher than the empty cavity losses, which indicates that the membrane introduces significant additional losses.

Using the IR EOM as a frequency ruler, we can perform slow scans of the cavity length while monitoring the transmitted intensity. By carefully controlling the piezo voltage and using a lock-in amplifier to extract the signal, we can obtain high-resolution measurements of the cavity resonances. This technique allows us to probe the cavity modes with great precision and is particularly useful for characterizing the effects of the membrane on the cavity dynamics.

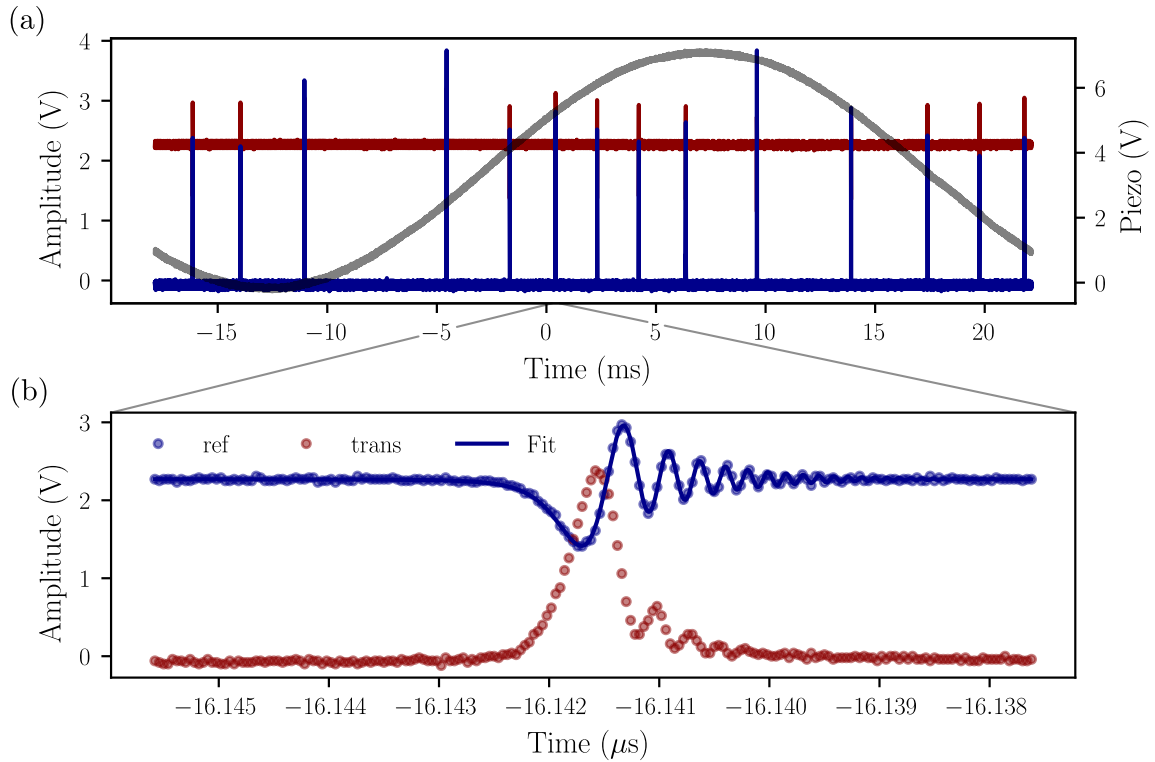


Fig. IV.9

#### IV.2.2 Locking Techniques and Stability

#### IV.2.3 Optical Ringdowns and Loss Measurements

#### IV.2.4 Mechanical Resonator Characterization

#### IV.2.5 Bistability

### IV.3 Design of an Optomechanical Fibered Cavity

#### IV.3.1 Design considerations

# Chapter V

## Experiments: Squeezed Light

This chapter will cover the experimental methods used in the development of frequency-dependent squeezing in optomechanical systems, focusing on the generation of squeezed light, optical locking techniques, and quadrature measurement methods. The methods are designed to enhance the sensitivity of measurements in quantum optics and optomechanics.

### Contents

---

<b>V.1 Optical Setup Overview</b> . . . . .	<b>86</b>
<b>V.2 Cavity Resonances and Locks</b> . . . . .	<b>86</b>
V.2.1 IRMC Cavity . . . . .	86
V.2.2 SHG Cavity . . . . .	88
V.2.3 OPO Cavity . . . . .	91
<b>V.3 Spectral analysis</b> . . . . .	<b>91</b>
V.3.1 Detection of Squeezing and Anti-squeezing . . . . .	91
V.3.2 Spectral Variation with Frequency . . . . .	91
V.3.3 Optimal Quadrature Conditions . . . . .	91
<b>V.4 Filter Cavity Concept</b> . . . . .	<b>91</b>
V.4.1 Virgo Filter Cavity . . . . .	91
V.4.2 Thermal effects in bichromatic locks . . . . .	91
<b>Appendix: PDH Derivation</b> . . . . .	<b>95</b>
<b>Appendix: Spectra Derivation</b> . . . . .	<b>99</b>

---

## V.1 Optical Setup Overview

We first provide a general overview of the optical setup used to generate and manipulate squeezed light. Two lasers are used in this setup, to give flexibility as to produce bright squeezing directly from the OPO (one laser only), or produce vacuum squeezing to be mixed with a bright coherent field (two lasers). Both lasers are 1064nm Nd:YAG lasers (Coherent Mephisto and Mephisto S) as in the previous chapter. The full optical layout is shown in figure ???. The experiment was designed as to easily switch between the two configurations. Throughout this chapter, we will refer to three different optical cavities common to the two configurations: the infrared mode cleaner (IRMC) cavity, the SHG cavity, and the OPO cavity. Each of these cavities is central to the generation and manipulation of squeezed light, and their characterization is detailed in the following sections.

To generate bright squeezed light from an OPO, there are two configurations. The first one uses a single laser source, where the main laser beam is split into two paths. One path is directed to the SHG cavity to generate the second harmonic pump beam at 532nm, while the other path serves both for the Homodyne LO, as well as to seed the OPO with a bright field to be parametrically amplified or deamplified.

The second configuration employs two independent lasers: one dedicated to pumping the SHG cavity and generating the 532nm pump beam, and the other serving as the LO for homodyne detection. This dual-laser setup allows for greater flexibility in controlling the relative phase and frequency between the pump and LO beams, which is crucial for optimizing squeezing measurements.

## V.2 Cavity Resonances and Locks

### V.2.1 IRMC Cavity

The first cavity presented here is the infrared mode cleaner (IRMC) cavity. The purpose of this cavity is to spatially filter the laser beam, ensuring a high-quality TEM<sub>00</sub> mode profile, as well as *cleaning* the IR beam from any excess classical noise as developed in Chapter ???. It consists in a triangular cavity, with a round trip length of 99 cm, and a finesse of  $\mathcal{F} = 300$ . The input coupler has a transmission of 1.4%, while the other two mirrors are highly reflective. The cavity is designed to be overcoupled, with the input coupler transmission dominating the total round-trip losses. This configuration maximizes the transmission of the fundamental mode while effectively filtering out higher-order spatial modes and excess noise.

## MCIR Cavity

The main reference cavity employed throughout this work is the MCIR cavity, whose relevant parameters are summarized in Table ???. It is a three mirror - *travelling wave* Fabry-Pérot resonator with a total round-trip length of  $L = 84$  cm, corresponding to a free spectral range of  $\text{FSR} = 357$  MHz. With a measured optical bandwidth of  $\kappa/2\pi = 60$  kHz, the finesse reaches a value of  $\mathcal{F} \approx 6000$ , which ensures narrow resonances suitable for frequency stabilization and precision measurements. At resonance, the measured reflectivity is  $R_0 \simeq 0.47$ .

The cavity is formed by two mirrors of complementary characteristics. The curved end mirror has a radius of curvature  $\text{RoC} = -2$  m, while both the input and output mirrors are plano with transmissions  $T_{\text{in}} = T_{\text{out}} = 475$  ppm. Additional intracavity losses were estimated to be  $P \approx 718$  ppm, as computed from Eq. (II.72), which assumes ideal mode matching of the laser to the cavity. From these values, one obtains a stable resonator with a well-defined mode geometry. The Gaussian beam waist at the cavity center is  $w_0 = 578$   $\mu\text{m}$ , calculated using the standard mode waist formula [?].

The combination of high finesse, moderate cavity length, and relatively large mode waist makes the MCIR cavity particularly well-suited for applications requiring high spectral selectivity with minimal sensitivity to mirror surface imperfections or thermal effects. Its design parameters are optimized to balance transmission through the input and output couplers with the unavoidable excess loss, ensuring a stable operation point for subsequent experiments.

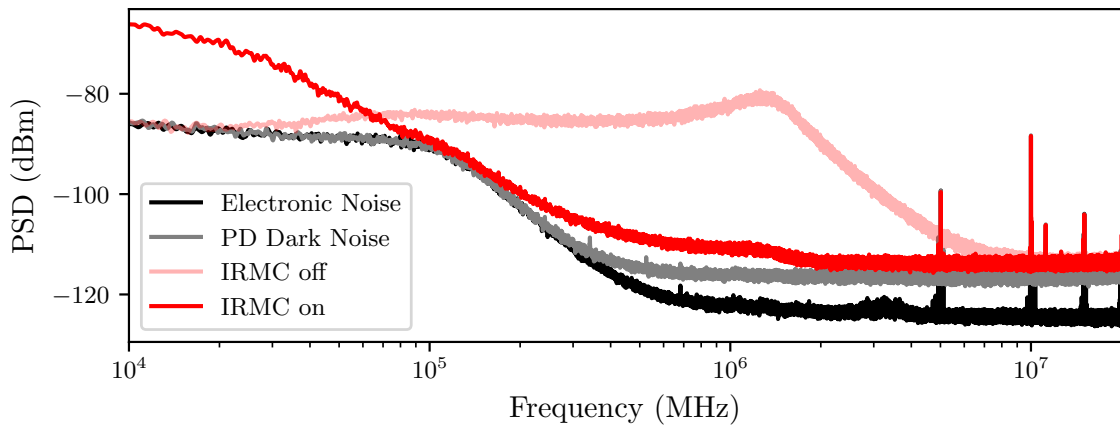


Fig. V.1

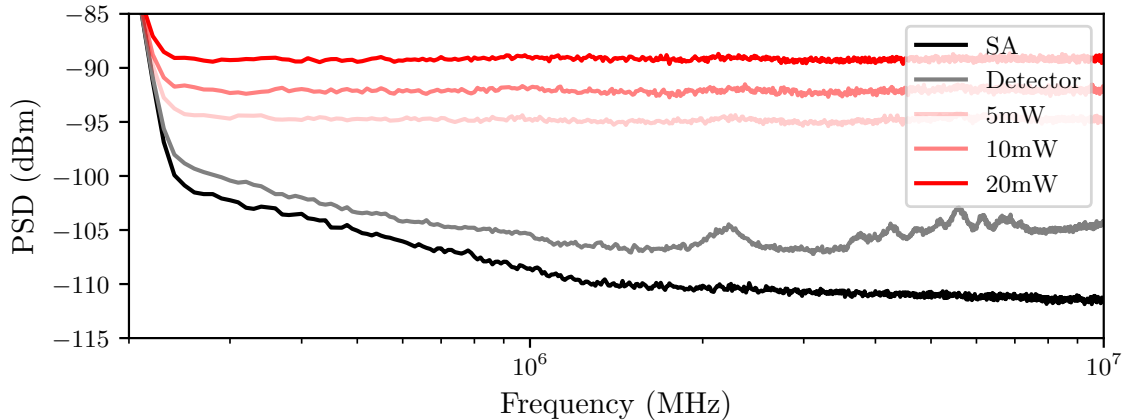


Fig. V.2

### V.2.2 SHG Cavity

In order to generate a stable 532 nm pump beam for the OPO, we implemented and characterized a linear SHG cavity. The cavity is designed to resonantly enhance an incoming IR field at 1064 nm and convert it into its second harmonic through a periodically poled lithium niobate (PPLN) crystal. In what follows we detail the characterization sequence.

**Cavity Scanning and Resonance Mapping.** The cavity is linear, with a length of 45 mm, where both mirrors have a radius of curvature of 250 mm:  $L < 2R$  so the cavity is stable. The input coupler has a transmission of 10% at 1064 nm and less than 1% at 532 nm. The end mirror has a reflectivity of 99.9% for both 1064 nm and 532 nm. This results in a theoretical cavity finesse of approximately 60 at 1064 nm, while the finesse at 532 nm would be around 1, as no cavity buildup is desired at this wavelength. Initial characterization was performed by scanning the cavity length around resonance using a piezoelectric transducer on which the cavity output coupler was glued. The input infrared power was maintained at approximately 100 mW. The transmitted infrared signal and the generated green output were simultaneously monitored on fast photodiodes, while the PZT drive voltage was recorded to provide a calibrated frequency axis.

Typical traces of the transmitted IR beam are shown in Fig. ??(b)–(c). As the cavity length is swept, the cavity exhibits sharp IR resonance peaks, corresponding to successive TEM<sub>00</sub> modes of the cavity. At the same time, the green output rises only in coincidence with infrared resonances, confirming that efficient SHG occurs exclusively under resonant build-up of the fundamental field. The actual IR finesse was measured to be  $\mathcal{F} = 35 \pm 0.6$ , where the discrepancy is attributed to poor knowledge of the mirror parameters, as well as optical losses from the non linear medium. The polarization of the input beam is controlled

by half and quarter waveplates as to maximize the output green power, and the symmetry of the resonance peaks in the scans further indicates negligible birefringence in the PPLN crystal.

**Cavity Locking.** While scanning is useful for diagnostics, stable operation of the OPO pump requires continuous locking of the cavity to resonance. To achieve this, we employed a dither lock technique. The infrared input beam was phase-modulated at  $\Omega_{\text{mod}} = 19 \text{ MHz}$  using a free space EOM (Photline NIR-MPX-LN-10). The transmitted infrared beam is demodulated and provides an error signal suitable for feedback to the PZT actuator. The cabling of the RedPitaya and other elements are detailed in Chapter ??.

**Nonlinear Crystal and Phase Matching.** The nonlinear medium is a commercially available PPLN chip from Covision, with dimensions  $10 \times 10 \times 1 \text{ mm}^3$  and five parallel poling periods. Each grating corresponds to a different quasi-phase-matching period, enabling SHG for pump wavelengths near  $1064 \text{ nm}$  across a wide temperature range. For our Nd:YAG source we selected the  $\Lambda \simeq 6.9 \mu\text{m}$  grating, designed for SHG around  $65^\circ\text{C}$ . The crystal is AR coated at both  $1064 \text{ nm}$  and  $532 \text{ nm}$ , limiting intra-cavity facet losses.

The conversion efficiency usually follows a sinc-squared dependence on temperature. Due to the high IR power build-up in the cavity, thermal effects are observed, which distort the expected sinc<sup>2</sup> shape as reported in ... When locking the cavity, hence stabilizing intracavity power at (relatively) high IR intensity, the non-linear crystal undergoes heating due to the IR absorption. Immediately, its bulk starts to dilate, changing the quasi-phase matching conditions.

After taking a rough quasi-phase matching curve not shown here, we identified the central peak and performed a fine scale scan of the crystal temperature at the IR input power allowing us to recover around  $100 \text{ mW}$  of green power, necessary to pump the OPO below threshold. For an input IR power of around  $200 \text{ mW}$ , the generated green power as a function of temperature is shown in (a) of figure V.4, where we observed a tilt of the phase matching curve. The sinc<sup>2</sup> shape is however recovered when injecting an order of magnitude less IR power, but not useful to our purpose as it does not provide sufficient power for the OPO. The optimum is found at  $58.37^\circ\text{C}$  for the  $6.90 \mu\text{m}$  grating, with a measured phase-matching bandwidth  $\Delta T \simeq 1.5^\circ\text{C}$  (FWHM).

**Temperature-Induced Resonance Shifts.** In addition to determining phase-matching, the crystal temperature modifies the effective optical length of the cavity. As the temperature increases, the refractive index  $n(T)$  rises, effectively lengthening the cavity. When the cavity is locked, an increase in intracavity IR power induces heating of the PPLN, which shifts the resonance condition. This thermal feedback manifests as a tilt in the transmission traces

during PZT sweeps at high input powers [Fig. ??(c)].

At moderate powers ( $P_\omega < 200$  mW) the effect is negligible, but at higher powers the thermo-optic shift dominates, causing a deviation from the ideal  $\text{sinc}^2$  dependence of the conversion efficiency. Instead, the efficiency curve skews and broadens, and thermal lensing within the crystal degrades the spatial overlap of the intracavity mode. In practice, we observed that beyond  $\sim 200$  mW of circulating IR power, the green output no longer increases linearly with  $P_\omega$ , but saturates due to these thermal effects.

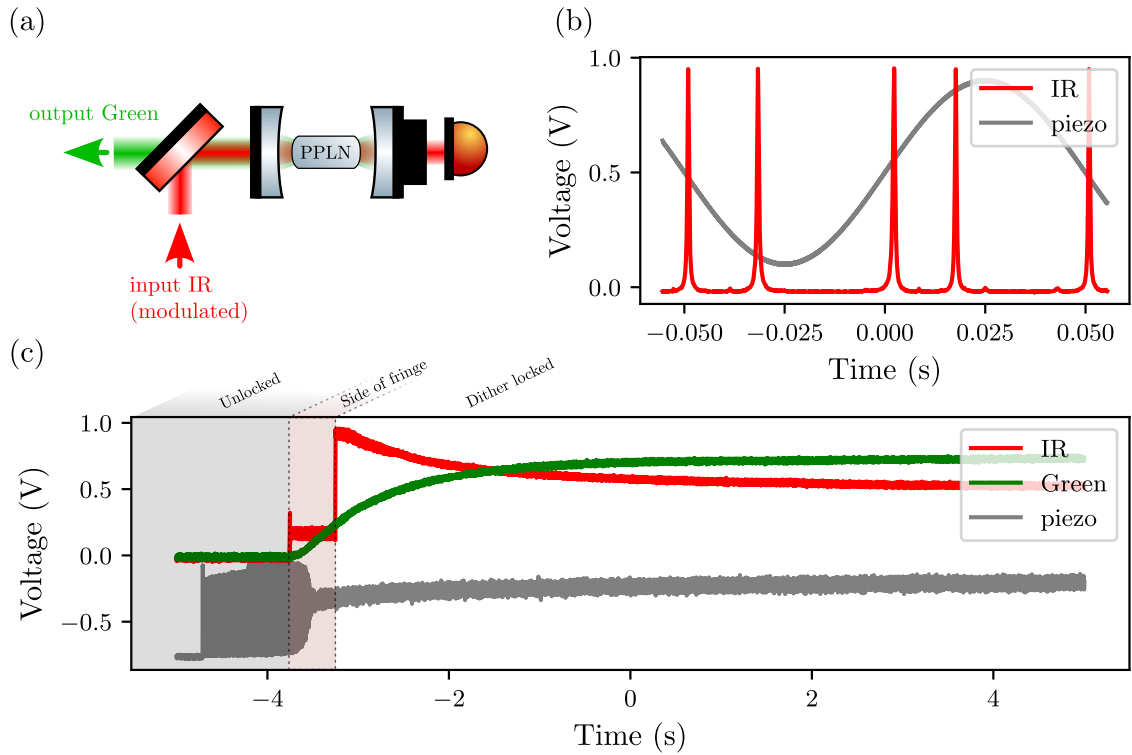


Fig. V.3

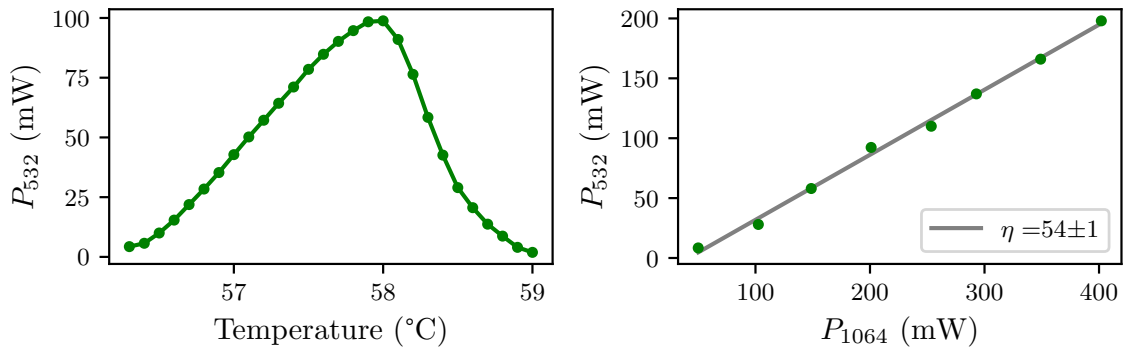


Fig. V.4

### V.2.3 OPO Cavity

## V.3 Spectral analysis

### V.3.1 Detection of Squeezing and Anti-squeezing

### V.3.2 Spectral Variation with Frequency

### V.3.3 Optimal Quadrature Conditions

## V.4 Filter Cavity Concept

### V.4.1 Virgo Filter Cavity

### V.4.2 Thermal effects in bichromatic locks



# **Summary, conclusion and perspectives**

This chapter will cover the summary of the work done, the conclusions drawn from the experiments, and the perspectives for future research in optomechanical systems. It will highlight the key findings, their implications for quantum optics, and potential directions for further exploration.



# Appendix 1: Derivation of the PDH Error Signal

In this appendix, we derive the Pound-Drever-Hall (PDH) error signal starting from the real, quantum-normalized phase-modulated electric field expression. We aim to show how the demodulated signal is a linear combination of the real and imaginary parts of the cavity reflection coefficient, with the demodulation phase selecting the appropriate quadrature for locking.

## 1. Input Phase-Modulated Field

The electric field at the input of the cavity is assumed to be a coherent state that has been phase-modulated at frequency  $\Omega$ , such that the classical (real) electric field takes the form:

$$E_{\text{cl}}^{(\text{PM})}(t) = i\sqrt{\frac{\hbar\omega_0}{2\varepsilon_0}} \alpha_0 \left[ e^{-i\omega_0 t} - e^{i\omega_0 t} + \frac{i\epsilon_\phi}{2} (e^{-i(\omega_0-\Omega)t} + e^{i(\omega_0-\Omega)t}) + \frac{i\epsilon_\phi}{2} (e^{-i(\omega_0+\Omega)t} + e^{i(\omega_0+\Omega)t}) \right] \quad (1)$$

where  $\alpha_0$  is the coherent amplitude of the carrier,  $\epsilon_\phi \ll 1$  is a small modulation index (related to the phase modulation depth), and  $\omega_0$  is the optical carrier frequency. This field includes both the positive and negative frequency components, as expected for a physical (Hermitian) electric field operator.

## 2. Reflection from the Cavity

Each frequency component of the field is reflected with a complex frequency-dependent amplitude reflection coefficient  $r(\omega)$ , such that the reflected field is:

$$\begin{aligned} E_{\text{refl}}(t) = & i\sqrt{\frac{\hbar\omega_0}{2\varepsilon_0}} \alpha_0 \left[ r(\omega_0)e^{-i\omega_0 t} - r^*(\omega_0)e^{i\omega_0 t} \right. \\ & + \frac{i\epsilon_\phi}{2} \left( r(\omega_0 - \Omega)e^{-i(\omega_0-\Omega)t} + r^*(\omega_0 - \Omega)e^{i(\omega_0-\Omega)t} \right) \\ & \left. + \frac{i\epsilon_\phi}{2} \left( r(\omega_0 + \Omega)e^{-i(\omega_0+\Omega)t} + r^*(\omega_0 + \Omega)e^{i(\omega_0+\Omega)t} \right) \right] \end{aligned} \quad (2)$$

### 3. Photodetected Intensity

The photodetector measures the intensity:

$$I(t) \propto |E_{\text{ref}}(t)|^2$$

We isolate the terms oscillating at  $\Omega$ , which arise from the interference between the carrier and sideband components. Keeping only the beat terms between the carrier and sidebands, we find:

$$I(t) \supset \epsilon_\phi \cdot \text{Re}[A_+ - A_-] \cos(\Omega t) + \epsilon_\phi \cdot \text{Im}[A_+ - A_-] \sin(\Omega t) \quad (3)$$

where we define:

$$A_\pm = r(\omega_0)r^*(\omega_0 \pm \Omega)$$

### 4. Demodulation with Arbitrary Phase

The signal is demodulated using a local oscillator  $\cos(\Omega t + \phi)$ , where  $\phi$  is the demodulation phase. Using trigonometric identities:

$$\cos(\Omega t + \phi) = \cos(\Omega t) \cos \phi - \sin(\Omega t) \sin \phi$$

we multiply Equation (3) and low-pass filter to obtain:

$$\epsilon_{\text{PDH}}(\phi) \propto \epsilon_\phi \{ \text{Re}[A_+ - A_-] \cos \phi + \text{Im}[A_+ - A_-] \sin \phi \} \quad (4)$$

### 5. Sidebands Far Off-Resonance Approximation

In the standard PDH regime, the modulation frequency is much greater than the cavity linewidth:

$$\Omega \gg \kappa$$

so the sidebands are far off-resonance. This means:

$$r(\omega_0 \pm \Omega) \approx 1 \Rightarrow A_\pm \approx r(\omega_0)$$

and therefore:

$$A_+ - A_- \approx 0$$

However, if we retain the asymmetry between the sidebands (e.g., due to dispersion), or keep the finite detuning contribution, we approximate:

$$A_+ - A_- \approx r(\omega_0) [r^*(\omega_0 + \Omega) - r^*(\omega_0 - \Omega)] = r(\omega_0) \Delta r^*$$

## 6. Final Result

Substituting into Equation (4), we obtain:

$$\epsilon_{\text{PDH}}(\phi) \propto \epsilon_\phi \{ \text{Re}[r(\omega_0)\Delta r^*] \cos \phi + \text{Im}[r(\omega_0)\Delta r^*] \sin \phi \} \quad (5)$$

In the limit where  $\Delta r^* \rightarrow 1$  (normalized, symmetric sidebands), this simplifies to:

$$\boxed{\epsilon_{\text{PDH}}(\omega_0, \phi) \propto \cos \phi \cdot \text{Re}[r(\omega_0)] + \sin \phi \cdot \text{Im}[r(\omega_0)]} \quad (6)$$

## 7. Interpretation

Equation (6) shows that the demodulated error signal is a linear superposition of the real and imaginary parts of the complex reflection coefficient. The demodulation phase  $\phi$  selects the detected quadrature:

- $\phi = 0$ : error signal is proportional to  $\text{Re}[r]$  — symmetric around resonance, not suitable for locking.
- $\phi = \pi/2$ : error signal is proportional to  $\text{Im}[r]$  — antisymmetric, ideal dispersive error signal.
- $\phi \neq 0, \pi/2$ : mixes quadratures, possibly introducing offset or distortion.

This derivation makes explicit how the PDH method uses phase-sensitive detection to extract the component of the reflection coefficient that varies linearly with detuning, enabling precise feedback locking of the laser to the cavity resonance.



## Appendix 2: Spectra derivation

$$\hat{p}[\Omega] = 2|\alpha| \left( \delta[\Omega] + \operatorname{Re}\{\varepsilon[\Omega]\} \right) + \delta\hat{p}[\Omega], \quad (7)$$

$$\hat{p}[\Omega] \hat{p}[\Omega'] = 4|\alpha|^2 \left( \delta[\Omega]S[\Omega'] + \delta[\Omega] \operatorname{Re}\{\varepsilon[\Omega']\} + \delta[\Omega'] \operatorname{Re}\{\varepsilon[\Omega]\} + \operatorname{Re}\{\varepsilon[\Omega]\} \operatorname{Re}\{\varepsilon[\Omega']\} \right) + \delta\hat{p}[\Omega] \delta\hat{p}[\Omega'], \quad (8)$$

$$\langle \dots \rangle = 4|\alpha|^2 \left( \delta(\Omega) \delta(\Omega') + \frac{\varepsilon}{2} \delta(\Omega) \delta(\Omega' - \Omega_m) + \frac{\varepsilon}{2} \delta(\Omega) \delta(\Omega' + \Omega_m) \right. \quad (9)$$

$$+ \frac{\varepsilon}{2} \delta(\Omega') \delta(\Omega - \Omega_m) + \frac{\varepsilon}{2} \delta(\Omega') \delta(\Omega + \Omega_m) \quad (10)$$

$$+ \frac{\varepsilon^2}{4} \left[ \delta(\Omega - \Omega_m) \delta(\Omega' + \Omega_m) + \delta(\Omega - \Omega_m) \delta(\Omega' - \Omega_m) \right. \quad (11)$$

$$\left. + \delta(\Omega + \Omega_m) \delta(\Omega' + \Omega_m) + \delta(\Omega + \Omega_m) \delta(\Omega' - \Omega_m) \right] \Big) + \langle \delta p[\Omega] \delta p[\Omega'] \rangle. \quad (12)$$



# Derivation of the optimal angle

## Optimal fixed homodyne angle with complex $\mathcal{K}$

Assume the measured (reflected) quadrature is

$$\delta q_r = \delta q_{\text{in}} + \mathcal{K} \delta p_{\text{in}},$$

so that, for any input covariance matrix  $S^{\text{in}}$ ,

$$S_{qq}^r = S_{qq}^{\text{in}} + |\mathcal{K}|^2 S_{pp}^{\text{in}} + 2 \operatorname{Re}\{\mathcal{K}\} S_{pq}^{\text{in}}.$$

For an input squeezed state of strength  $R$  and angle  $\theta$ ,

$$S^{\text{in}}(R, \theta) = \begin{pmatrix} \cosh R - \sinh R \cos 2\theta & -\sinh R \sin 2\theta \\ -\sinh R \sin 2\theta & \cosh R + \sinh R \cos 2\theta \end{pmatrix}.$$

Hence

$$\begin{aligned} S_{qq}^r(\theta) &= \cosh R - \sinh R \cos 2\theta + |\mathcal{K}|^2 (\cosh R + \sinh R \cos 2\theta) - 2 \operatorname{Re}\{\mathcal{K}\} \sinh R \sin 2\theta \\ &= (1 + |\mathcal{K}|^2) \cosh R + (|\mathcal{K}|^2 - 1) \sinh R \cos 2\theta - 2 \operatorname{Re}\{\mathcal{K}\} \sinh R \sin 2\theta. \end{aligned} \quad (13)$$

**Optimal fixed angle.** Differentiate (13) w.r.t.  $\theta$  and set to zero:

$$\frac{\partial S_{qq}^r}{\partial \theta} = -2 \sinh R \left[ (|\mathcal{K}|^2 - 1) \sin 2\theta + 2 \operatorname{Re}\{\mathcal{K}\} \cos 2\theta \right] = 0,$$

which gives the optimal fixed readout angle

$$\tan(2\theta_{\text{opt}}) = \frac{2 \operatorname{Re}\{\mathcal{K}\}}{1 - |\mathcal{K}|^2} \quad (14)$$

Writing  $\mathcal{K} = |\mathcal{K}| e^{i\varphi_m}$  one may also use

$$\tan(2\theta_{\text{opt}}) = \frac{2|\mathcal{K}| \cos \varphi_m}{1 - |\mathcal{K}|^2}.$$

**Minimum attained value.** Equation (13) can be written as

$$S_{qq}^r(\theta) = (1 + |\mathcal{K}|^2) \cosh R + M \sinh R \cos(2\theta - \phi),$$

with

$$M = \sqrt{(|\mathcal{K}|^2 - 1)^2 + (2 \operatorname{Re}\{\mathcal{K}\})^2}, \quad \phi = \operatorname{atan2}(-2 \operatorname{Re}\{\mathcal{K}\}, |\mathcal{K}|^2 - 1).$$

The minimum is therefore

$$S_{qq,\min}^r = (1 + |\mathcal{K}|^2) \cosh R - M \sinh R.$$

(15)

**Lower bound and the real- $\mathcal{K}$  case.** Using  $M^2 = (1 + |\mathcal{K}|^2)^2 - 4(\operatorname{Im}\{\mathcal{K}\})^2$ , one finds

$$M \leq 1 + |\mathcal{K}|^2 \implies S_{qq,\min}^r \geq (1 + |\mathcal{K}|^2) e^{-R},$$

with equality *iff*  $\operatorname{Im}\{\mathcal{K}\} = 0$  (i.e.  $\mathcal{K}$  real). When  $\mathcal{K} \in \mathbb{R}$ ,

$$\tan(2\theta_{\text{opt}}) = \frac{2\mathcal{K}}{1 - \mathcal{K}^2} \stackrel{\text{(double-angle)}}{\iff} \theta_{\text{opt}} = \arctan(\mathcal{K}) \pmod{\frac{\pi}{2}},$$

and the minimum (15) saturates the bound:

$$S_{qq,\min}^r = (1 + \mathcal{K}^2) e^{-R}.$$











---

## Sujet : Progress towards cryogenic squeezed light optomechanics

---

Résumé : .

**Mots clés :** Optomecanique, Lumière comprimée, Cavité de grande Finesse, Interferométrie, Bruit thermique, Bruit de grenaille quantique, Resonateur de grand facteur de Qualité, Interféromètres pour la detection d'ondes gravitationnelles, Bruit de pression de radiation quantique

---

## Subject : Optomechanics and squeezed light

---

**Abstract:**

**Keywords :** Optomechanics, Squeezing, High-Finesse cavity, Interferometry, Thermal Noise, Quantum Shot Noise, High-Q Resonator, Gravitational wave Interferometer, Quantum Radiation Pressure Noise

